APPLICATION OF HYDROGEOPHYSICAL IMAGING IN THE REYNOLDS CREEK CRITICAL ZONE OBSERVATORY

by

Travis Nielson

A thesis

submitted in partial fulfillment

of the requirements for the degree of

Master of Science in Geophysics

Boise State University

December 2017

BOISE STATE UNIVERSITY GRADUATE COLLEGE

DEFENSE COMMITTEE AND FINAL READING APPROVALS

of the thesis submitted by

Travis Nielson

Thesis Title: Application of Hydrogeophysical Imaging in The Reynolds Creek Critical Zone Observatory

Date of Final Oral Examination: 01 May 2017

The following individuals read and discussed the thesis submitted by student Travis Nielson, and they evaluated his presentation and response to questions during the final oral examination. They found that the student passed the final oral examination.

John Bradford, Ph.D.	Chair, Supervisory Committee
James P. McNamara, Ph.D.	Member, Supervisory Committee
Lee M. Liberty, M.S.	Member, Supervisory Committee

The final reading approval of the thesis was granted by John Bradford, Ph.D., Chair of the Supervisory Committee. The thesis was approved by the Graduate College.

ACKNOWLEDGEMENTS

First I would like to acknowledge my adviser Professor John Bradford for his continued guidance and patients. My committee member Professor Lee Liberty for making sure my writing and methods were sound and Professor Jim McNamara for providing all of the hydrology know how to a project run by a physicist. Professor Steve Holbrook, at the University of Wyoming, and his student Brady Flinchum for being so generous with their data, insight, and time, with their help my understanding of the critical zone was greatly advanced. The countless professors and students in the BSU Geosciences department, who were all so generous with their insights into the hydrologic and geomorphic implications of this work. Mark Seyfried and Steve Van Vactor at the USDA ARS for providing the hydrologic data that made this work come together. The at least two dozen volunteer graduate and under-graduate students who were deceived into participating in grueling field campaigns in the middle of a hot summer. Of my fellows students Aida Mendieta, Diego Domenzain, Amy Streimke, and Paden Gould, were brave enough to participate in multiple surveys and thus invaluable in the field. And lastly the Reynolds Creek Critical Zone Observatory for funding me and this research.

ABSTRACT

The critical zone is defined as the upper most portion of the crust extending from the top of unweathered bedrock to the top of the vegetation canopy. It is the zone in which inorganic rock is transformed into biologically useful soils and saprolites in a process termed weathering. Because the critical zone is the connection between the subsurface and surface it plays a role in a wide variety of biological, hydrologic, and climatic processes. Understanding the critical zone though is inherently difficult because its scale and heterogeneity often means direct sampling methods, e.g. soil pits and cores, under represent the heterogeneous critical zone process. Geophysical methods are increasingly applied to study the near-surface processes at a variety of spatial and temporal scales. This paper presents two geophysical experiments that capture two different hydrologic processes and two different scales: the first is the study of the influence of aspect, elevation, and snow accumulation on weathering depths at the catchment scales using seismic refraction tomography and second is the application of electrical resistivity tomography to observe the heterogeneous seasonal change of soil moisture and its connectivity at the plot scale.

TABLE OF CONTENTS

ACKNOWLEDGEMENTS iv

ABSTRACT v

LIST OF TABLES viii

LIST OF FIGURES iix

LIST OF ABBREVIATIONS xi

CHAPTER ONE: INTRODUCTION TO THE CRITICAL ZONE AND HYDROGEOPHYSICAL IMAGING 1

CHAPTER TWO: GEOPHYSICAL INVERSTIGATION OF THE EFFECT OF ASPECT AND ELEVATION ON CRITICAL ZONE ARCHITECTURE 12

Abstract 12

Introduction 13

Site Description 18

Methods 24

Results 28

Discussion 36

Conclusion 43

CHAPTER THREE: MONITORING NATURAL SOIL MOISTURE INFILTRATION USING TIME-LAPSE 3D ELECTRICAL RESISTIVITY TOMOGRAPHY 46

Abstract 46

Introduction 47

Site-description 52

Methods..55
Results..62
Discussion...68
Conclusion...71
CHAPTER FOUR: SUMMARY AND CONCLUSION 74
REFERENCES 80
APPENDIX A...92
Soil moisture monitoring at the Mid Elevation Sagebrush site 93
Site description..93
Methods...93
Results...95
Discussion..98
Conclusion 101

LIST OF TABLES

Table 1: Hours the shallow soils on both aspects spent within the frost cracking temperature window....24

Table 2: P-wave velocities for the weathering stages of granite as measured by Olona et al. (2010)....28

Table 3: Mean depth and standard deviation to fractured and fresh bedrock for both aspects at each seismic line....29

Table 4: Archie's parameters used in the pedo-physical conversion....60

LIST OF FIGURES

Figure 1: Overview of the Reynolds Creek Critical Zone Observatory 8

Figure 2: Satellite map of the Johnston Draw Watershed.. 10

Figure 3: Soil volumetric water content on the north and south facing aspects throughout Johnston Draw 21

Figure 4: Snow depth on the north and south facing aspects throughout Johnston Draw 22

Figure 5: Soil temperature on the north and south facing aspects throughout Johnston Draw.. 23

Figure 6: An example shot break with picked first arrivals... 25

Figure 7: Observed and modeled first arrivals from Line 4... 26

Figure 8: Fence diagram of the inverted velocity profiles within Johnston Draw........... 31

Figure 9: Inverted velocity profiles with the 700m.s, 2000m/s, and 3500m/s.................. 32

Figure 10: Mean depth to various velocity contours on the north and south facing aspects for each seismic line 33

Figure 11: Difference in weathering depth between the north and south facing slopes for each seismic line.. 35

Figure 12: Illustration of how frost cracking could work in conjunction with soil moisture propagation from snow to increase the weathering on the north facing slope. 432

Figure 13: (a) Map showing the location of the LES and MES study sites. (b and c) Satellite maps of the LES and MES study sites.. 53

Figure 14: Soil volumetric water content measured at the LES site................................ 54

Figure 15: The resistivity grids from the static inversion of the February, 23rd, 2016 (a) and June, 17th, 2016 (b) surveys for the LES site. 60

Figure 16: The 3D resistivity and soil moisture response to a 10mm rainstorm event 63

Figure 17: Fence plot of the 2D resistivity surveys with seismic velocity contours overlain at the LES site 63

Figure 18: Change in 3D resistivity for the spring 2015, spring 2016 and fall 2015 transitions 65

Figure A1: Soil volumetric water content measured at the MES site. 94

Figure A2: Fence plot of the 2D resistivity surveys with seismic velocity contours overlain at the LES site 97

Figure A3: The resistivity grids from the static inversion of the February, 23rd, 2016 (a) and June, 17th, 2016 (b) surveys for the MES site. 97

Figure A4: Change in 3D resistivity for the spring 2015, spring 2016 and fall 2015 transitions 98

Figure A5: The 3D resistivity and soil moisture response to a 8mm rainstorm event 97

LIST OF ABBREVIATIONS

WET	Wave-path Eikonal Traveltime
BCCZO	Boulder Creek Critical Zone Observatory
CZ	Critical Zone
DCEW	Dry Creek Experimental Watershed
ERT	Electrical Resistivity Tomography
GPR	Ground Penetrating Radar
LES	Low-Elevation Sagebrush
MES	Mid-Elevation Sagebrush
RCCZO	Reynolds Creek Critical Zone Observatory
SRT	Seismic Refraction Tomography
TDR	Time-domain Reflectometry
Vp	P-wave Velocity

CHAPTER ONE: INTRODUCTION TO THE CRITICAL ZONE AND HYDROGEOPHYSICAL IMAGING

The critical zone (CZ) is defined as the upper most portion of the crust extending from the top of unweathered bedrock to the top of the vegetation canopy [*Parsekian et al.*, 2015], it is the zone in which inorganic rock is transformed into biologically useful soils and saprolites [*Anderson, SP. et al.*, 2007; *Brantley et al.*, 2007; *Parsekian et al.*, 2015; *Riebe et al.*, 2016]in a process termed weathering. Because the CZ is the connection between the subsurface and surface it plays a role in a wide variety of biological [*Moulton and Berner*, 1998; *Amundson et al.*, 2007; *Gabet and Mudd*, 2010; *Roering et al.*, 2010], hydrologic[*Dunne*, 1998; *Hinckley et al.*, 2014; *Langston et al.*, 2015], and climatic[*Millot et al.*, 2002; *Riebe et al.*, 2004a] processes. Understanding the CZ though is inherently difficult because its scale and heterogeneity often means direct sampling methods, e.g. soil pits and cores, under represent the heterogeneous CZ process. Geophysical methods are increasingly applied to study the near-surface processes at a variety of spatial and temporal scales. My thesis consists of two geophysical experiments that capture two different hydrologic processes and two different scales. The first experiment examines the influence of aspect, elevation, and snow accumulation on weathering depths at the catchment scales using seismic refraction tomography. The second experiment is the application of electrical resistivity tomography to observe the heterogeneous seasonal change of soil moisture and its connectivity at the ten meter scale.

Weathering is the process in which bedrock, saprolites, and soils is chemically and physically altered through its interaction with meteoric water [*Anderson, SP et al.*, 2007], topographic and tectonic stresses [*Molnar et al.*, 2007; *St. Clair et al.*, 2015], and biological processes [*Moulton and Berner*, 1998; *Amundson et al.*, 2007; *Gabet and Mudd*, 2010; *Roering et al.*, 2010]. These forces manifest distinguishable layers of fractured bedrock, saprolite, and soil within the CZ [*Anderson, SP et al.*, 2007]. While the boundary between the layers is most likely not discrete as other geologic contacts, each layer has distinct geologic and geophysical properties that can be used to differentiate them [*Parsekian et al.*, 2015]. Generally as a parent material becomes more weathered the porosity increases. This leads to slower seismic velocities and generally lower electrical resistivities [*Parsekian et al.*, 2015]; it is these later properties that are measured with geophysical methods.

There are a variety of theories that predict the depth of the CZ from the tectonic [*St. Clair et al.*, 2015], geochemical [*Brantley et al.*, 2007], and hydrologic [*Rempe and Dietrich*, 2014] characteristics, however the most basic the depth of weathering is controlled by the availability and reactivity of the water that interacts with weathered and un-weathered material. The availability of reactive water is a function of both the amount of water input into the subsurface and the hydraulic conductivity of the material. The bulk hydraulic conductivity is a function of the conductivity of the material matrix and the density and size of fractures. While fractures can occur through chemical weathering [*Riebe et al.*, 2016], the majority of fractures are inherited from the formation and uplift of the rock material and their opening controlled by regional and topographic regimes. During uplift these fractures open in response to the combined topographic and regional stress field or total stress field. Within a compressive tectonic environment the total stress field decreases under ridges opening fractures and promoting greater weathering under ridges. While in weakly compressive and neutral tectonic regimes the stress field parallels topography and so does weathering depth[*St. Clair et al.*, 2015]. These stress field patterns are reflected in the seismic velocity patterns, i.e. where the total stress is low the seismic velocity is low and where the stress is high the velocity is high. This signal can be complicated in high elevation catchments as the cooler and sometimes snow dominated north facing slopes are subject to unique weathering processes. Two examples of weathering process unique to snow dominated cooler aspects are frost cracking [*Anderson et al.*, 2013] and the hydrologic characteristics of snow which is highly effective at propagating moisture in the deeper CZ [*Langston et al.*, 2015].

The availability of meteoric water at a large scale is a function of climate. However within a single catchment and between aspects, microclimate can vary, causing catchment scale variations in water availability[*Anderson et al.*, 2014]. The upper portion of the CZ is an unsaturated or vadose zone environment which, due to the non-linear hydraulic conductivity of unsaturated flow and evapotranspiration, makes deep water propagation difficult to characterize. Further because of the insulating and water storage properties of snow, hillslopes with persistent winter snow cover have been shown to have more deep CZ moisture recharge than equivalent hillslopes without or with intermittent snow cover [*Langston et al.*, 2015].

The reactivity of the meteoric water is a function of the material and temperature, and while it is easy to find catchments of consistent lithology temperature varies widely with aspect and elevation. As water propagates deeper into the CZ it reacts with the soil, saprolite and fractured bedrock eventually reaching a chemical equilibrium before being flushed out to a stream or infiltrated into deep aquifer recharge[*Rempe and Dietrich*, 2014]. Temperature affects the rate, reactivity and chemical equilibrium concentrations of the weathering process [*Ma et al.*, 2013] with higher temperatures leading to faster weathering. Generally at higher elevations, the rate of weathering is lower than at lower elevations. This signal is complicated by the general increase in precipitation with elevation; however field studies have observed the maximum extent of weathering occurs around rain-snow transition [*Rasmussen et al.*, 2010]. Across aspect, the difference in radiation input leads to differences in weathering extent, with southerly aspects below the rain-snow transition being more weathered than the northerly aspect but above the rain-snow line because of the aforementioned hydrologic properties of water the northerly aspects are more weathered. With the variety of factors that can effect weathering rate it has been observed that the weathering depth can vary along the drainage and sides off a catchment that spans a sufficiently large micro-climactic gradient [*Befus et al.*, 2011].

Within mountainous catchments, unsaturated vertical and lateral flow play a large role in deep CZ recharge and stream discharge. Because of the intricacies of unsaturated flow the hydraulic connectivity of a hillslope or ephemeral riparian area is complex. In order to sustain vertical or lateral unsaturated flow the volumetric water content of the soils in which flow is taking place must be greater than the field capacity of the soil for the whole extent in which flow is taking place. This leads to seasonal periods in which the hillslope is at different levels of connectivity with low connectivity typically being seen during the summer and high connectivity during the winter and spring. However soil moisture distribution is spatially heterogeneous so characterizing the hydraulic connectivity at a specific site is difficult to do with *in site* soil moisture measurements. The complexity of unsaturated flow is compounded by high conductivity flow paths referred to as preferential flow paths that can bypass slower matrix flow. Preferential flow paths can play a large role in vadose zone hydrology [*Tromp-van Meerveld and McDonnell*, 2006a, 2006b] but are hard to characterize due to their relatively small size, difficult to predict spatial distribution, and site dependent formation. Additionally they are usually characterized using destructive methods so their natural response to seasonal change and precipitation has never been observed [*Leslie and Heinse,* 2013]. Nonetheless vadose zone hydraulic connectivity and preferential flow paths play an important role in deep CZ recharge and stream discharge.

With the myriad of controlling factors, the CZ is difficult to characterize at a broad scale. There are generally two approaches to characterizing CZ structure and properties: direct sampling methods and geophysical methods. The direct sampling methods provide a variety of accurate measures of weather degree and depth but are difficult to apply at a catchment scale. Geophysical methods provide spatially broad measurement of physical properties, i.e. electrical resistivity and seismic velocity, at scales ranging from meters to kilometers. Further geophysical acquisition is generally non-destructive, measurements can be applied over the same area to provide a time-lapse picture of geophysical property changes. Because of these reasons geophysical methods have been applied to study the CZ and the weathering zone. There are a variety of geophysical methods that have been used to study the CZ, each measuring a different geophysical property and each with a unique logistical advantage. Seismic refraction tomography (SRT) is particularly well suited for delineating weathering degree and CZ structure as the weathering process reduces P-wave velocity (Vp) [*Parsekian et al.*, 2015]. Additionally there is a well established relationships between weathering degree and seismic velocity [*Olona et al.*, 2010; *Parsekian et al.*, 2015].With a motivated field crew an SRT survey can span kilometers in rough terrain providing catchment scale characterization of the weathering zone. As such SRT has been at both the hillslope and catchment scale [*Befus et al.*, 2011] to map CZ structure and efforts have been made to develop petrophysical models that relate Vp to porosity [*Holbrook et al.*, 2014].

Electrical resistivity tomography (ERT) has also been used to determine weathering structure and degree. Due to the complex relationship between resistivity and weathering degree, ERT surveys need a robust ground truth [*Leopold et al.*, 2013]. ERT arrays can easily be installed permanently and once they are installed individual surveys can be quickly performed. This makes ERT ideal for time-lapse measurements. The sensitivity of electrical resistivity to changes in water content and the well tested Archie's Law relating resistivity and volumetric water content [*Shah and Singh*, 2005] make ERT surveys well suited to monitoring water content changes at a variety of scales. Because of this sensitivity to water content, ERT surveys have been used to elucidate a variety of transient hydrologic processes such as soil moisture changes across ecotones [*Jayawickreme et al.*, 2008; *Niemeyer et al.*, 2017], seasonal changes at the plot scale [*French and Binley*, 2004; *Amidu and Dunbar*, 2007; *Miller et al.*, 2008; *Schwartz et al.*, 2008; *Brunet et al.*, 2010; *Nijland et al.*, 2010; *Calamita et al.*, 2012; *Robinson et al.*, 2012; *Yamakawa et al.*, 2012b; *Brillante et al.*, 2014; *Fan et al.*, 2015; *Niemeyer et al.*, 2017] and moisture infiltration [*Kean et al.*, 1987; *Daily, William et al.*, 1992; *Al Hagrey et al.*, 1999; *Al Hagrey and Michaelsen*, 1999; *Dietrich et al.*, 2003; *Singha and Gorelick*, 2005; *Cassiani et al.*, 2006; *Deiana et al.*, 2007; *Monego et al.*, 2010; *Travelletti et al.*, 2012; *Zumr et al.*, 2012].

The Reynolds Creek Critical Zone Observatory (RCCZO) is a unique study site with high instrument density, a large climactic gradient and varying lithology. Located in southwestern Idaho the RCCZO, see figure 1, spans from 1100m to 2200m in elevation with the lower reaches being dominated by sagebrush steppe and the higher elevation by conifers, junipers and aspens. Across this elevation gradient the precipitation form and amounts also vary with rain dominating the lower elevations and snowpack at high elevations. Geologically it is a granitic overlain by Tertiary volcanic rocks [*McIntyre*, 1972] with both volcanic and granitic bedrock and weathered material exposed throughout the watershed. This variability provides ample opportunity to apply hydrogeophysical methods and the dense instrumentation fortifies the geophysical methods with a wide variety of supplemental data.

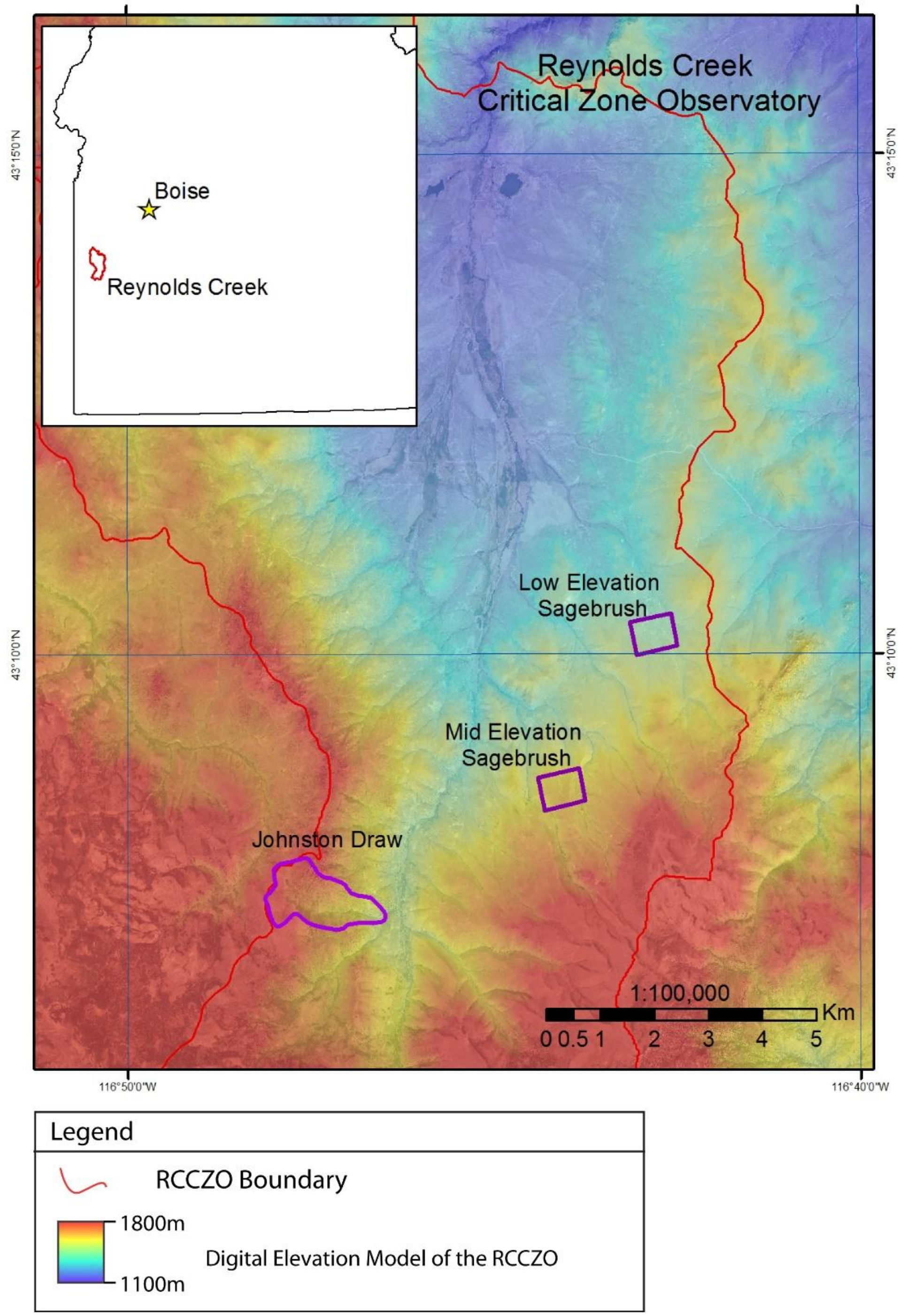

Figure 1: **Overview of the Reynolds Creek Critical Zone Observatory and its location in south western Idaho. The study sites are outlined in purple and a digital elevation model overlays a satellite image of the Reynolds Creek watershed.**

In my thesis, I present two hydrogeophysical imaging studies to explore different CZ phenomena. The first study is an SRT survey of the granitic Johnston Draw catchment to explore the influence of elevation, aspect and snow accumulation on weathering. As discussed earlier, micro-climactic properties play a large role in the rate of weathering and there properties vary with elevation and aspect. Johnston Draw is an east-west trending catchment, thus north and south facing slopes host very different microclimates, with the northerly aspect hosting denser vegetation and greater snow accumulation than the southerly aspect [*Anderson et al.,* 2014]. Further, the drainage of the catchment spans 300m in elevation so the micro-climates on both slopes vary from outlet to headwater with generally greater snow accumulation and vegetation density at higher elevations. This micro-climactic variability makes Johnston Draw an exceptional place to explore the relationship between snow accumulation and elevation on weathering extent. Johnston Draw also has been heavily instrumented with 3 sets paired of hydrologic instruments, each set placed at the same elevation but on the opposing aspects. These paired instrument sets span a large portion of Johnston Draw (figure 2) and thus allow for us to discern how the microclimates change on both aspects throughout the draw. This better informs the interpretation of the CZ architecture within Johnston Draw. I gathered four seismic lines each running perpendicular to the direction of drainage at varying elevations throughout Johnston Draw.

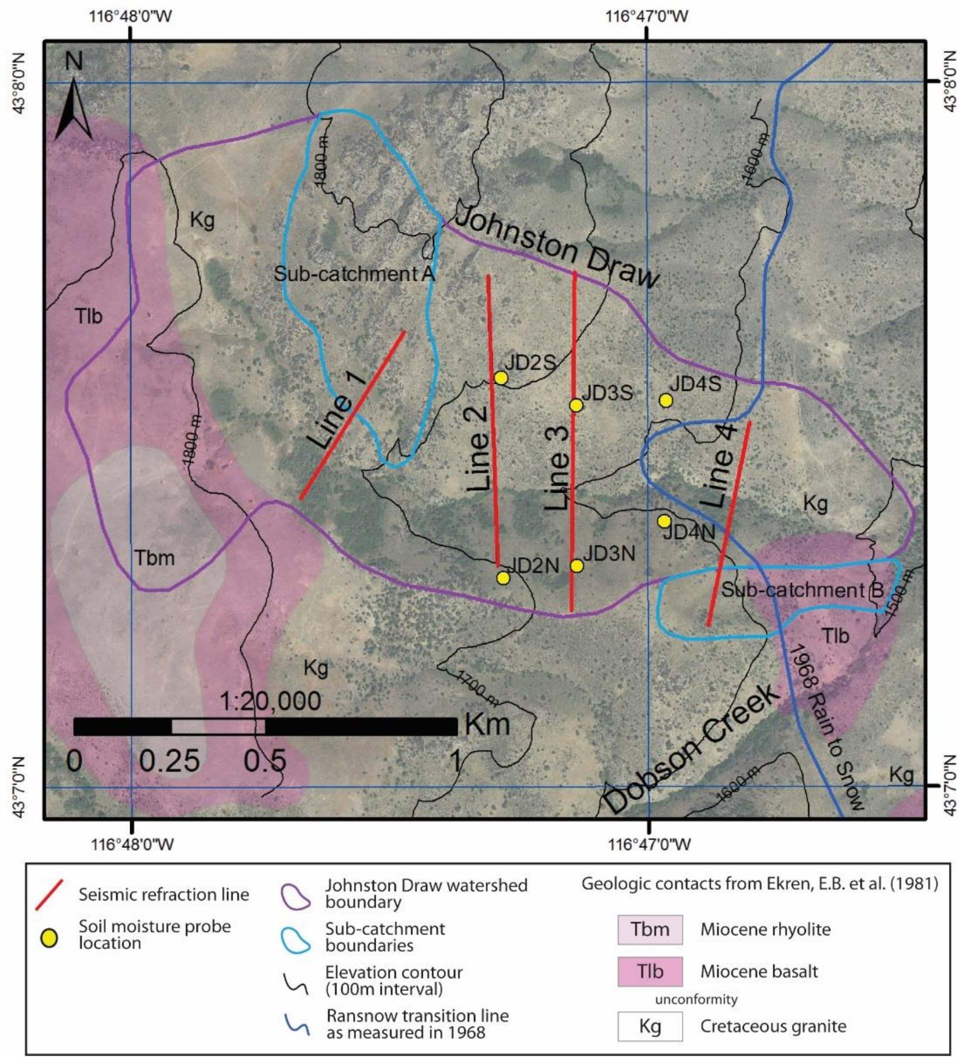

Figure 2: Satellite map of the Johnston Draw watershed seismic survey in the Reynolds Creek Critical Zone Observatory. The yellow circles are the locations of soil moisture, snow depth and soil temperature instruments (figures 2, 3, and 4), and the red lines are the locations of the seismic surveys (figure 7 and 8). Also shown are 100m elevation contours as thin black lines, the 1968 rain/snow transition as a blue line, and the outlines of the Johnston Draw watershed and sub-catchments A and B. The pink areas are the surficial exposures of volcanic rock and the transparent areas granitic rock.

My second study is a pair of time-lapse 3D ERT surveys of the upper ~1.5m of soil to observe seasonal and precipitation driven soil moisture changes. Soil moisture has been shown to be spatially and temporally heterogeneous while also being difficult to characterize using *in situ* methods, however the distribution of soil moisture has hydrological impacts on hillslope connectivity. To observe this heterogeneity in the RCCZO, ERT arrays were installed at the Low Elevation Sagebrush (LES) and Mid Elevation Sagebrush (MES) sites, at 1406m and 1653m in elevation respectively. Each of these sites is heavily instrumented and well-studied, with soil volumetric water content, soil temperature, precipitation and a whole host of other parameters being continuously measured. This robust dataset hydrologic measurement allows for the interpretation ERT results to be informed by the sites hydrology. In addition to the time-lapse 3D ERT surveys, 2D ERT and seismic refraction tomography surveys were conducted at the sites. The 2D geophysics provides information about the broader CZ structure, thus giving spatial context to the detailed observations made with the 3D arrays. While there have been other electrical surveys conducted at the RCCZO [i.e. *Robinson et al.*, 2012; *Niemeyer et al.*, 2017], this is the first high temporal density 3D ERT surveys conducted at the site and the first known ERT study of the sagebrush steppe.

CHAPTER TWO: GEOPHYSICAL INVERSTIGATION OF THE EFFECT OF ASPECT AND ELEVATION ON CRITICAL ZONE ARCHITECTURE

Abstract

In snow dominated mountainous watersheds it is commonly observed that the northerly facing slopes are more deeply weathered than the southerly facing slopes. This has been attributed to the unique insulating and water storage properties of snow that accumulate more heavily on northerly aspects. Johnston Draw is an east draining catchment within the Reynolds Creek Critical Zone Observatory that spans a 300m elevation gradient. The north facing slope hosts a persistent snowpack that increases in volume up drainage. While the south facing slopes has intermittent snow pack. I hypothesize that the largest difference in weathering depth between the two aspects will occur where the difference in snow accumulation between the aspects is also greatest. In order to test this hypothesis, I conducted four seismic refraction tomography surveys within Johnston Draw from inlet to outlet and perpendicular to drainage direction. From these measurements, I calculate the weathering zone thickness from the P-wave velocity profiles. I conclude that the maximum difference in weathering between aspects occurs ¾ of the way up the drainage from the outlet where the difference in snow accumulation is highest. Above and below this point, the subsurface is more equally weathered and the snow accumulations are more similar. I also observed that the thickness of the weathering zone increased with decreasing elevation. This supports the hypothesis that deeper snow

accumulation leads to deeper weathering when all other variables are held equal. This result does not account for the possibility that the denser vegetation on the north facing slope are contributing to the deeper weathering on the north facing slopes, via soil retention or higher rates of biological weathering.

Introduction

The critical zone (CZ) is the portion of the crust where bedrock is weathered into biologically usable soils. This process is an intricate interaction of physical, chemical and biological processes that leads to extreme structural heterogeneity both vertically and laterally. Generally the CZ can be broken into distinguishable vertically arranged layers of soil, saprolite and fractured bedrock[*Anderson, S.P. et al.*, 2007; *Brantley et al.*, 2007]. The combined regional tectonic stress and localized topographic stress creates a characteristic total stress field which controls fracture opening [*St. Clair et al.*, 2015]. This creates a basic critical zone pattern for a geomorphic region that is then acted on by other processes [*Riebe et al.*, 2016] such as climate [*Millot et al.*, 2002; *Riebe et al.*, 2004b], altitude [*Riebe et al.*, 2004c], hydrology[*Dunne*, 1998; *Lebedeva and Brantley*, 2013; *Hinckley et al.*, 2014; *Rempe and Dietrich*, 2014; *Langston et al.*, 2015], and biological processes[*Moulton and Berner*, 1998; *Amundson et al.*, 2007; *Gabet and Mudd*, 2010; *Roering et al.*, 2010]. Some of these later processes, climate, hydrology and biology, vary with aspect and elevation, thus within a large enough catchment the controls on CZ structure vary. In this study how elevation, aspect and the resulting differences in snow accumulation affect CZ structure is investigated using seismic methods within an east draining catchment.

At its most basic, chemical weathering is controlled by the ability to flush chemically stagnant water from bedrock pores and replace it with reactive water [*Maher*, 2010; *Rempe and Dietrich*, 2014] which is in turn controlled by the conductivity and density of fractures to act as fluid conduits[*Molnar et al.*, 2007; *St. Clair et al.*, 2015] and the amount of fluid input into the hillslopes. At the scale of individual hillslopes it is assumed that precipitation is distributed equally. However, hillslopes of varying aspects have different amounts of radiation input leading to differences in snow accumulation, soil temperature, and vegetation communities [*Anderson et al.*, 2014], all of which can affect the amount and reactivity of the water that infiltrates into the deeper CZ. Whether these hydrologic differences leads to more extensive weathering on the northerly or southerly aspects is a function of whether the site is limited by the reactivity or availability of meteoric water [*Ma et al.*, 2013]. In regions where water is input equally into all aspects, the higher solar radiation input to the more south facing slopes leads to higher rates and degrees of weathering[*Rech et al.*, 2001; *Ma et al.*, 2013]. However in snow dominated catchments the aspects with persistent snowpack are observed to have more extensive weathering than hillslopes with intermittent snowpack [*Hunckler and Schaetzl*, 1997; *Egli et al.*, 2006; *Befus et al.*, 2011; *Anderson et al.*, 2014]. Hunckler and Schaetzl (1997) and Elgi et al. (2006) posited that the aspect weathering difference is due to snow acting as an insulating layer, allowing for more continuous infiltration during the winter. Befus et al. (2011) suggested that the higher soil moisture retention and denser vegetation increases the rate of weathering and soil retention on the northerly aspect. Anderson et al. (2013) proposed a mechanism in which the cooler temperatures on the north facing slopes cause frost cracking damage which in turn promotes downslope transport of soils and generates fluid flow paths. When the frost cracking process was modeled, Anderson et al. (2013) showed that frost cracking lead to deeper weathering on the north facing slopes over the 10ka to 100ka time scales. Observations of soil water infiltration in the snow dominated Gordon Gulch in the Boulder Creek Critical Zone Observatory (BCCZO) showed that the persistent snowpack on north facing slopes led to a single sustained infiltration pulse in the spring while the intermittent snowpack on south facing slopes lead to periodic infiltration pulses through the winter[*Hinckley et al.*, 2014; *Langston et al.*, 2015]. Numerical modeling of unsaturated flow through a granitic CZ model suggested that a sustained single infiltration pulse characteristic of persistent snowpack leads to more water infiltrating into the deeper CZ than the episodic recharge events, thus increasing the relative rate of chemical weathering [*Langston et al.*, 2011, 2015]. Snow insulation, frost cracking, and recharge pulse shape hypotheses provide plausible explanation for deeper weathering on north facing slopes. Without direct observation of moisture flux into the deep CZ in hillslopes dominated by rain and snow how snow affects the weathering process cannot be conclusively factors. That being said there is enough observation of deeper weathering on snow dominated hillslopes to conclude that snow or a snow-related process is a driver of this asymmetry.

Elevation has been shown to affect weathering extent and rate of soils. Above the snow line at the Santa Rosa Mountains Reibe et al. (2004a) attributed the observed decrease in chemical weathering rates of soils at higher elevations to the decrease in mean soil temperature in combination with decreases in vegetative cover and an increase in snow cover. Dahlgren et al. (1997) and Rasmussen et al. (2010) observed an increase in soil development with elevation peaking at the rain-snow transition, above which the soil development decreased. Rasmussen et al. (2010) postulated that below the rain-snow transition the weathering is limited by water and above the transition it is limited by soil temperature thus at the rain-snow transition soil development is maximized.

With the myriad of potential controls on weathering within a single catchment, the depth of weathering will change both with aspect and elevation. However, measuring weathering depth at the catchment scale is challenging. Hand auguring and soil pits can provide measurements of weathering extent for the upper two meters and have been applied to the catchment scale [e.g. *Hunckler and Schaetzl*, 1997; *Egli et al.*, 2006]. Cored wells provides information on the deeper CZ [*Jin et al.*, 2010; *Olona et al.*, 2010; *Buss et al.*, 2013], but due to the cost it is difficult to apply with enough density and scale to provide a broad scale image of the deeper CZ. Geophysical methods such as seismic refraction tomography (SRT), electrical resistivity tomography (ERT), ground penetrating radar etc., trade the fine detail of the direct sampling methods for a spatial broad image of physical parameters such as seismic velocity, electrical resistivity, dielectric permittivity. SRT is particularly well suited for providing a constraint on regolith thickness since the weathering process reduces P-wave velocity (Vp), thus for a uniform geology, the velocity typically increases with depth, a first order assumption in most refraction methods [*Parsekian et al.*, 2015]. Further, granitic weathering studies have shown relatively consistent correlations between seismic velocity and weathering degree across several sites making the interpretation of SRT straightforward [e.g. *Olona et al.*, 2010; *Yamakawa et al.*, 2012(a); *Holbrook et al.*, 2014].

Interest in using geophysical methods to characterize the CZ for geomorphic analysis [*Thomas*, 1966] and to apply weathering correction to seismographs

[*Balachandran*, 1975] is long standing. Recently the increasing affordability and accessibility of geophysical methods has spurred researchers to apply geophysics to a number of CZ related phenomena. Studies have used geophysical methods to extrapolate engineering parameters [*Olona et al.*, 2010], hydrogeologic information [*Holbrook et al.*, 2014], to discern soil thickness [*Yamakawa et al.*, 2012a], bedrock depth [*Vignoli et al.*, 2012] and to characterize CZ architecture [*Befus et al.*, 2011; *Leopold et al.*, 2013]. Most of these studies are limited to a handful of slope parallel surveys that characterize a single hillslope however Befus et al. (2011) and Leopold et al. (2013) conducted multiple geophysical surveys spanning the width of catchments within the BCCZO, creating a catchment scale image of CZ architecture. Befus et al. (2011) used shallow seismic refraction (SSR) to investigate geomorphic controls on CZ architecture in Gordon and Betasso Gulch while Leopold et al. (2013) corroborated the SSR collected by Befus et al. (2011) with ERT providing a highly detailed but more difficult to interpret image of the CZ. For the sake of brevity in this paper, the difference in depth to a weathering horizon between the north and south aspects will be referred to as north-south (N-S) weathering depth asymmetry. Within east-west running Gordon Gulch they observed greater N-S weathering depth asymmetry in the steep lower catchment and less N-S weathering depth asymmetry in the shallower gradient hillslopes higher in the catchment. The decrease in N-S weathering depth asymmetry at the higher elevation was attributed to more equal radiation input into the hillslopes. N-S asymmetry was also seen to lesser extent in Betasso Gulch which drains to the south-east and is subject to an increased incision rate lower in the catchment complicating the effect of aspect on weathering. In both catchments the difference in weathering between the two slopes changed throughout the drainage, the N-S weathering asymmetry being larger near the outlet in Gordon Gulch and smaller near the outlet in Betasso Gulch. Why the N-S asymmetry changes in each catchment is different, demonstrating how geophysics can be used to elucidate the controls on weathering depth and how they can vary within and between catchments.

In this study SRT is used to investigate the CZ architecture of Johnston Draw which is a sub-catchment of the Reynolds Creek Critical Zone Observatory (RCCZO) in southwestern Idaho. Johnston Draw is east-west trending, almost completely granitic, has had no recorded Pleistocene glaciation or peri-glaciation, and is host to a persistent winter snow drift that increases in both width and depth up drainage. Because of these factors, Johnston Draw offers a unique opportunity to study the effect of aspect, elevation, snow accumulation, and soil temperature on CZ architecture with minimal complicating factors. I aim to investigate how variations in snow accumulation and soil temperature reflect weathering depths. This is the first catchment scale geophysical survey within the RCCZO and adds a valuable dataset for the other scientists studying Johnston Draw and Reynolds as a whole. The survey presented here adds to the growing body of geophysical data in mountainous critical zone sites and provides a more full perspective of catchment wide weathering architecture.

Site Description

The Reynold Creek Critical Zone Observatory (RCCZO) is in the Owyhee Mountains of southwestern Idaho, approximately 80km southwest of Boise, Idaho. The RCCZO ranges from 1100m to 2200m in elevation with regions of flat alluvial valleys and steep mountain slopes, figure 1. Due to the range in topography and elevation the RCCZO has a strong climactic gradient along different aspects and elevations. This climactic range is expressed in the variety of plant communities spanning desert shrubs in the low elevations to dense conifers at higher elevations [*Seyfried et al.*, 2000]. The surficial geology of the RCCZO is Cenozoic volcanic rocks all underlain by a Cretaceous age granite stock of the Idaho Batholith [*McIntyre*, 1972].

Johnston Draw is on the western flank of the RCCZO (figure 1). The draw trends east-west with an ephemeral stream draining towards the east. The stream bed varies in elevation from 1490m at the outlet to 1800m at the headwaters; the ridges to the north and the south have a topographic high of 1840m and 1860m, respectively. Johnston Draw is primarily composed of granite but intersects rhyolite units to the east and west [*Ekren et al.*, 1981]. The seismic lines in this study do not intersect the rhyolite (figure 2). During a typical winter a snow drift forms on the north facing slope of Johnston Draw, the drift increases in size higher in the drainage while the south facing slope hosts only intermittent snow that increases in persistence up drainage. Both the north and south facing slope nearer to the outlet are dominated by junipers, sage and grasses; higher in the drainage the north facing slope becomes vegetated by shrubs and aspens, while the southern aspects are dominated by junipers, sages, ponderosa, and grass.

Measurements of volumetric water content of the upper 20cm indicate that the shallow soils of the two aspects contain a highly variable amount of water (figure 3). The locations of the instruments are shown as yellow dots in figure 2 and are paired sites, each pair located at equal elevation on opposite aspects. While the two slopes may have similar shallow soil moistures they may have different rates of infiltration to the deeper CZ. Similar to what was observed by [*Langston et al.*, 2015] in the BCCZO northerly aspects the north facing slopes within Johnston Draw experience recharge in a single pulse at the end of March while the south facing slope experienced a primary recharge event in mid-January followed by several smaller events (figure 3). While there is a clear contrast in infiltration pattern between aspects, the 2012 water year is shown in this study as the contrast is exceptionally evident. Acoustic snow depth sensors adjacent to the soil moisture sensors show that for the 2012 water year the first measurable snow accumulation was on November 12th at all sites (figure 4). The amount of time snow covers the ground can be seen to increase higher in the drainage with nearly continuous snow coverage at the highest north facing site JD2N. The soil temperature was also recorded at all of the sites and the temperatures at 5cm depth are shown in figure 5. The thin blue and red lines are the temperature on the north and south facing slopes and the thick lines identify the times in which the soils are between -8°C and -3°C, which is the window of most efficient frost cracking in granites [*Anderson et al.*, 2013]. All of the north facing slopes spends time within the frost cracking window and the maximum time spent occurs on the lowest elevation north facing slope (table 1). However if the temperature window in which frost cracking is assumed to occur is increases to -8°C and 0°C then the highest elevation north facing slope spends the most time in the frost cracking window.

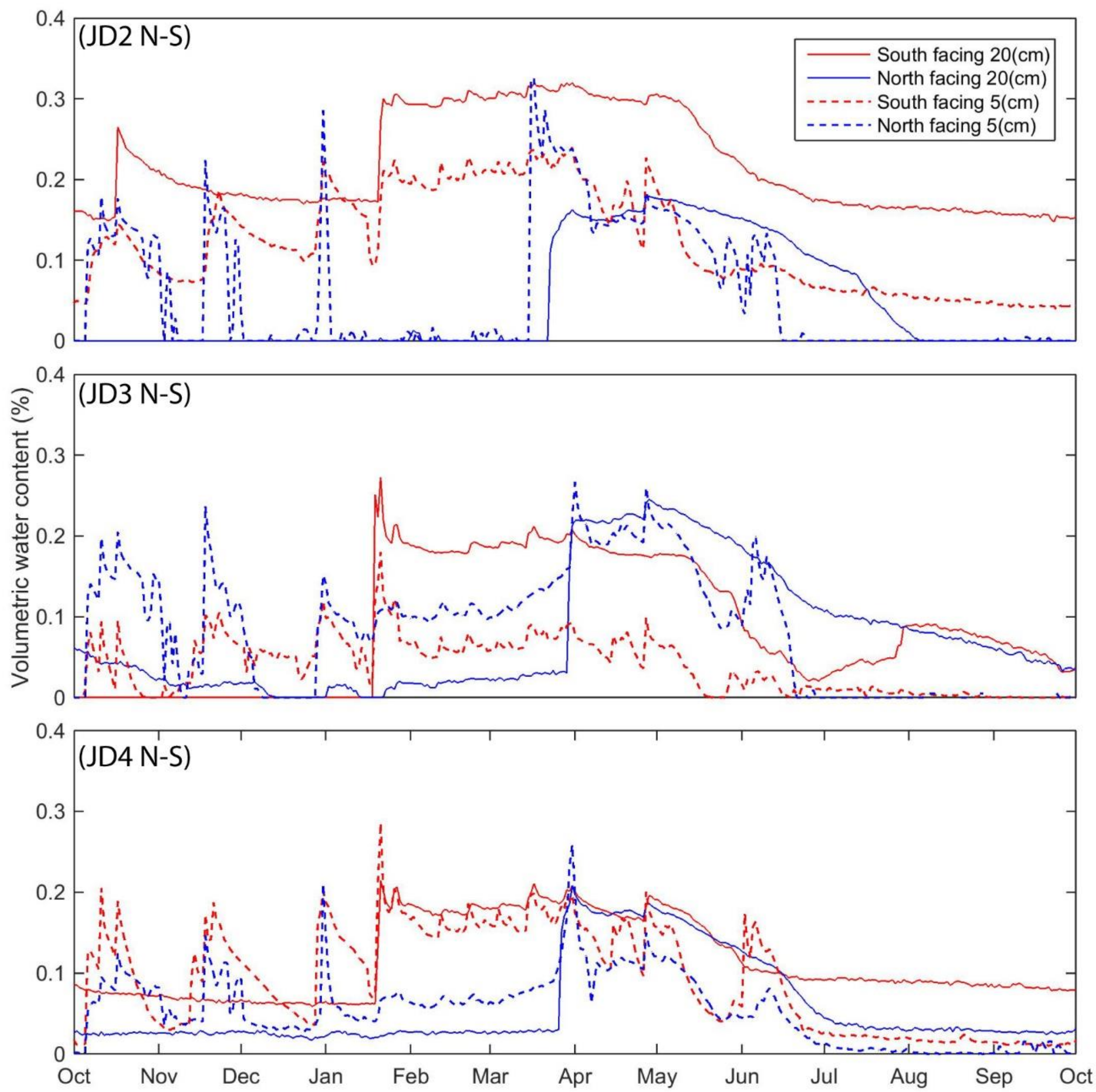

Figure 3: **Volumetric water content at 5cm and 20cm depth measured at the JD2(N-S), JD3(N-S), and JD4(N-S) instrument sites for the 2012 water year. The blue and red lines indicate the instruments on the north and south facing slopes, respectively; and the solid and dashed lines indicate 20cm and 5cm of depth, respectively. In the winter months the south facing slope are continuously wet while the north facing slopes remain dry, because of below freezing soil temperatures, until late March at which time moisture in_ltrates into the soil column in a single large pulse.**

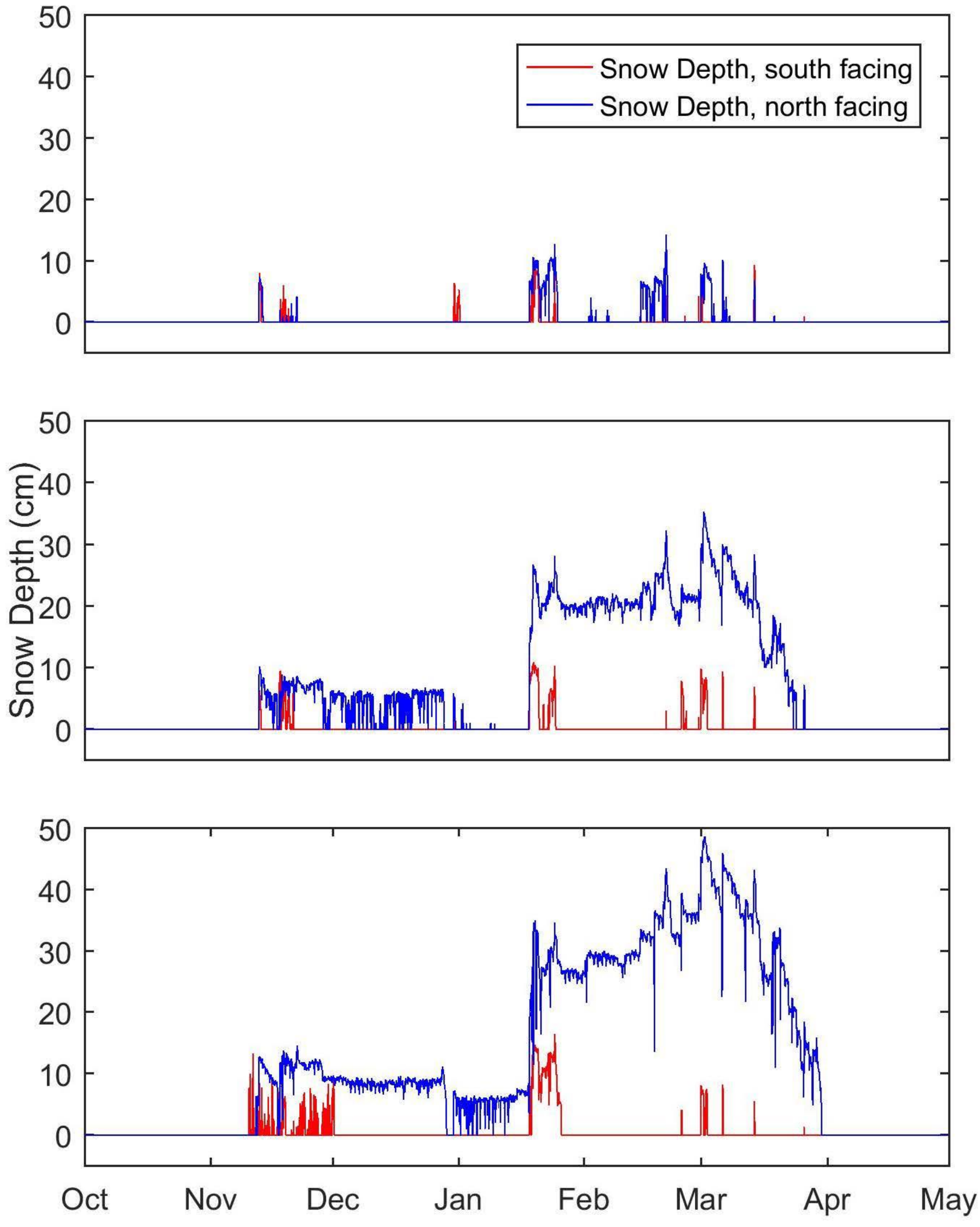

Figure 4: Snow depth measured with acoustic sensors at the JD2(N-S), JD3(N-S), and JD4(N-S) instrument sites for the 2012 water year. The blue and red lines indicate the instruments on the north and south facing slopes. The amount of snow and time it covers the ground increases up drainage for both aspects and the difference in total snow accumulation between the aspects increases up drainage.

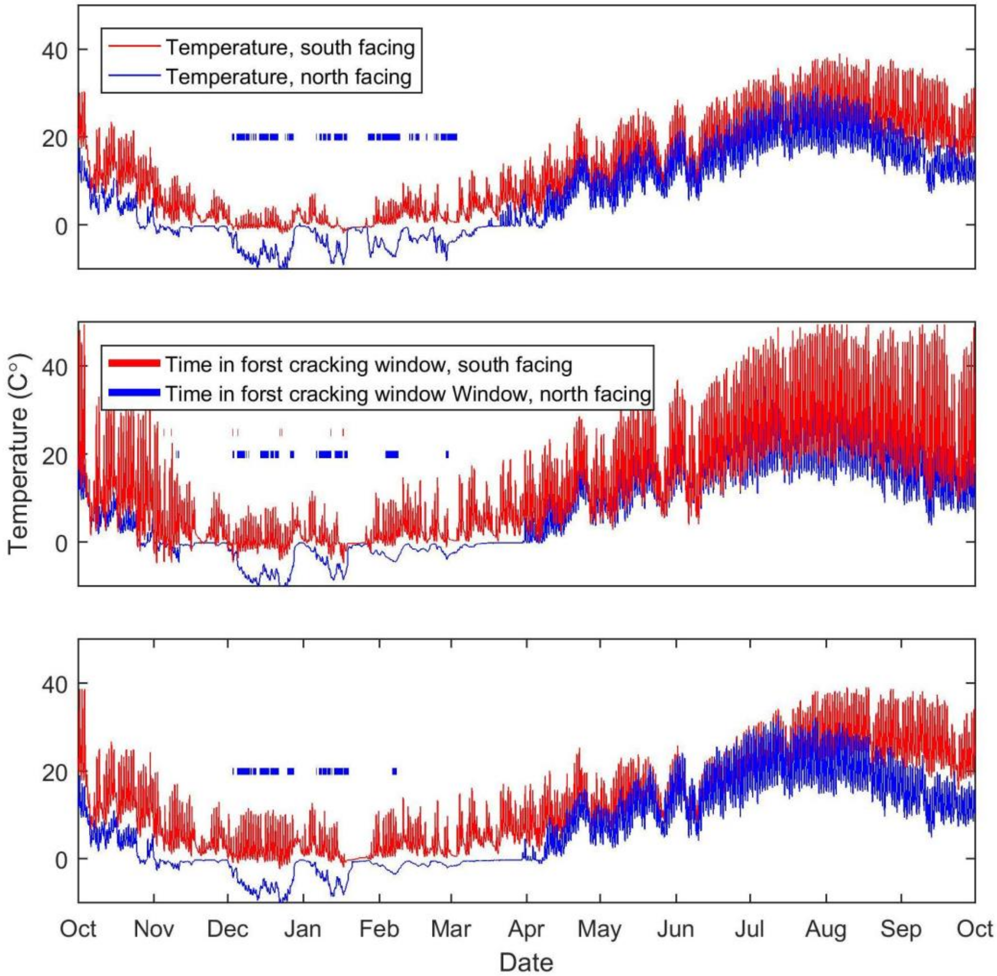

Figure 5: Soil temperature measured at 5cm depth with TDR probes at the JD2(N-S), JD3(N-S), and JD4(N-S) instrument sites for the 2012 water year. The blue and red lines indicate the instruments on the north and south facing slopes, the thick red and blue lines indicate times then the sensors were between -3°C and -8°C.

Table 1: The time in hours the soils at 5 cm depth spend in various temperature windows, measuredat the north facing (N.F.) and south facing (S.F.) paired instrument sites during the 2012 water year. All of the north facing soils spend time within the -8°C to -3°C however the lowest elevation north facing site (JD4N) spends the most time in the window. If the window is increased to -8°C to 0°C then the highest elevation north facing site (JD3N) spends the most time in said the window.

Temp. Window:	-8°C and -3°C		-8°C and 0°C	
	N.F.	S.F.	N.F.	S.F.
JD4 (hrs)	300	0	840	200
JD3 (hrs)	180	14	850	240
JD2 (hrs)	185	0	910	75

Methods

To investigate the CZ architecture within Johnston Draw four seismic lines were gathered in the summers of 2014, 2015, and 2016. The seismic lines start at or near the top of the south ridges of the draw and extend to the north ridge (figure 2). The lines were set to be perpendicular to the direction of drainage and placed such that they avoided bedrock outcrops and dense vegetation. Additional care was taken to ensure that they remained as straight as possible so that continuous seismic profiles were maintained. Line 1, at the top of the draw, was gathered by the Wyoming Center for Environmental Hydrology and Geophysics, University of Wyoming in the summer of 2014 using four 24-channel Geometric Geodes systems with a receiver spacing 2.5m and shot spacing of 10m. Because the spread of the array is less than the width of the draw, the array was deployed twice with shots off the end of the line performed for 50m in the to-be occupied or reoccupied shot locations. Lines 3 and 4 were gathered in the late summer and fall of 2015 and Line 2 in the summer of 2016 by the Center for Geophysical Investigation of the Shallow Surface, Boise State University using five 24-channel Geometric Geode systems with a 5 m receiver spacing and 20 m shot spacing creating an array of five 120m segments. In order to span the width of the draw segments of the line were leap

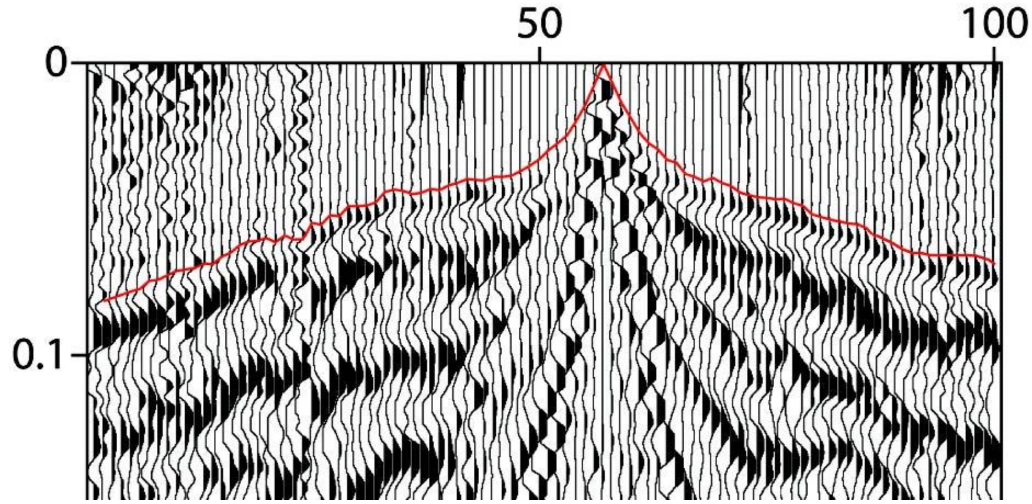

Figure 6: An example shot break from Line 3 with the picked first arrivals shown as a red line. The shot was located midway up the south facing slope, at approximately the 100(m) mark in figure 7c.

frogged; i.e. shots were performed on the southernmost segment which was then moved to the northern end of the line, shots were then performed on the new southernmost segment which was then moved to the northern end of the line. This process was repeated until the array reached the opposite ridge at which point shots were performed through the array. The seismic source was a 10lb sledge hammer swung against an aluminum plate and nine strikes were stacked into one shot.

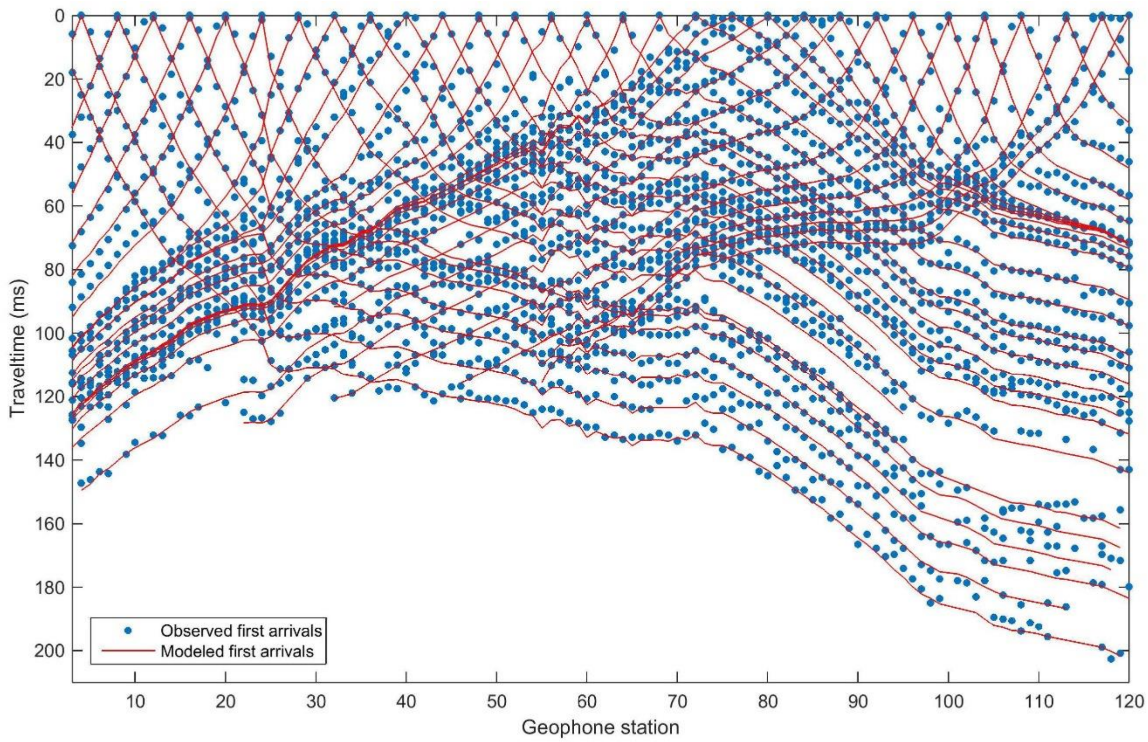

Figure 7: Observed and modeled first arrival travel times for Line 4. Generally the observed and modeled travel times are in good agreement, however at the far and near offset receivers the fit becomes more tenuous as the first arrivals are more difficult to pick.

I picked first arrivals as the first motion that could be confidently attributed to either the refracted or direct seismic wave arrival. An example shot break for Line 3 with the picked first arrivals is shown in figure 6. I then estimate the subsurface seismic velocities by inverting the first arrival times using the commercial software Rayfract which employs a wavepath eikonal traveltime (WET) inversion to partial account for band-limited frequency effects [*Schuster and Quintus-Bosz,* 1993]. The initial models for the inversion were derived by taking a Delta t-V for each receiver location and averaging the velocities at common depths, creating a pseudo-2D Delta t-V inversion[*Jansen,* 2010]. WET inversion with the pseudo-2D Delta t-V initial model has proven to be an effective inversion schema at resolving large scale near-surface velocity features[*Zelt et al.*, 2013] and for the estimation of smooth critical zone velocity structures [*Nielson and*

Bradford, 2015]. The inversions were carried out for 150 iterations,long enough for the RMS error to reduce to less than 3% of the maximum travel time of the modeled traces for all the inversion. The observed and modeled travel times for Line 4 are plotted in figure 7, which shows the observed arrivals as red dots and the modeled arrivals as blue lines. As can be seen the near offset picks do not fit as well as the medium offset picks. This residual arises because at geophones adjacent to the shot location it becomes difficult to discern the seismic arrivals from the air wave arrival thus reducing the precision of the near offset picks. A similar problem occurs at far offsets where the seismic wave has dispersed and attenuated thereby reducing the signal to noise ratio making it difficult to confidently pick the seismic arrival.

The resulting velocity profiles of these seismic lines were then interpreted using the weathering degree seismic velocity relationship from [*Olona et al.,* 2010], see Table 2. The mean depths to the seismic contours that correspond to the tops of weathering horizons were calculated for each seismic line and the individual hillslopes. I then compared how the weathering zone varied across elevations by comparing the mean depths of each seismic line and how the weathering zone varied across aspects by comparing the hillslopes.

Table 2: P-wave velocities for the weathering stages of granite as measured by Olona et al. (2010)

Description	P-wave velocity (m/s)
Disaggregated materials	<700
Saprolite	700-2000
Fractured Bedrock	2000-3500
Fresh Bedrock	>3500

Results

The resulting Vp profiles of the four seismic lines were analyzed to estimate depth to fractured and fresh bedrock. The depth to saprolite (700m/s) was also calculated, but as discussed later, is biased and incomplete. The depth to fractured (2000 m/s) and fresh bedrock (3500 m/s) is taken as the depth to the Vp contour that corresponds to the saprolite-fractured bedrock and fractured-fresh bedrock interfaces. The velocities for these interfaces are taken from Befus et al. (2011) and Olona et al. (2010) and are shown table 2. To compare the weathering between the north and south facing hillslopes the Vp profiles are split by the current drainage location. The mean depth and standard deviation of the mean to the weathering horizon is calculated for each hillslopes and each seismic line, the results are shown in table 3. It should be noted that the standard deviation in the mean depths is not a reflection of the error in depth measurement but the square root of the variance in the depths.

Table 3: Mean depth and standard deviation of the mean to fractured and fresh bedrock measured at each seismic line and hillslope. Down drainage both the mean depth to fractured and unweathered bedrock and the standard deviation of the mean increase.

	Mean Depth To Fractured Bedrock (m)	Mean Depth To Un-Weathered Bedrock (m)
Line 1	7±3	14±5
North Aspect	9±3	16±5
South Aspect	4±1	10±2
Int. North Aspect (N-2)	9±3	17±5
Int. South Aspect (S-2)	7±3	13±4
Line 2	11±5	23±6
North Aspect	17±4	31±7
South Aspect	9±3	21±4
Line 3	10±3	20±5
North Aspect	12±3	21±4
South Aspect	9±3	20±5
Line 4	16±6	31±11
North Aspect	16±6	31±11
South Aspect	16±5	31±10

The Vp profiles are shown as an orthographically correct fence plot in figure 8 with the top of fresh bedrock velocity (3500m/s) contour shown. The Vp profiles are shown again in figure 9 with the soil-saprolite (700m/s), saprolite-fractured bedrock (2000m/s), and fractured-fresh bedrock (3500m/s) velocity contours shown; note that a 3x vertical exaggeration is applied to Line 1 in figure 9a so that the velocity contours can be distinguished. As can be seen in figures 2, 8, and 9 the highest elevation seismic profile Line 1 covers two catchments, the primary drainage and sub-catchment A thus there are two sets of hillslopes to compare. The different hillslopes are given the names N1, S1, N1, and S2 (see figure 9a) for labeling. Line 4, intersects a small drainage on the south ridge, sub-catchment B, and as seen in figure 2 sub-catchment B drains into Dobson Creek and not Johnston Draw. The portion of the seismic profile underlying sub-catchment B is excluded from this analysis as it accumulates meteoric water that does not contribute to the weathering of the hillslopes within Johnston Draw. Further, as discussed later the weathering zone under sub-catchment B is anomalously deep and is likely caused by a pre-existing weakness so its inclusion in the analysis would introduce a control on weathering other than aspect, elevation, and snow accumulation. Thus for the north facing slope of Line 4 the mean depth to a weathering horizon is calculated from -115m to the drainage (figure 9).

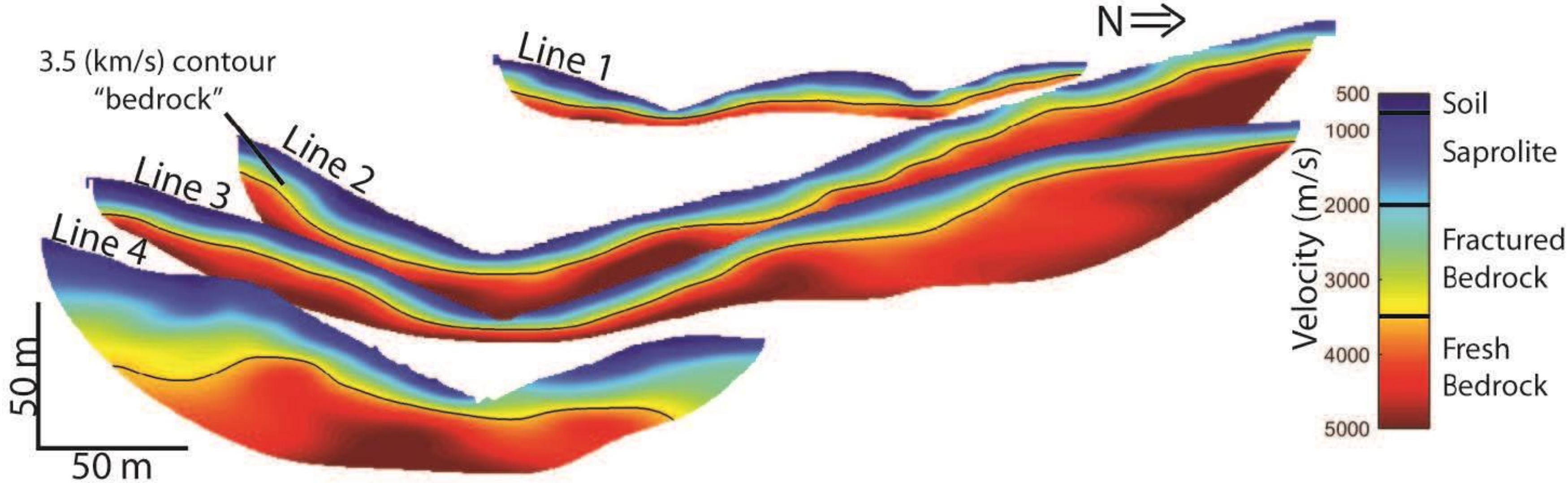

Figure 8 Fence diagram, looking up drainage, of the inverted velocity profiles within Johnston Draw with no vertical exaggeration. The black lines are the 3.5km/s velocity contour which we interpret as the top of unweathered bedrock.

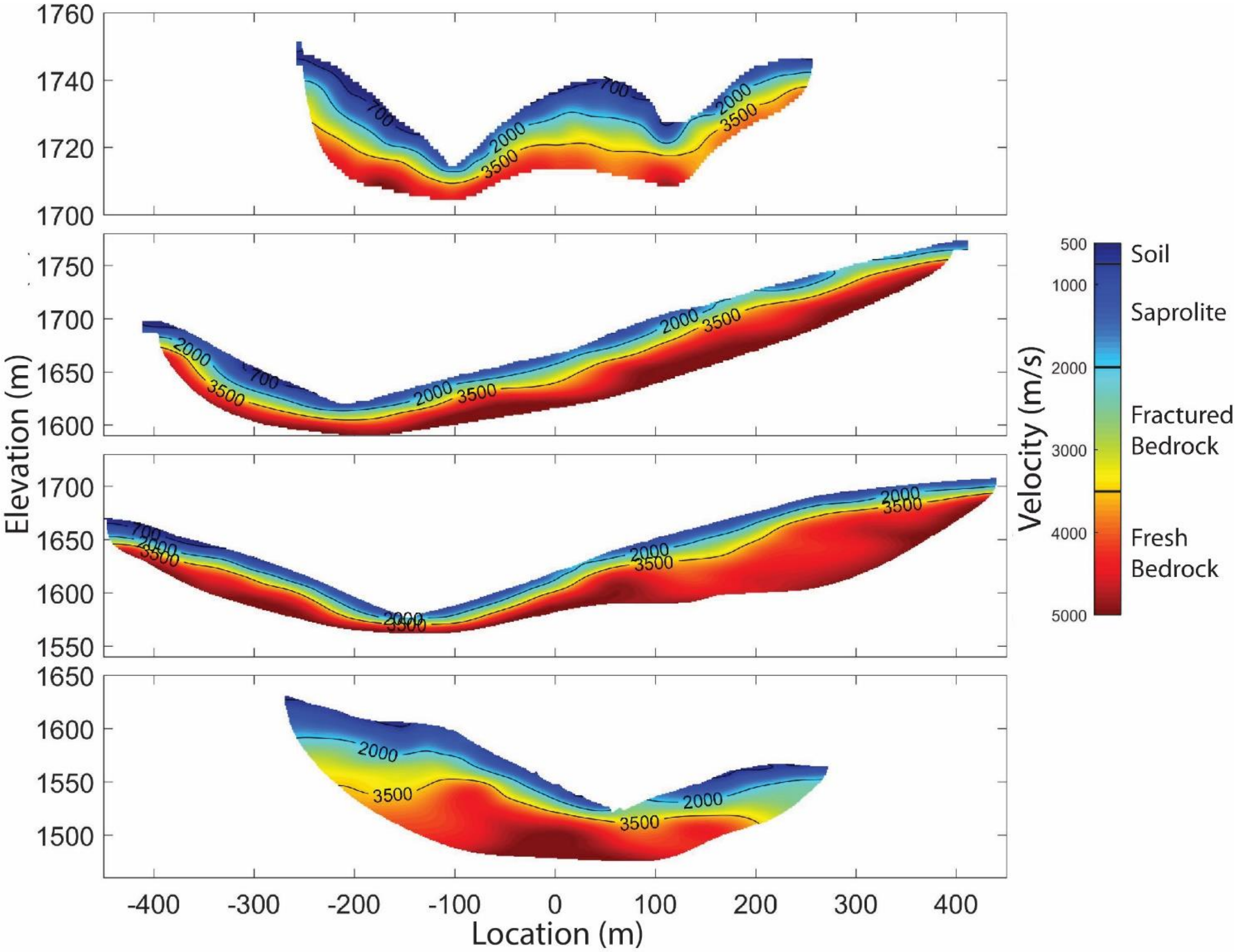

Figure 9: Inverted velocity profiles for the seismic refraction surveys conducted in Johnston Draw with the 700m/s, 2000m/s, and 3500m/s velocity contours shown as black lines. The velocity contours correspond to the top of saprolite, fractured bedrock and unweathered bedrock, the velocity ranges for these layers is shown in Table 2. Line 1 (a) is vertically exaggerated by 3 times while all the other profiles have no vertical exaggeration.

The mean depths to various velocity contours and the standard deviations of the mean for each seismic line is depicted in figure 10 and table 3, where the blue and red represent the north and south facing slopes, respectively. Generally within Johnson Draw the depth to fractured and unweathered bedrock increases lower in the drainage. The mean depth to bedrock is 31.1m at Line 4 and 13.8m at Line 1 and the depth to fractured rock the mean depth at Line 4 is 17.3m and at Line 1 is 7.3m. Unlike with the other horizons, soil depth doesn't increase down drainage rather the largest mean depth to the 700 m/s contour is on Line 3 at 4.4m, while Line 1, 2 and 4 the soil is on average 2.3m, 3.6m and 2.1m thick, respectively. However the top of saprolite contour, 700 m/s, is not continuous across all the profiles. This is because the receiver spacing's is too broad to receive distinct arrivals from the refracted or diving rays traveling through the relatively thin low velocity media near the surface.

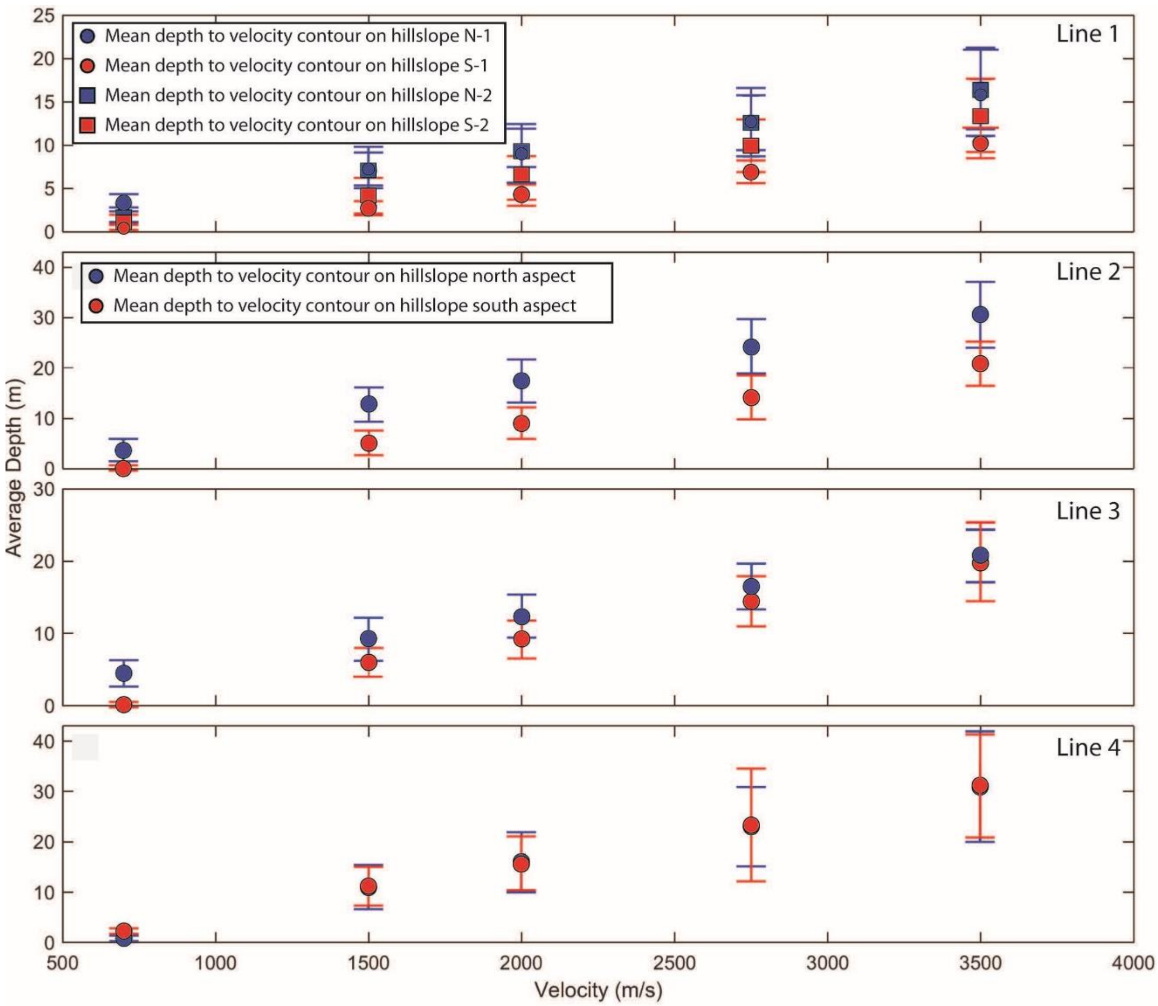

Figure 10: **Mean depth and standard deviation of the mean to various velocity contours for the north and south facing aspects, shown in blue and red, for each velocity pro_le. The 700m/s, 2000m/s and 3500m/s velocities correspond to the depth to top of saprolite, fractured bedrock, and fresh bedrock respectively. As can be seen in every line except Line 4 the mean depth to all velocity contours is greater on the**

north facing slope and the depths to fractured and fresh bedrock increase down drainage.

The water table could also influence the seismic velocities in the near surface. As the Vp velocity of water is roughly 1500m/s a high saturation in a low velocity high porosity media can increase the bulk seismic velocity. However within the CZ porosity decreases and dry seismic velocity increase rapidly with depth, decreasing the effect of water content on bulk Vp. Within the fractured and fresh bedrock the porosity is near zero thus the effect of pore-water is negligible and does not affect our analysis.

On every seismic profile except Line 4, the north facing slope is more deeply weathered than the south facing slope, at Line 4 the N-S weathering depth asymmetry is insignificant. The N-S weathering depth asymmetry is plotted on figure 11, this is the mean depth to the fractured and unweathered bedrock contours on the north aspect minus the mean depth to the same horizons on the south aspect. Because of the multiple drainages in Line 1, I calculated three differences, the difference in mean depths between N-1 and S-1 are circle, N-1 and S-2 are squares, and N-2 and S-2 are diamonds (figure 9a for reference). The maximum N-S weathering depth asymmetry is measured at Line 2 with the unweathered and fractured bedrock being about 10m and 8m deeper on the north facing slopes than the south. At the highest elevation, Line 1, the N-S weathering depth asymmetry for unweathered and fractured bedrock is N-1 and S-1 is 6m and 5m, respectively. Below at Line 3 the N-S weathering depth asymmetry for unweathered and fractured bedrock decreases to 1m and 3m and decreases again to about 0m for both horizons at Line 4. This pattern of bedrock weathering parallels the observed snow accumulation pattern as can be seen from the acoustic snow depths in Figure 4. The seismic derived weathering zone depths and the acoustic snow depths show a correlation between snow accumulation and depth to unweathered and fractured bedrock for hillslopes at the same elevation.

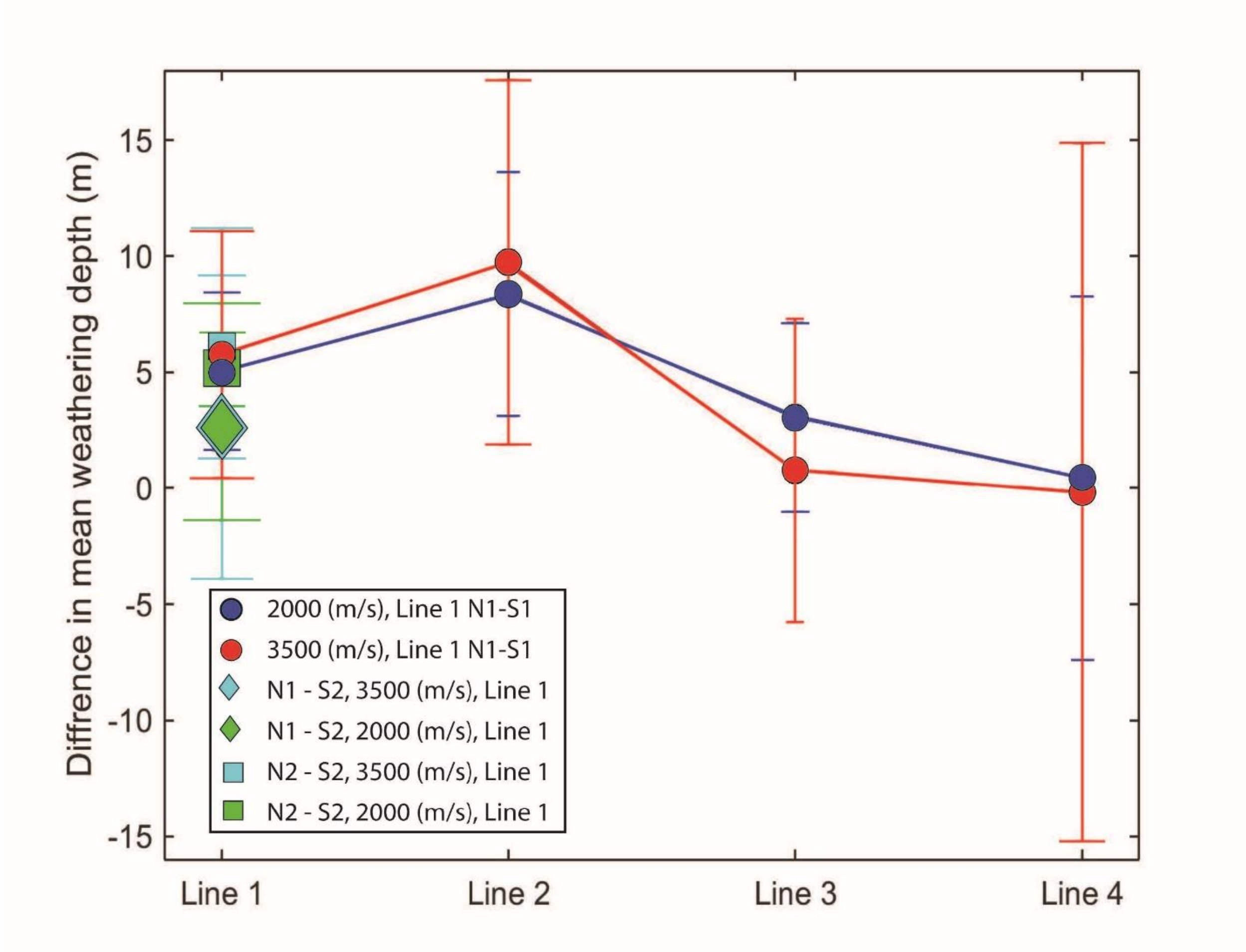

Figure 11: The N-S weathering depth asymmetry, i.e. the difference in mean depth to fractured (2000m/s) and fresh (3500m/s) bedrock between the north and south facing slopes. Because Line 1 spans two catchments there are two sets of hillslopes to analyze: they are shown as circles for the difference between hillslopes N1 and S1, diamonds for hillslopes N1 and S2, and squares for hillslopes N2 and S2. The highest N-S weathering depth asymmetry occurs at Line 2, above and below this the asymmetry decreases.

Discussion

Bedrock topography generally parallels surface topography with the weathered layer thinning near the drainage; this is similar to what was observed by *St. Clair et al.* (2015) in a neutral or extensive region. While there are no regional stress measurements in the Owyhee region *Payne et al.,* (2012) showed that the Snake River Plain and Owyhee-Oregon Plateau experience very low rates of deformation. Given the low rates of strain and the regions general extensive nature, it is unlikely that the Reynolds area is experiencing a significant amount of compressive stress. This bedrock topography pattern is also what is predicted by *Rempe and Dietrich* (2014) and *Lebedeva and Brantley* (2013), and is similar to what was observed at the BCCZO [*Befus et al.*, 2011; *Leopold et al.*, 2013].

There are several notable velocity anomalies in the Vp profiles: the low velocity anomaly in Line 3 at location 150 m, and to a lesser extent Line 2 at location 0 m; and the low velocity anomaly under sub-catchment B in Line 4, location -150 m. As can be seen in figure 8 the low-velocity anomalies in Lines 2 and 3 are relatively close to each other, suggesting that it is a continuous feature such as a set of fractures. Fractures would increase the weathering proximal to the fractures, creating a low velocity anomaly like the one seen in Lines 2 and 3.

The weathering zone under sub-catchment B is unusually thick with the top of unweathered bedrock being ~65m deep. This is much thicker than the weathering zone in the other profiles (figures 8 and 9d). A possible interpretation is that it is pre-existing fractures or weakness in the bedrock that has created an area of faster weathering, that then increased mass transport causing a depression. If it is included in the mean depth of the north facing slope of Line 4 it greatly increases the calculated N-S weathering depth asymmetry in the lower portion of Johnston Draw. However as discussed earlier Sub-catchment B drains into Dobson Creek not Johnston Draw, thus the precipitation inputted into the sub-catchment does not contribute to the weathering of the north facing slope in Line 4. It is possible that at a previous time sub-catchment B either didn't exist or drained into Johnston Draw. But as discussed the weathering is anomalously deep and is likely caused by a pre-existing structure. Therefore it's inclusion in the analysis would detract from the focus of this study, so is excluded from the N-S weathering asymmetry analysis.

For the majority of the catchment, Lines 2-4, the N-S weathering depth asymmetry increases higher in the drainage. However from Line 2 to Line 1 the N-S weather depth asymmetry decreases (figure 11). Between Lines 2 and 1 the direction of drainage shifts from east to south-east. Thus the hillslopes spanned by Line 1 face north-east and south-west rather than north and south as the rest of Johnston Draw does. Additionally (as can be seen in figure 7) the slope gradient is less at Line 1 than it is at the other lines. *Befus et al.* (2011) observed a similar decrease in N-S weathering depth asymmetry at the headwater of Gordon Gulch and similarly attributed it to the lower relief hillslopes higher in the catchment. This shift in aspect and slope gradient reduces the radiative difference between the hillslopes which likely leads to more equal distribution of snow between the aspects and more equal weathering. Unfortunately at Line 1 there are no paired instrument stations to measure snow depth, soil moisture, and soil temperature as there are at the other lines.

Within Johnston Draw the depth to unweathered bedrock increases lower in the drainage. Similar trends have been observed across elevation gradients with higher soil weathering rates [*Riebe et al.*, 2004c] and more soil development [*Dahlgren, et al.*, 1997; *Rasmussen et al.*, 2010] at lower elevations. Above the snow line at the Santa Rosa Mountains *Reibe et al.* (2004a) attributed the observed decrease in chemical weathering rates of soils at higher elevations to the decrease in mean soil temperature, in combination with decreases in vegetative cover and an increase in snow cover. *Dahlgren et al.* (1997) and *Rasmussen et al.* (2010) observed an increase in soil development with elevation peaking at the rain-snow transition, above which the soil development decreased. *Rasmussen et al.* (2010) postulated that below the rain-snow transition the weathering is limited by water and above the transition it is limited by soil temperature, thus at the rain-snow transition soil development is maximized. In Johnston Draw the 1968 rain/snow to snow transition occurred at about the same elevation as Line 4 (figure 2), which is where the greatest average depth to unweathered bedrock and fractured bedrock occurs (table 3). This suggests that elevation and dominant precipitation are a control on the depth to unweathered bedrock within Johnston Draw, similar to what was observed for soil weathering and development by *Dahlgren et al.* (1997), *Reibe et al.* (2004a), and *Rasmussen et al.* (2010). However the current dominant precipitation phase may not reflect the dominant precipitation pattern in the past. *Klos et al.* (2014) showed that the rain-snow transition in the western US has been moving higher since the 1960's and that this trend is likely to continue. Thus the 1968 rain-snow transition is likely not reflective of past precipitation phases. While no work has been done linking soil weathering degree to bedrock weathering depth, it is conceivable that more chemically depleted soils wouldn't react with incoming meteoric water as readily, thereby increasing the reactivity of the water propagating into the deep CZ increasing the rate of deep weathering. Some caution should be applied when comparing the deep weathering depths measured in Johnston Draw to the soil weathering and development measured at other sites, as both the magnitude of the depth of measurements and methods applied are very different. Making a causal link between dominant precipitation phase and depth to fractured or unweathered bedrock is tenuous.

Within Johnston Draw the north facing slopes are generally steeper than the south facing slopes, this can be seen in the surface topography of the velocity profiles in figure 8. The north facing slope are densely vegetated with mountain sagebrush, snowberry, and several aspen communities, while the south facing slope feature Wyoming sagebrush and bitterbrush at the lower elevations and sagebrush and mahogany at the higher elevations. Differences in slope angle can be attributed to denser vegetation communities on the north facing slope, increasing soil retention relative to the less densely vegetated south facing slopes [*Poulos et al.*, 2012].

Our observations do not exclude the possibility that the factors that control snow accumulation patterns, i.e. vegetation and radiation, are the factors that cause deeper weathering on the north facing aspects and that the snow accumulation is coincidental. It is well documented that plants increase the rate of chemical weathering in soils [*Moulton and Berner*, 1998] and that deep taproots can fracture bedrock creating hydraulic pathways as well as detach bedrock blocks when bedrock rooted trees are overturned [*Gabet and Mudd*, 2010; *Roering et al.*, 2010]. Aspens have been seen to root as deeply as 3m [*Jones and Debyle*, 1985] and within Johnston Draw they are clustered higher in the catchment on the north facing slope, so they could very well be a contributor to the increase in N-S weathering depth asymmetry up drainage. However at the adjacent

Reynolds Mountain East site within the RCCZO it has been shown that tree groves both influence the location of a snowdrift [*Marks et al.*, 2002] and rely on the water derived from snowdrifts [*Robinson et al.*, 2008a]. Hence it could be that the snowdrift allows for the aspen community to exist and the deep rooting allows for more moisture to propagate into the deeper CZ. The persistent snow drift within Johnston Draw is centered roughly with Line 1, and could also be influencing the weathering on the north facing slope of the upper drainage.

Radiation is the primary control on snow distribution pattern and has been shown to effect on soil weathering rates by increasing soil temperature, thus in non-snow dominated environments leading to deeper weathering on the south facing slopes [*Rech et al.*, 2001; *Ma et al.*, 2013]. However Johnston Draw is primarily above the 1968 rain-snow transition and sees deeper weathering on the north facing slopes. Therefore differences in soil temperature from radiation contrasts alone, does not explain the CZ architecture within Johnston Draw. So while vegetation likely contributes to the N-S weathering depth asymmetry to some degree it is unlikely that radiation directly contributes, rather as it is a direct control on snow distribution it is an indirect factor.

The soil moisture data for the 2012 water year showed that the north facing slope recharged in a single pulse at the end of March, while the south facing slope experienced a primary recharge event in mid-January followed by several smaller events (figure 3). Numerical modeling of moisture infiltration into the deep CZ, has shown that the single sustained pulse characteristic of the north facing slope of Johnston Draw leads to more recharge in the deeper CZ than the episodic pulses characteristic of the southern aspect [*Langston et al.*, 2011, 2015]. This phenomenon has been proposed as a mechanism to explain N-S weathering depth asymmetry within Gordon Gulch in the BCCZO [*Langston et al.*, 2015], and would also explain the asymmetry observed within Johnston Draw. The difference in snow accumulation between the two aspects higher in the catchment would lead to a difference in the amount of water infiltrating into the deep CZ. This difference in infiltration would decrease down drainage as the snow accumulation becomes more equal between the aspects. As the ability to flush and replace chemically stagnant water from bedrock pores is a control on deep chemical weathering[*Maher,* 2010; *Rempe and Dietrich*, 2014], then the chemical weathering rates will parallel the infiltration rates. This would results in deeper weathering where the snow pack is deeper and more persistent. Therefore, as the difference in snow accumulation between the aspects decreases down drainage the difference in the rate of weathering between the two aspects would also decrease, leading to the observed N-S weathering depth pattern within Johnston Draw.

It is apparent that all the north facing slopes spend time within the frost cracking window (figure 5 and table 1). However if we assume the more time spent within the frost cracking window the greater the damage, then our temperature observations would suggest that the lower portions of the draw would have the greatest N-S weathering depth asymmetry. Rather we observe insignificant N-S weathering depth asymmetry where our temperature observations and frost cracking would predict the high asymmetry (figure 11). The exact range in which frost cracking is most efficient is dependent on the hydraulic and fracture mechanical characteristics of the rock [*Walder and Hallet,* 1986]. This suggests that the ideal frost cracking window for the granite within Johnston Draw could be different than -8°C and -3°C. The temperature window that does fit the observed

N-S weathering depth asymmetry is -8°C and 0°C. However near 0°C the van der Waal and electrostatic forces that cause frost cracking are weekend [*Hales and Roering*, 2007]. Further even if the frost cracking window is expanded the time spent in the expanded window (table 1) still indicates that at Line 4, the north facing slope should be more deeply weathered than the south facing slope. The aspect paired soil temperature measurements suggest that the frost cracking theory is not the primary driver of the weathering pattern that is observed with Johnston Draw.

The soil moisture patterns at the paired instrument sites (figure 3) within Johnston draw, suggest that the north facing slopes are receiving deeper infiltration than the south facing slopes. The temperature sensors indicate the soils are within the frost cracking window (figure 5). But the time spent within the window (table 1) is not reflective of the weathering pattern within Johnston Draw (figure 11). While it does appear the snow accumulation is the primary N-S weathering depth asymmetry observed, I propose that frost cracking could still play a role in the weathering pattern observed within Johnston Draw. Since frost cracking creates preferential flow paths on the northerly aspects, these preferential flow paths would exacerbate the difference in infiltration caused by the more persistent snow pack on the north facing. The seasonality of the hillslope hydrology is depicted in figure 12, the gray lines represent flow paths caused by frost cracking and the darker shades of blue high soil moisture. Before snow accumulation both aspects are in low flux state soil moisture. During the winter a persistent snow pack accumulates on the north facing slope. However the frozen soils and stable snow limit moisture infiltration. On the south facing slope the periodic accumulation and melt of snow leads to moderate moisture flux. In spring the snow on the north facing slope melts in a single sustained event, leading to a pulse of moisture infiltration on the north facing slope, while the south facing slope maintains moderate infiltration.

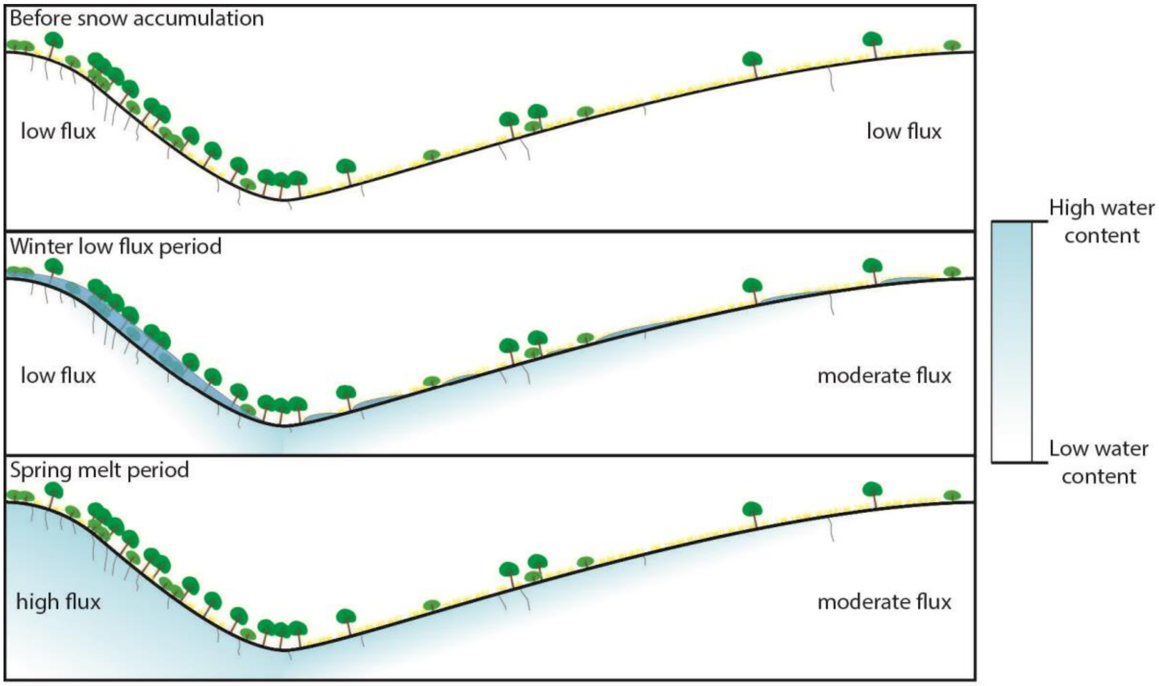

Figure 12: Illustration of how the soil and regolith damage from frost cracking could work in conjunction with the distinct soil infiltration patterns from a north facing hillslope with persistent snow pack and a south facing hillslopes with intermittent snow pack. The top panel is the hillslopes before snow accumulation, the north facing hillslopes have denser and larger vegetation communities and due to frost crack more preferential _ow path, denoted by the gray lines, through the soil and regolith. The middle paned depicts the hillslope in mid-winter in which the northerly aspect host a persistent snowpack however there is little moisture flux into the subsurface due to lack of snow melt, while the south facing slope has an intermittent snowpack that has been periodically melting leading to moderate moisture flux. The bottom panel is the hillslopes just after complete snow melt in during which the single melt event on the north facing slope and the high average conductivity has led to high moisture flux, while the south facing slope is still experiencing moderate moisture flux.

Conclusion

To explore the critical zone architecture within Johnston Draw, I collected four seismic refraction tomography lines throughout the catchment perpendicular to the direction of drainage. From the resulting Vp profiles the depth to fractured and unweathered bedrock were identified and show a dynamic critical zone structure throughout Johnston Draw. The average depth to the top of unweathered bedrock changes from 14m deep at the headwater to 31m at the outlet, the depth to the top of fractured bedrock follows a similar trend. This increase in weathering extent at lower elevations, is similar to what was observed in soil weathering along elevation gradients above the rain-snow transition by *Reibe et al.* (2004a), *Dahlgren et al.* (1997), and *Rasmussen et al.* (2010). These studies suggested that the lower soil temperatures at higher elevation affect the reaction kinetics. However linking soil weathering to deep critical zone weathering is a tenuous prospect, as both the methods to measure weathering and the factors that can affect weathering are different.

Higher in the draw the north facing slope is more deeply weathered than the south facing slope, however this asymmetry decreases down drainage leading to nearly equal weathering depths on both aspects at the headwaters. The largest difference in weathering depth between the two aspects occurs ¾ the way through the draw, where the greatest difference in snow-accumulation occurs. Above this point the drainage direction shifts from east to southeast, so the snow accumulation on the aspects likely becomes more equal. Soil moisture measurements on the north facing slopes of Johnston Draw, show that the soils are recharged by a single pulse in the late spring. While the south facing slopes with its intermittent snowpack experiences periodic soil recharge events throughout the winter and spring. Numerical modeling studies (see *Langston et al.*, 2011; *Langston et al.*, 2015) have shown the single pulse recharge characteristic of the north facing slope is more effective at propagating moisture into the deep critical zone, than the periodic recharge events seen on the south facing slopes.

During the winter the temperature of the soils north facing are within the temperature window in which frost cracking occurs. However the time the hillslopes spend within the frost cracking window suggests that the maximum difference in weathering depth between the aspects should occur at lower elevations, where the observed difference in between is insignificant. This doesn't mean that frost cracking doesn't play a role in the weathering of Johnston Draw. Preferential flow paths generated by the frost cracking process would only amplify the difference in infiltration caused by the snow accumulation pattern. It is also likely that differences in vegetation density also contribute to the difference in weathering depth between the aspects. Higher in the catchment the north facing slope is more densely vegetated and hosts an aspen colony which could contribute to both the chemical and physical weathering on the north facing slope.

It is observed that both elevation and aspect play a role in the weathering pattern observed within Johnston Draw. Elevation effects weathering depth throughout Johnston Draw, while the effects of aspect are greatest high in the catchment. Of course it is not that elevation and aspect themselves affect weathering depth. But the climactic parameters such as temperature, precipitation, and radiation that vary with them that effect weathering. Within Johnston Draw snow and its unique water storage characteristics has a strong role in the weathering differences between the north and south aspects; however the role of temperature cannot be ruled out.

CHAPTER THREE: MONITORING NATURAL SOIL MOISTURE INFILTRATION USING TIME-LAPSE 3D ELECTRICAL RESISTIVITY TOMOGRAPHY

Abstract

At the Reynolds Creek Critical Zone Observatory (RCCZO), long term monitoring of soil moisture using *in situ* moisture probes has shown that during the dry summer only the shallow soils(<30cm) respond to rainfall events, while the deeper soils are recharged during the wet winter. To investigate this process, I installed a 7x8m^2 electrical resistivity tomography (ERT) array at the Low Elevation Sagebrush (LES), a long term hydrologic instrument site. To capture the dry down and wet up of the soils as well as the soils response to rainfall events, I monitored the site bi-weekly during the spring, summer, and fall of 2015 and 2016. The time-lapse ERT array was placed adjacent to time-domain reflectometry (TDR) probes, so that the time-lapse data could be referenced to precise measurements of volumetric water content. The individual resistivity volumes from the time-lapse array show spatial heterogeneity in the resistivity structure. The resulting ERT inversions show a 3 layer soil structure consisting of a high resistivity top layer that is from deposition; a low resistivity weathered soil layer at intermediate depth; and high resistivity saprolite. The resistivity of the top layer responds readily to the seasons and precipitation while the deeper weathered soil layer does not. This agrees well with the changes in soil moisture with depth measured by the TDR probes, suggesting that the contact between the depositional and weathered soil layer

limits infiltration. However weathered soil layer contains vertical preferential flow paths, whose resistivity responds to large precipitation events and seasonal changes in soil moisture. This implies that the preferential flow paths are a conduit for soil moisture flow that is not captured by the TDR probes. From the combined interpretation of the ERT and TDR I conclude that soil structure is a control on soil moisture infiltration during both the summer dry months and the winter wet flux period. And that preferential flow paths provide a vertical connection between the deep and shallow soils not captured by the TDR probes.

Introduction

Measuring the distribution and behavior of soil moisture in the vadose zone is vital for understanding a variety of hydrologic processes in natural and agricultural settings. However within unsaturated environments soil moisture has proven to be both spatially and temporally heterogeneous, making its robust characterization difficult. Conventional *in situ* sensors and direct sampling can provide accurate measurements of soil moisture at a point. And remote sensing methods provide spatially continuous measurement on the scale of kilometers. While geophysical methods have been proven to provide precise soil moisture estimates at the 1m to 100m scale [*Robinson et al.*, 2008b]. Ground penetrating radar (GPR) and electrical methods have been shown to be particularly useful in this application, as they measure the dielectric permittivity and electrical conductivity of the ground, respectively [*Parsekian et al.*, 2015], and both of these parameters are sensitive to volumetric water content. Electrical methods such as electrical resistivity tomography (ERT) have the added advantage of being able to install permanent electrode arrays, making them ideal for non-invasive time-lapse applications.

Further the petro/pedo-physical relationship between electrical resistivity and volumetric water content has been thoroughly studied with numerous laboratory and field experiments [*Shah and Singh*, 2005].

The application of electrical methods to characterize changing soil moisture dates back to before the use of tomographic inversions. The first application of DC electrical methods to soil science was by *Kean et al.*, (1987), who used vertical electrical sounding to characterize soil moisture migration before and after rainfall events. *Daily et al.*, (1992) applied tomographic inversion methods to create a 2D perspective of unsaturated flow in the vadose zone. By applying tomographic inversions *Daily et al.*, (1992) opened the door for more broad scale characterization of soil moisture heterogeneity. Now with the relatively low cost of electrical resistivity controllers and sophisticated readily available tomographic inversion software, ERT is widely applied to vadose zone water infiltration. Modern ERT allows for broad scale measurements that capture the spatial heterogeneity not practical with point scale measurements, such as time-domain reflectometry (TDR) probes and more detailed measurements than are capable with remote sensing methods. Further the use of surface arrays allows for continuous observations without interfering with the natural flow patterns. An example within the RCCZO is *Niemeyer et al.* (2017) in which time-lapse 2D ERT was used to study the effects of ecotone transitions to soil moisture distribution over a 100m transect.

In ERT the petro/pedo-physical relationship between electrical resistivity and water usually takes the form of Archie’s Law [*Archie*, 1942] or a modified form of Archie’s Law. *Shah and Singh* (2005) give a comprehensive review the petro/pedo-physical models relevant to soils. Precise calibration of any petro/pedo-physical model entails direct sampling, which is often expensive and requires destructive testing. Further there is no guarantee that any given sample is representative of the study area or target lithology or pedology. However if the soil moisture with depth is measured with adjacent soil moisture, the seasonal variation in volumetric water content measured by the TDR probes, and electrical resistivity measured by the ERT, can be used to solve for the non-time varying parameters. Several studies [*Schwartz et al.*, 2008; *Fan et al.*, 2015] have used adjacent TDR probes and ERT to solve for non-time varying pedo-physical parameters.

Currently the application of ERT towards the vadose zone can be loosely broken into three categories, controlled infiltration experiments for technical development [*Kean et al.*, 1987; *Daily et al.*, 1992; *Al Hagrey et al.*, 1999; *Al Hagrey and Michaelsen*, 1999; *Dietrich et al.*, 2003; *Singha and Gorelick*, 2005; *Cassiani et al.*, 2006; *Deiana et al.*, 2007; *Monego et al.*, 2010; *Travelletti et al.*, 2012; *Zumr et al.*, 2012] and the observation of infiltration from crop irrigation[*Michot et al.*, 2003; *Srayeddin and Doussan*, 2009] and meteoric precipitation [*French and Binley*, 2004; *Amidu and Dunbar*, 2007; *Miller et al.*, 2008; *Schwartz et al.*, 2008; *Brunet et al.*, 2010; *Nijland et al.*, 2010; *Calamita et al.*, 2012; *Robinson et al.*, 2012; *Yamakawa et al.*, 2012b; *Brillante et al.*, 2014; *Fan et al.*, 2015; *Niemeyer et al.*, 2017]. The majority of these ERT experiments have been conducted in Europe, with only a handful in the US, and only one ERT experiment *Miller et al.*, (2008) has observed the seasonal variation in soil moisture in the western sagebrush steppe. However *Miller et al.* (2008) focused on the deeper vadose zone seasonal moisture dynamics, leaving the imaging of the shallow seasonal changes and response to natural precipitation events within the sagebrush steppe unexplored with ERT.

Within semi-arid and arid environments the hydrologic connectivity within the vadose zone has an effect on stream flow dynamics, groundwater recharge, and ecology [*Freer et al.*, 2002; *McNamara et al.*, 2005; *Hinckley et al.*, 2014]. Characteristic seasonal states of soil moisture connectivity, have been identified at a snow-dominated headwater catchment within the Dry Creek Experimental Watershed (DCEW) which is: a dry period characterized by low and stable soil moistures; a transitional wetting period in which the field capacity is met for the deeper soils and wetting progresses downward; a wet, low-flux period in which accumulated snow keeps soil moistures stable at around field capacity; a wet, high-flux period where the snow begins to melt and the soil moisture responds to precipitation; a transitional late-spring drying period after the snow melts in which soil moistures decrease from evapotranspiration [*McNamara et al.*, 2005]. However at the plot scale the heterogeneity of soils and the potential presence of preferential flow paths complicate the characteristics of these seasonal states.

Preferential flow paths provide an hydrologic pathway other than matrix flow that have been shown contribute to subsurface flow [*Tromp-van Meerveld and McDonnell*, 2006a, 2006b]. Understanding their distribution and dimensions has large implications for hillslope hydrologic modeling[*Sidle et al.*, 2001]. However the majority of previous work on preferential flow paths have relied on excavation and dye tracer observations, which inherently disrupts the existing soil textures making long term observations in a natural environment difficult [*Leslie and Heinse*, 2013]. High-resolution ground penetrating radar and ERT has been used to image preferential flow paths [*Leslie and*

Heinse, 2013] and fractures [*Hansen and Lane*, 1995; *Robinson et al.*, 2013].However no study to date has used continuous geophysical measurements to monitor preferential flow path response to seasonal and precipitation changes.

In this study, permanent 3D ERT arrays (7mx8m) were installed at two sites within the Reynolds Creek Critical Zone Observatory (RCCZO) and used to conduct ERT surveys about every two weeks from May of 2015 to June of 2016. The results from lower elevation site Low Elevation Sagebrush (LES), is the primary focus of this thesis. The ERT results from the higher elevation site Mid Elevation Sagebrush (MES) are discussed in the Appendix. The inverted electrical resistivity grids were converted into volumetric water content using a modified form of Archie's Law. The non-time varying parameters of the modified Archie's Law were found by comparing the volumetric water content measured adjacent TDR probes and the resistivity measured by the ERT. In order to constrain the broader soil and critical zone structure a pair of crossing 2D seismic refraction tomography (SRT) and ERT surveys were conducted overtop the 3D ERT arrays. This project was designed to use ERT to image the change in soil moisture in response to seasonal change and precipitation events, so that the spatial temporal variation in hydrologic connectivity within the vadose zone could be examined. Previous studies have demonstrated the application of ERT for imaging seasonal monitoring of soil moisture changes [*French and Binley*, 2004; *Amidu and Dunbar*, 2007; *Miller et al.*, 2008; *Schwartz et al.*, 2008; *Brunet et al.*, 2010; *Nijland et al.*, 2010; *Calamita et al.*, 2012; *Robinson et al.*, 2012; *Yamakawa et al.*, 2012b; *Brillante et al.*, 2014; *Fan et al.*, 2015; *Niemeyer et al.*, 2017] and the imaging preferential flow path structure [*Leslie and Heinse*, 2013]. While there have been other studies that have applied electrical methods to understanding soil moisture distribution at the RCCZO [*Robinson et al.,* 2012; *Niemeyer et al.*, 2017], this is the first high temporal density ERT surveys at the RCCZO. Additionally this is the first 3D ERT study to monitor seasonal and precipitation driven changes in shallow soil moisture within the western sagebrush steppe.

Site-description

The RCCZO is a 240km^2 experimental watershed in southwest Idaho, as shown in figure 1. Geologically it is granite overlain by several sequences of Neogene volcanics with quaternary alluvium at the lower elevations. LES is at 1406min elevation, dominated by sagebrush and grasses; is primarily composed of basalt; and is on near neutral aspects. The site is near a northerly flowing ephemeral stream within a topographic basin. Rain is the dominant precipitation though it does occasionally snow it rarely persists for more than a few days.

Two profiles of Stevens hydraprobes (TDR probes) are installed at LES and the MES site, one within a cattle exclosure, given the suffix *n* for non-grazed, and one outside the exclosure, given the suffix *g* for grazed in (figure 13). They log volumetric water content every 15 minutes at depth 5cm, 15cm, 30cm, 60cm and 90cm. The volumetric water content measured by the probes within the exclosure for the LES and MES sites is shown in figures 14 and A1. Precipitation is also measured at both sites, outside of the map extents in figure 13, and is shown as the blue vertical lines in figures 14.

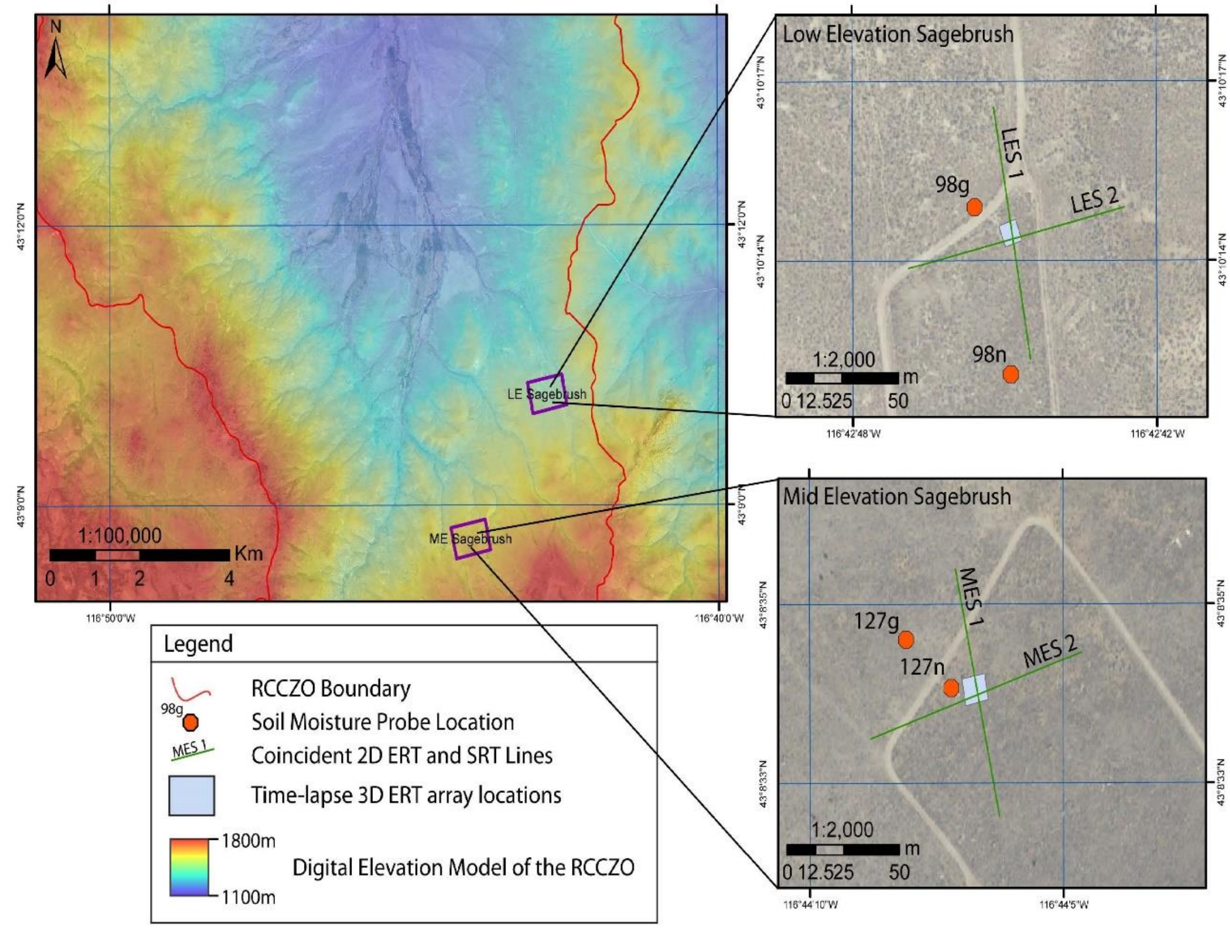

Figure 13: (a) is a digital elevation model overlaying satellite images of the southern portion of the Reynolds Creek Critical Zone Observatory, with the Reynolds Creek watershed boundary shown as a red line. The approximate extent of the LES and MES sites are shown as purple squares in (a). (b) and (c) are satellite image maps the LES and MES sites, with the 2D SRT and 2D ERT surveys lines, the extent of the 3D ERT surveys, and soil moisture probe profiles locations shown.

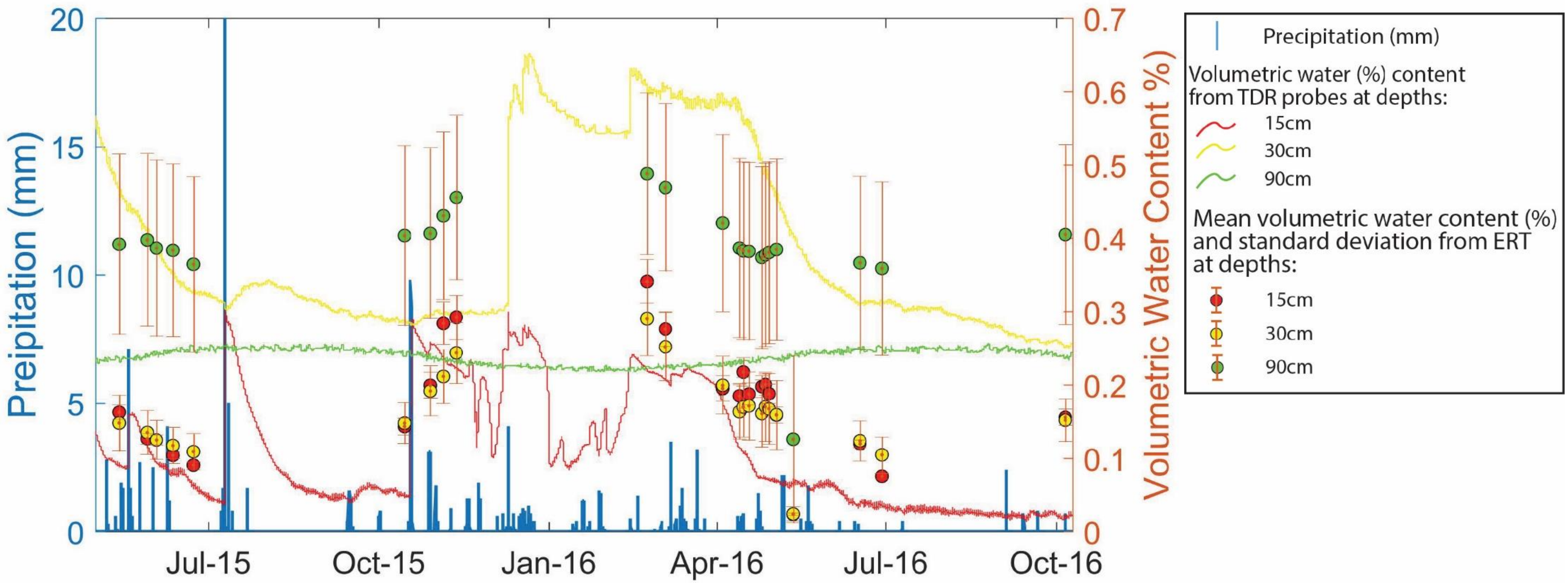

Figure 14: The colored lines are the volumetric water content as measured by the TDR probes, and the dots with errorbars are the mean and standard deviations of the conductivity of the resistivity grids at the same depths as the TDR probes, for the LES sites. The precipitation is also shown on both figures as blue vertical lines. Despite receiving similar amounts of precipitation, at the LES the volumetric water content at 90 cm remains constant.

At the RCCZO I identify four characteristic soil moisture states: low stable soil moisture occasionally broken by rainstorms that infiltrate 15cm; a late-fall or early-winter wetting period, in which the field capacity of the soils is met and matrix flow propagates to the deeper soils; a wet high-flux winter early-spring, characterized by high matrix soil moistures and rapid soil moisture response to precipitation; a spring drying where precipitation decreases and evapotranspiration draws down soil moisture to their summer dry values. There is little snow at both sites, and the soils rarely freeze, so there is no winter low flux period as was identified at the DCEW by *McNamara et al.*, (2005).

Methods

In order to image the changes in electrical resistivity caused by the changes in soil water content I installed permanent ERT arrays. The permanent 3D ERT arrays consist of 72 electrodes arranged in a uniform rectangular 8x9 grid; the electrodes are buried ~6cm deep and spaced 1m from each other, resulting in a 7x8m array. Each electrode is wired to a central connection box placed in the center of the array. The surveys were conducted using an Iris Syscal Pro Switch resistivity meter. The electrodes are composed of stainless steel wool connected to the wire via stainless steel nuts and bolt. To capture the seasonal changes in resistivity the surveys were conducted once every two weeks during the spring of 2015 and the fall of 2015, and weekly during the spring of 2016.

The apparent resistivities were inverted using an iteratively reweighted least squares inversion with the software package E4D [*Johnson et al.*, 2010]. The inversions were performed using a time-lapse approach; the temporal smoothing constraints were calculated using equation 1:

1 $$X = \left|(m_t - v_{ref}) - (m_n - v_{refn})\right|$$

Where m_t and m_n are the log of the conductivities of the target element and its spatial neighbor; and v_{ref} and v_{refn} are the log of conductivity of the target element and its spatial neighbor in a reference grid. The value X is then used to calculate the elements of the weighting function using:

$$W = {}^1\!/_2\left(1 - erf\left((X + mn)/\sqrt{2sd^2}\right)\right) \tag{2}$$

Where *erf* refers to the Gauss error function, *mn* is the center of the error function, and *sd* the standard deviation. The effective width equation 2 is *mn+2sd*, ergo if *X* is within *mn±2sd* a weighting is applied. This weighting schema acts to smooth the difference between the reference and target grid and thus forcing a consistent resistivity structure. As can be deduced, the quality of the time-lapse inversion result is dependent on the quality of the reference grid used to build the weighting matrix *W*. I assume that the changes in resistivity will be a function of difference in soil moisture. Thus by using a static inversion result for the reference grid taken when soil moisture is at its minimum, the changes in resistivity will all be negative and can be attributed to changes in soil moisture. While a reference grid taken at a high moisture state could have also been used, the sensitivity at depth is greater when the soil moisture is lower. The June 23rd, 2016 survey was chosen to be the reference solution as it was during a low soil moisture period at the static inversion converged to a high degree of confidence. The time-lapse inversions were iterated until the objective function reduced by less than 0.00001 between iterations. The mesh used for inversion 12mx12mx5m, well beyond the extent of the array and depth of investigation. The area of confidence is an 8mx8mx1.5m grid. The inversion results are interpolated to a uniform 0.05m grid spacing for plotting.

Weighting for the static inversion was used to smooth the spatial resistivity structure using the following equation:

3 $$X = |m_t - m_n|$$

where the value X is again used to calculate W in equation 2. In order to ensure that the resulting resistivity structures were persistent and not an anomaly within the reference grid static inversions were performed on the surveys gathered on February 23rd, 2016 and June 23rd, 2016. The static inversions were iterated until the mean residual was less than ±0.05Ωm, this generally took several thousand iterations.

Since soil temperatures at the LES site vary from -2C° in the winter to 30C° in the summer, a temperature correction was performed to normalize the resistivities to a single temperature. If the resistivities were not corrected for then comparing the resistivity grids across seasons would be skewed, as resistivity increases with temperature. The soil temperatures were corrected using the method outlined by *Keller and Frishchknecht*, (1966), whom proposed the resistivities can be adjusted to a temperature using:

4 $$\rho_{25} = \rho_m\left[1 + 0.02\left(T_m - T_{ref}\right)\right]$$

Where ρ_{25} is the corrected restively, ρ_m is the measured resistivity, T_m is the temperature during the measurement and T_{25} is the reference temperature (25C° in this study). Soil temperature is measured at depths of 5cm, 10cm, 20cm, 30cm, 40cm, 50cm, 60cm, 90cm, 120cm, and 180cm at the site, though outside of the map in figure 13. A piecewise cubic hermite interpolating polynomial was fitted to the measured temperatures at 5cm spacing, and it was assumed that the ground temperature is 11.1C° at 10m depth year round. Thus a 1D T_m was generated with the same vertical spacing as the resistivity tomograms.

Electrical resistivity grids can say a lot qualitatively about changes in soil moisture. However to make quantitative comparisons of the changes in volumetric water content the resistivity grids need to be converted into volumetric water content. In order to convert from electrical resistivity to soil moisture a petro/pedo-physical conversion was performed on the inverted temperature corrected resistivity grids. I used a modified form of Archie's Law proposed by *Shah and Singh* (2005) to convert from electrical resistivity to volumetric water content. Their study focused on soils and the effects of clay on the pedo-physics of soils, since both our study sites contain clayey soils their pedo-physical model, equation 5, is applicable and well tested.

5 $$\rho = {}^{1}/_{c}\, \rho_w \theta^{-m}$$

Equation 5 is a simplified form of the Archie's equation [*Archie*, 1942] where ρ_w is the conductivity of the pore water, θ is the volumetric water content, *m* is a fitting parameter dependent on the tortuosity and *c* a fitting parameter related to the soil matrix conductivity [*Shah and Singh*, 2005]. I simplify equation 5 further by assuming ρ_w is constant for each site and thus can be combined with c to creating a new parameter a:

6 $$\rho = a\theta^{-m}$$

The parameters *a* and *m* are here referred to as Archie's parameters. In order to find the Archie's parameters for each site the mean resistivity from the temperature correct inverted resistivity grids were compared to the volumetric water contents at the same depths. This comparison was done for the 3D ERT surveys from the spring of 2016. A gradient search was performed to find the Archie's parameters that provided the lowest RMSE between the resistivity calculated from equation 6 using the TDR probe measured volumetric water content and the mean resistivities from the ERT. Both resistivity and volumetric water content are time varying parameters while the Archie's parameters are time invariant, so by comparing a wide range of corresponding water content and resistivity a set of Archie's parameters that describe the relationship between volumetric water content and resistivity can be derived. The surveys for the spring of 2016, February, 23rd 2016 to June, 29th 2016, were used because of the high apparent resistivity data quality and the range of soil moistures captured.

The static inversion results (figures 15) show three distinct resistivity regimes, a high resistivity top layer and vertical tube structures, a low resistivity middle layer and high resistivity deeper layer. When a single set of Archie's parameters was fit to the whole resistivity grid the resulting soil moisture grid had unrealistic volumetric water content. So two sets of parameters were derived, one describing the pedo-physics of the high resistivity zone and one describing the low resistivity zones. At the LES site figure 15 shows that the high resistivity top layer extends to ~50cm of depth and that this layer responds readily to seasonal changes (see figure 16). The TDR probes at depths 5 cm, 15 cm, and 30 cm also respond to precipitation (figure 16) so it is assumed that the TDR probes at those depths occupy the high resistivity top layer and the TDR probes at 60 cm and 90 cm are within the low resistivity middle layer. Thus a set of Archie's parameters that fit the volumetric water content and resistivites for depths 5cm, 15cm, and 30cm is derived and a separate set of Archie's parameters that describe the relationship at depths 60cm and 90cm is also derived. The Archie's parameters used for the pedo-physical transform are shown in table 4.

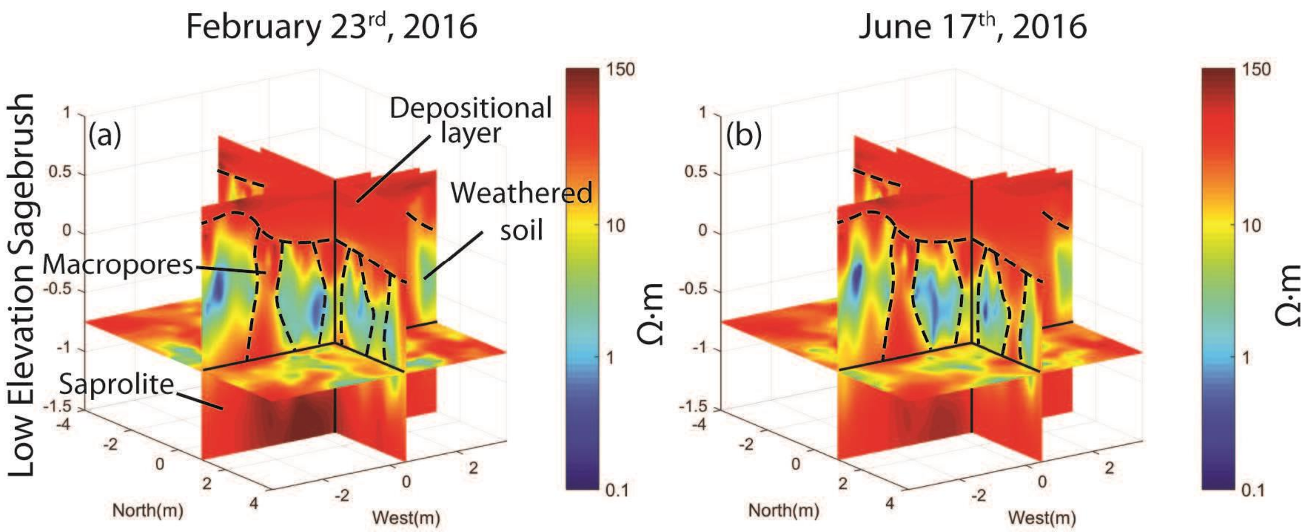

Figure 15: **The resistivity grids from the static inversion of the February, 23rd, 2016 (a) and June, 17th, 2016 (b) surveys for the LES site. The colorbar ramps at a log scale but the values indicated on the colorbar are the true resistivity values. The dark dotted lines are the contact between the various soil structures and in (a) soil structures are labeled with our interpretation. While the soil moisture states are very different between the two surveys the resistivity structure remains largely the same.**

Table 4: **Archie's patameters used in the pedo-physial conversion from resistivity to volumetric water content. Two sets of parameters were used for each site, one set for the high resistivity regions and one for the low resistivity regions.**

.

	LES High Res.	LES Low Res.	MES High Res.	MES Low Res.
m	0.7	1.1	1.25	25
a	9	0.6	1.6	0.005

Shah and Singh (2005) reported on the pedo-physical parameters from a variety of studies that tested a wide range of soil types, in addition they themselves tested silty soil, black cotton soil, white clay, and marine clay soil samples for a range of pedo-physical parameters. The c parameters of the soils they measured were 4.08, 15.85, 3.19, and 8.2, respectively, with corresponding ρ_w of 7.04Ωm, 8.93Ωm, 12.05Ωm, and 0.163Ωm. I combine the c and ρ_w parameters into a parameter a, thus the samples tested by Shah and Singh (2005) the a parameter would have a range of 1.72Ωm, 0.56Ωm, 3.77Ωm, and

0.020Ωm. Of all the soil samples tested and taken from other studies in Shah and Singh (2005), the *a* parameter has a range of 0.02Ωm to 16.67Ωm. The range of *c* values measured and gathered by Shah and Singh is 0.74 to 3.92.

In order to understand the broader resistivity structure a pair of 2D ERT surveys were conducted overtop the 3D ERT arrays parallel to the edge of the 3D arrays, see figure 13 for 2D and 3D survey extents. The surveys were conducted on October 6th, 2016. For the 2D ERT surveys a 72 electrode array with 2m electrode spacing was used and the surveys were conducted using an Iris Syscal Pro switch. On the same day as the 2D surveys the 3D arrays were also used to perform a 3D survey. The measured apparent resistivity's were inverted with a smoothness-constrained Gauss-Newton least-squares inversion [*Sasaki*, 1992] using the software package Res2Dinv. The inversions were conducted over 10 iterations, which was enough for the RMSE between iterations to change by less than 1%.

In addition to the 2D ERT I also gathered 2D seismic refraction surveys (SRT) to provide additional constraint on the broader CZ structure. By employing both ERT and SRT the CZ structure can be more robustly interpreted. 2D SRT surveys were conducted at roughly the same extent and orientation as the 2D ERT surveys (figure 13). The SRT surveys were conducted on the same day as the 2D ERT. The SRT surveys consisted of 96 10Hz geophones spaced 1.5m apart with 9 stacked shots performed every 6m using an 8lb sledgehammer and aluminum plate. The first arrivals were inverted with an wavepath eikonal traveltime tomography inversion (*Schuster and Quintus-Bosz*, 1993), using the Rayfract software package. The inversion was allowed to iterate 150. While there have been studies that have correlated weathering states of granite to seismic velocity [*Olona* *et al.*, 2010; *Holbrook et al.*, 2014], this correlation has not been done for the basaltic weathering process. However the knowledge that decreasing p-wave velocity correlates to increasing weathering[*Parsekian et al.*, 2015] is used to inform our interpretations of the 2D resistivity structure.

Results

For clarity only the inversion results from the LES site will be discussed, the results for the MES site are discussed in the Appendix. The static inversions all converged to a mean residual less than ±0.05Ωm, while the time lapse inversions converged to a mean residual less than 0.1Ωm. The higher level of convergence in the static inversion is due to the lack of temporal constraint, which allows for the resistivity structure to vary and fit the measured apparent resistivities more closely. However the time-lapse inversion is preferred for hydrologic analysis, as the temporal constraint insures smooth temporal changes better reflecting seasonal changes in soil moisture. The results from the static inversions are shown in figure 15, and as can be seen while the resistivity values are different, the soil structures are largely the same which suggests that there is an inherent resistivity structure to the soils. All of the 2D ERT surveys inverted to a mean residual of less than 0.5Ωm, and the 2D seismic refraction converged to solutions with RMS less than 2.00ms.

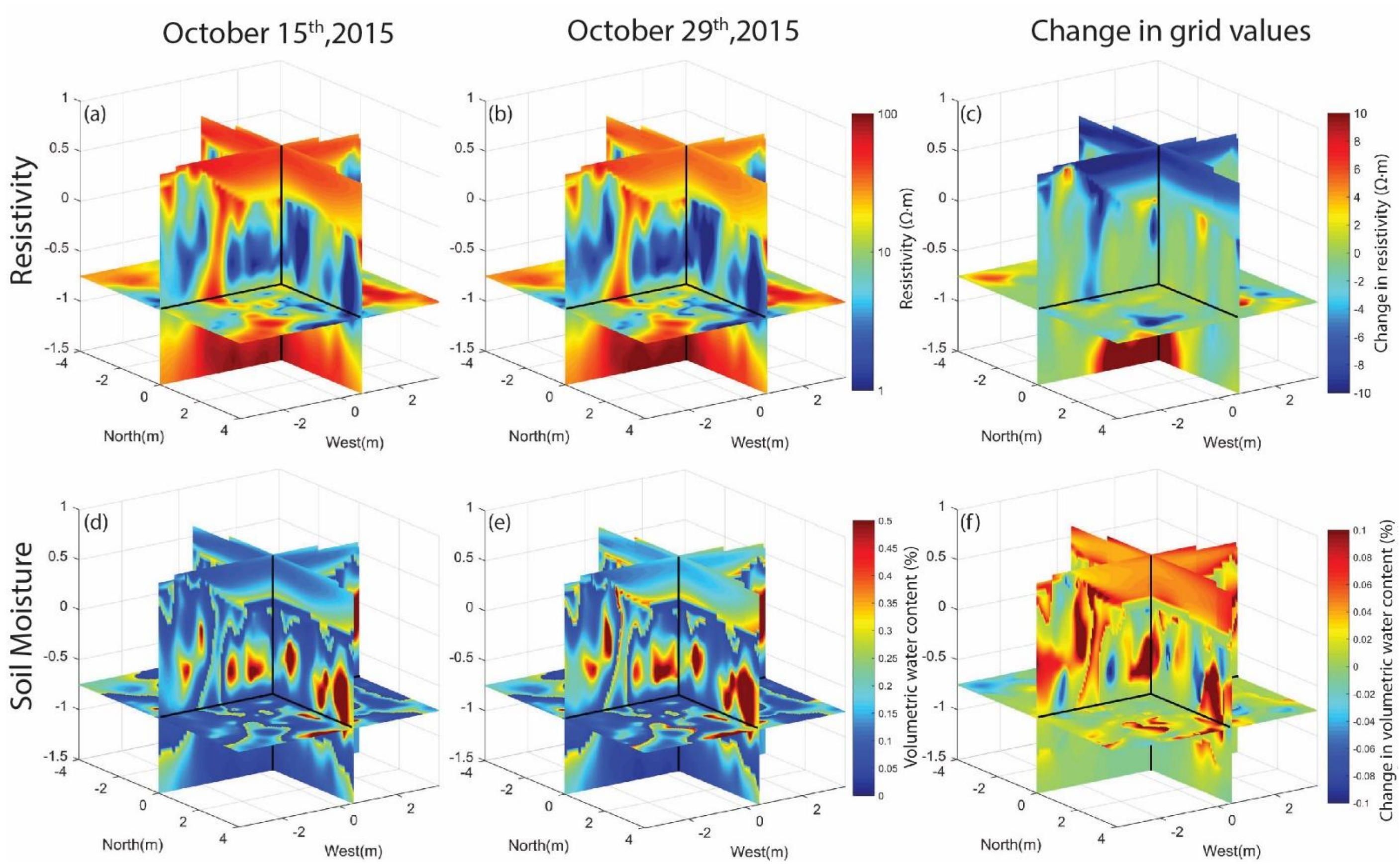

Figure 16: The response to the October 18th, 2015 rainfall event which precipitated 10 mm rain at the LES site. The resistivities and volumetric water contents were measured before the rainfall on October 15th (a, d) and after the rainfall on October 29th (b, e). The change in resistivity and volumetric water contents between the two surveys is shown in paned (c, f). The changes in electrical resistivity and volumetric water content are focused to the depositional layer and macropores. There are anomalous volumetric water content values in the soil

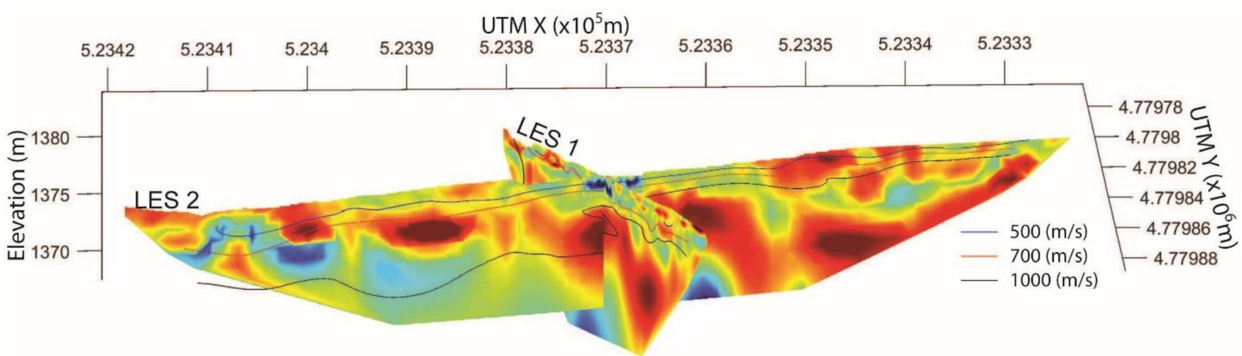

moisture grids suggesting that the pedo-physical conversion failed.

Figure 17: Fence plot looking north of the 2D resistivity surveys with the seismic velocity contours from the SRT surveys overlain of the LES site surveys. The portion of the 2D resistivity profiles that intersect the area of investigation of the 3D surveys is replaced with the resistivites from the 3D resistivity grids. The changes in seismic velocity and electrical resistivity are largely coincident.

The 2D resistivity profiles of the LES site (figure 17) show a general pattern of a moderately resistive 2m top layer and a high resistivity middle layer. This is interpreted as a weathered clayey soil layer transitioning to a less weathered more resistive saprolite layer. The resistivity and seismic velocity contours are generally in good agreement, with several anomalies being coincident in both. The north and west portions of the profiles show a decrease in both resistivity and seismic velocity, notably the sharp increase in the depth of the 1000m/s velocity contour. Since the weathering process always reduces the P-wave velocity of the parent material [*Parsekian et al.*, 2015] this indicates that the north and west portions of the profile are more weathered. There is also a high resistivity object near the surface at about easting 523350m that coincides with a warping of the velocity contours. The 700m/s velocity contour coincides with a transition from moderate resistivity to high resistivity in most of the profile, which is interpreted as the contact between weathered soil and saprolite. While there hasn't been as much research relating basalt weathering degree to seismic velocity, as there is for granite, *Von Voigtlander* (2016) found that the basalt derived soils at dry sites on the Kohala Peninsula of Hawaii were no faster than 1km/s. This supports the interpretation that the 700 m/s velocity contour is the transition from soils to saprolite.

In figure 17 where the 2D resistivity profiles cross the 3D resistivity arrays the resistivity information from the 3D resistivity grids was used, this can be seen as the small lower resistivity rectangle in figure 17. As can be seen in figure 17 the zone of investigation of 3D array is within the weathered soil layer with the bottom of the zone being near the contact between the weathered soil and saprolite layers. The 3D resistivity grids generally have lower resistivities than the 2D profiles, as the electrodes used in the permanent 3D arrays have much lower contact resistance than the electrodes used in the 2D arrays.

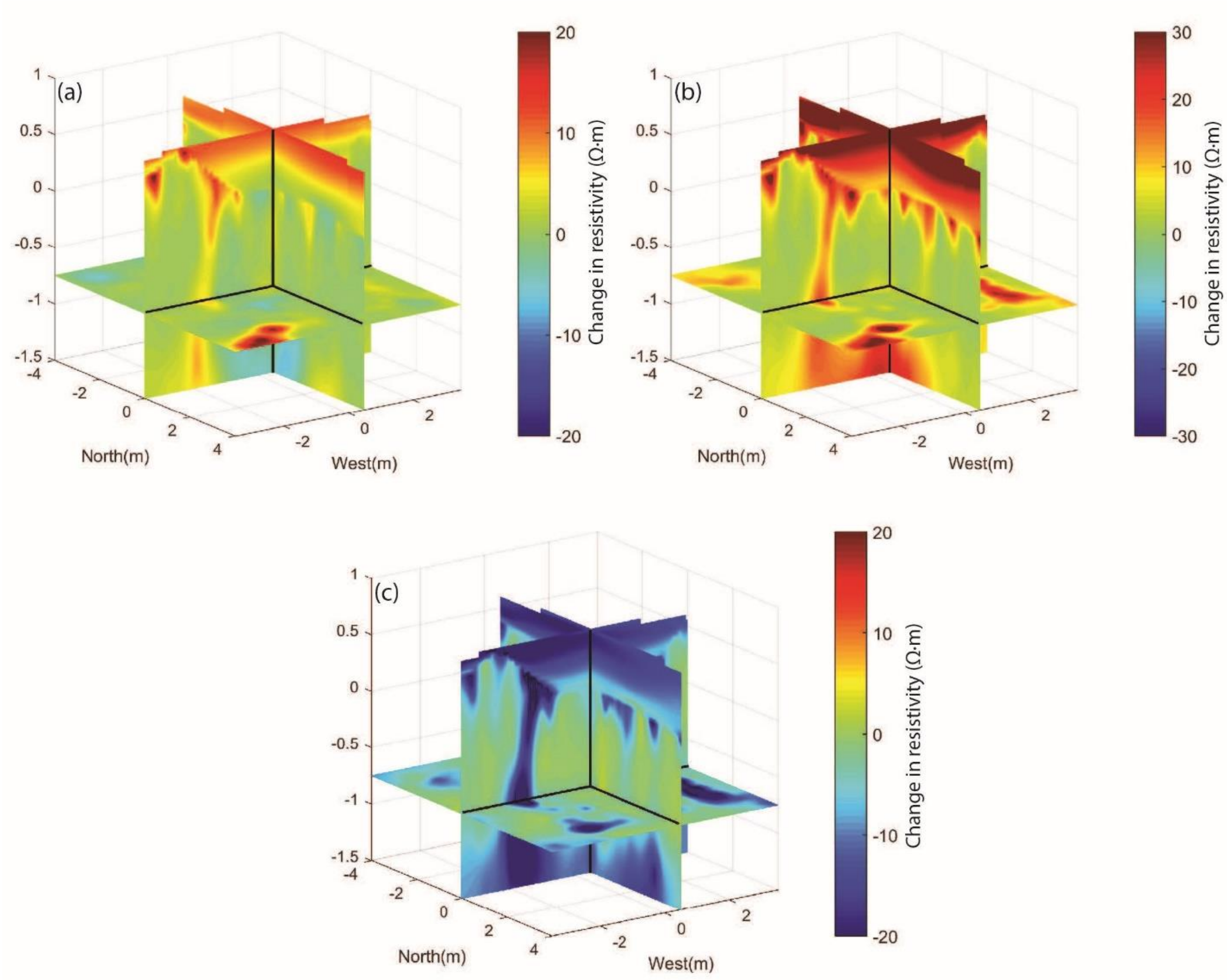

Figure 18: The change in resistivity for the springs of 2015 (a,) and 2016 (b). The change for the spring of 2015 is the difference in the grids from May 29th, 2015 to June 12th, 2015 and the change for the spring of 2016 is the difference between the grids gathered on February, 23rd, 2016 and June 29th, 2016. The change in the resistivity (a, b) for the fall 2015 (c). The grids are the difference in the reistivity grids taken on October 15th, 2015 and February 23rd, 2016. The seasonal changes in electrical resistivity are focused to the depositional and macropore layers suggesting that soil structure effects moisture distribution.

The resistivity structure within the 3D ERT array is characterized by a <50cm thick high resistivity top layer, underlain by a low resistivity ~1.5m thick middle layer, followed by a high resistivity horizon at about 2m (figure 15). Because of this site proximity to a stream and its position in a topographic low, the top layer is thought to be from a depositional process and is either loess or alluvial material. In this paper the top high resistivity layer will be referred to simply as the depositional layer. The middle low resistivity layer is likely weathered clayey soils of the basaltic parent material, here referred to as the weathered soil layer. The bottom high resistivity layer is interpreted as the saprolite identified in the broad resistivity structure (figure 17), as the transition from low to high resistivity occurs at roughly the same depth in both profiles. The high resistivity vertical pipe structures in the weathered soil layer persist throughout all the surveys no matter what inversion weighting strategy was applied, they can be seen in both the low resistivity winter (figures 15a) and the high resistivity summer, (figure 15b). Because the pipe structures persist through the seasons and as can be seen in figure 18b changing in resistivity in response to precipitation they are interpreted as being preferential flow paths.

During period of high soil moisture the ERT's sensitivity with depth decreases, due to the lower resistivity reducing the depth of current flow. This reduces the number of the individual dipole-dipole measurements that measure the deeper portions of the profile (>1.0m). The end result is a lower degree of confidence in the deeper resistivities during high soil moisture periods. However regardless of the time of year the static inversions resolve the transition to weathered soil and saprolite at the same depths. This suggests that while our sensitivity likely decrease at depth during wet periods, we still sample this portion of the profile well enough to resolve the soil lithology.

Preferential flow paths can be attributed to a variety of biological processes such as bioturbidation, root channeling, and pedological processes like clay swelling and soil freezing causing fractures to form in the soil [*Jarvis*, 2007]. Because the measured soil temperature at both sites is rarely below freezing, the preferential flow paths are unlikely to be caused by the freeze thaw cycle. There is no evidence of extensive bioturbation, further it does not seem likely that squirrel burrows have meter long vertical shafts. Fracture networks from clay swelling do occur in highly clayey soils, like those observed at the LES site, however there is no reference in literature to suggest that these networks would form in vertical tube shape structures. I believe the most likely explanation is that the preferential flow paths are the remnants of columnar joints, which have sustained as a flow path through the weathering process. However without excavation, the origin of the preferential flow paths and how they formed cannot be determined.

Figure 14 shows the volumetric water content measured by the TDR probes at depths 15cm, 30cm, and 90cm as colored lines, the mean volumetric water content of the soil moisture grids at the same depths as the TDR probes as colored circles and precipitation as blue vertical lines. The LES site has two sets of TDR profiles with one within the cattle exclosure, 98n, and one outside the exclosure, 98g. Both TDR profiles show a similar seasonal soil moisture pattern, in which only the TDR probes 30cm and above measure any significant seasonal change in water content. The lack of change in volumetric water content at 90cm could be attributed to equipment failure. However as the TDR profiles within and outside the exclosure show little change in water content at 90cm, indicating that the equipment is functioning and there is indeed minimal changes in volumetric water content below 30cm. As the ERT array is within the exclosure the profile 98n was used in analysis and is shown in figure 14. The limited infiltration at the LES is in contrast to TDR profiles at other sites like MES, which despite having similar precipitation amounts shows seasonal precipitation changes down to 90cm (figure A1). This suggests that there is a barrier to vertical soil moisture flow impeding infiltration at the LES site.

The Archie's parameters found using the gradient search are mostly within the range of parameters presented by *Shah and Singh* (2005). The range values for parameters *a* and *c* of samples shown in *Shah and Singh* (2005) is 0.02 Ωm to 16.67 Ωm and 0.74 to 3.92.

The ERT derived soil moisture follows the same trend as the TDR probes, though generally the ERT underestimates the volumetric water content (figure 14). However at the LES site the ERT indicates soil moisture change at depths 60cm and 90cm, while TDR probes show no change. This is due to the preferential flow path structures responding to seasonal and precipitation changes (see figure 16c), which could easily be missed by the TDR probes. The soil moisture grids (figure 16(d, e)) produce areas of unrealistic volumetric water contents in the low resistivity zone. This could be for a variety of reasons, such as the assumption that ρ_w doesn't vary seasonally, the gradient search used to find the Archie's parameters falls into a local minima, or that the pedo-physical model used isn't appropriate for these soils. Despite the unreliable results of the pedo-physical conversion valuable insights into soil moisture connectivity and distribution can be made from the resistivity grids.

Discussion

on October 18th, 2015, when the soils were dry and thought to be hydraulically disconnected a rainstorm precipitated 10mm at the LES site. 3D ERT surveys were gathered before and after the rainstorm on October 15th and October 29th, the results are shown in figure 15. Between those dates the TDR probes show an increase in volumetric water content of about 20% at 5cm, 15% at 15cm, 5% at 30cm, with little change in water content at depths 60cm and 90cm. This is characteristic of a large rainstorm during the dry summer low flux period, in which meteoric water doesn't infiltrate into the deeper soils. The change in resistivity (figure 16c) follows a similar pattern: the highest change in resistivity is near the surface and decreases with depth extending to the bottom of the depositional layer at ~50cm of depth. The preferential flow path structures can also be seen decreasing in resistivity to a depth of ~1.25m. However the TDR probes only observed significant changes in the volumetric water content in the upper 30 cm. Indicating that the preferential flow paths are providing a conduit for fluid flow during the summer low flux period that is not measured by the TDR probes. This is subsurface flow that is being completely missed by the existing *in situ* instruments.

The seasonal changes in resistivity during the springs of 2015 and 2016 and the fall of 2015 are shown in figure 18. The spring 2015 change in resistivity is the difference in the resistivity grids from May 29thand June 23rd, the spring 2016 is the difference in the grids from February 23rd, 2016 and June 29th, 2016, and the fall 2015 difference in the grids between the October 15th, 2015 and October 29th, 2015 surveys. In both the spring (figure 18(a,b)) and fall (figure 16c) transitions, the changes in resistivity are focused to the depositional, preferential flow path, and saprolite structures and the changes in volumetric water content to the upper 30cm. The lack of resistivity change in the weathered soil layer indicates that the weathered soil layer is staying at a relatively constant volumetric water content. This constant volumetric water content suggests that the contact between the depositional layer and weathered soil layer is a barrier to moisture flow. This contact is likely why the TDR probes show different soil moisture characteristics between the LES and MES sites (figure 14 and A1). If soil structure was not the limiter in infiltration, then the seasonal changes in resistivity would decrease smoothly with depth reflecting a smooth soil moistures distribution. However a sharp transition between the zones that do vary in resistivity and the zones that do not is observed.

As in the resistivities response to precipitation, the change in resistivity in the preferential flow paths show that water is flowing through them. In addition this water flow is being missed by the TDR probes. The corresponding decrease in resistivity of the preferential flow path and saprolite during the fall wetting (figure 18c) indicates that some amount of water is flowing through the preferential flow paths and wetting the saprolite. However I cannot exclude the possibility that a mechanism other than preferential flow paths that is outside our survey area is the primary source of water traveling to the saprolite. During the spring 2016 drying period, (figure 18b), the saprolite can also be seen to be decreasing in resisitivity suggesting that they are being subject to evapotranspiration or the moisture is infiltrating even deeper. This isn’t observed during the spring 2015 drying, but only the end of that season was surveyed with the 3D ERT. The seasonal changes in saprolite resistivity suggest that the deeper saprolites are not disconnected fom the surface and shallow soils. If one were to only rely on the TDR probes for interpretation the logical conclusion is that there is little to no infiltration to the deeper subsurface. But TDR probes are not buried deep enough to measure the water content change in the saprolites, and as previously stated these probes are missing the flow through the preferential flow paths. The ERT shows that the preferential flow paths are providing a flow pathway in which some moisture is flowing through causing the saprolite to change in resistivity.

The implications of the seasonal and precipitation driven changes in the resistivity grids are that: (1) soil structure is a control on hydraulic connectivity, (2) that preferential flow paths are a hydraulic connection between the deep and shallow CZ that can be missed by *in situ* instruments, and (3) preferential flow paths flow can be initiated during the summer dry low flux period causing deep recharge. The observation that soil structure effects hydraulic connectivity and that preferential flow paths play a role in soil hydrology is likely a site dependent phenomenon, as the same limits to infiltration are not observed at the MES site (figure A1). However more universally, these observations do strongly suggest that spatially sparse *in situ* measurements can miss much of the hydrogeologic processes that occur even at the meter scale.

Conclusion

As discussed earlier, McNamara et al. (2005) proposed five periods to describe the seasonal soil moisture characteristics. This work was done at a snow dominated headwater catchment within the Dry Creek Experimental Watershed (DCEW) which is just north of Boise, Idaho and 45 miles northeast of the RCCZO. The seasonal periods at the LES site follows a similar pattern, however unlike the DCEW the LES sites do not accumulate snow so there isn’t a wet, low-flux period. The pattern is a dry summer and early-fall, characterized by low stable soil moistures occasionally broken by rainstorms that infiltrate 15cm; a late-fall or early-winter wetting period, in which the field capacity of the soils is met and matrix flow propagates to the deeper soils; a wet high-flux winter early-spring, characterized by high matrix soil moistures and rapid soil moisture response to precipitation; a spring drying where precipitation decreases and evapotranspiration draws down soil moisture to their summer dry values.

All but the late-fall/early-winter wetting period were captured in detail with the electrical resistivity surveys. However surveys were gathered before and after the fall transition, so the transition can be inferred (figure 18c). The surveys on October 15th and 29th of 2015 are representative of a dry summer soil state, and its response to a substantial rainstorm (figure 16). The surveys gathered in the springs of 2015 and 2016 show the structure of resistivity change through the spring drying (figures 18(a, b)).

The seasonal and precipitation driven changes in resistivity are focused to the soil structures identified in figure 15, which suggests that soil structure is a control on the hydrologic connectivity of soil moisture. The TDR probes at 5cm, 15cm and 30cm measure changes in the volumetric water content. While the probes at 60cm and 90cm measure little change, this coincides with the resistivity change of a deposition layer (figure 16c) that extends to a depth of about 50cm. In the weathered soil layer the resistivity does not change significantly outside of the vertical preferential flow path structure. This suggests that the bottom of the depositional layer is a barrier to flow, which is why the TDR probes at 60cm and 90cm don't measure much soil moisture change.

The resistivity of preferential flow paths can be seen to respond to precipitation and seasonal changes, suggesting that they provide a conduit of soil moisture flow. During the October 18th, 2015 precipitation (figure 16c) event the preferential flow paths can be seen to decrease in resistivity at depths up to 1.25m. While the TDR probes at the site (figure 14) do not show a change in precipitation at 60cm and 90cm. This indicates that the preferential flow paths are allowing moisture to infiltrate into the deeper soils, while bypassing the TDR probes. The preferential flow paths can also be seen to change in resistivity during the fall wetting and spring drying. During the spring drying of 2015 and 2016, and the fall wetting, the TDR measurements show minimal change in volumetric water content, while the preferential flow paths in the resistivity grids show significant changes in resistivity (figure 18). This indicates that the volumetric water content in the preferential flow paths is changing in response to seasonal soil moisture changes. Suggesting that preferential flow paths may allow for vertical soil moisture infiltration into the deeper soil profile during the fall wetting period, which is not captured by the TDR measurements.

The time-lapse resistivity surveys show that at the LES site soil structure and soil weathering play a role in the flow and distribution of soil moisture, at both the seasonal and precipitation event time-scales. The contact between the depositional layer and the underlying weathered soil is a barrier for moisture infiltration, and the preferential flow paths are seen to respond to precipitation and seasonal changes. This demonstrates that various soil structures play a key role in vadose zone hydrology that is difficult to characterize without spatially and temporally dense datasets.

CHAPTER FOUR: SUMMARY AND CONCLUSION

The critical zone is where the biological world interacts with the geological world via the weathering process. The weathering processes that governs CZ architecture is a complex interplay of climate[*Millot et al.*, 2002; *Riebe et al.*, 2004b], altitude [*Riebe et al.*, 2004c], hydrology[*Dunne*, 1998; *Hinckley et al.*, 2014; *Langston et al.*, 2015], tectonics [*Molnar et al.*, 2007; *St. Clair et al.*, 2015], and biological processes[*Moulton and Berner*, 1998; *Amundson et al.*, 2007; *Gabet and Mudd*, 2010; *Roering et al.*, 2010]. Over a sufficiently large extent the microclimatic factors vary, making characterizing the weathering architecture at a catchment scale difficult. To further complicate the CZ environment is the unsaturated zone just below the surface. The non-linearity of hydraulic conductivity at unsaturated volumetric water contents make modeling water flow difficult. In both weathering architecture and soil moisture infiltration, a limitation in understanding these processes is the spatial density of measurements. Traditional methods of drilling core or digging soil pits to characterize weathering is difficult to apply at a catchment scale. While soil moisture probes provide temporally dense precise measurements of volumetric water content, they do so at only one point. In this thesis I applied geophysical methods in a pair of studies that investigate CZ architecture and soil moisture distribution. The first study is a seismic survey of a catchment that spans a sizable elevation gradient and whose aspects host different microclimates. Thus the effects of aspect and elevation on weathering extent can be elucidated. The second is a time-lapse 3D resistivity survey to image soil moisture dynamics in order to understand the controls on soil moisture infiltration.

Within snow-dominated catchments it has been observed that the north facing slopes are more deeply weathered than the south facing slopes, and as elevation increases weathering rate decreases. There are two theories that explain this observation. First, that the cooler temperatures on the north facing slopes leads to greater damage from frost cracking to the soils and saprolites [*Anderson et al.*, 2013]. And second, is that the persistent snow pack on the north facing slope melts all at once in late spring and is more effective at propagating soil moisture into the deep CZ than the intermittent snow pack on southern aspects which experience multiple melting events throughout the winter and spring [*Langston et al.*, 2015]. It has also been observed that weathering extent of soils varies with elevation, and has been hypothesized that above the rain snow transition decreasing mean yearly soil temperatures with increasing elevation reduces the weathering rate [*Riebe et al.*, 2004c; *Rasmussen et al.*, 2010]. Within Johnston Draw the mean depth to unweathered bedrock (table 3) increases down drainage, but the difference in weathering depth between the aspects increases up drainage. The maximum difference in weathering between the north and south facing slopes occurred where the maximum difference in snow accumulation occurred (see figures 4 and 11). This suggests a correlation between weathering extent and snow accumulation. All of the paired instrument sites show a single concentrated infiltration pulse on north facing slopes and episodic infiltration on the south facing slopes. The work done by *Langston et al., (2015)* would imply that this soil moisture pattern would lead to water being infiltrated into the CZ on the north facing slopes than the south facing slopes at the same elevation. The soil temperatures at 5cm show that all the north facing hillslopes spend time within the frost cracking window, [-8°C to -3°C]. However if it is assumed that time spent within the frost cracking window (figure 5) leads to more extensive weathering, then the difference in weathering depth between the aspects would increase down drainage. This is not consistent with what was observed in the seismic velocity profiles. If the frost cracking window is expanded to [-8°C to 0°C], then the time spent within the frost cracking for the hillslopes becomes reflective of the hillslopes weathering pattern. But even with the expanded frost cracking window, the low elevation seismic line shows minimal weathering depth asymmetry, while the soil temperature profiles show this low elevation line should be experiencing frost cracking damage. Thus as the temperature profiles clearly show frost cracking does occur on the northerly aspect of Johnston Draw, I propose that frost cracking and infiltration from persistent snow work in conjunction to increase the weathering rate on north facing slopes. Frost cracking increases porosity and creates preferential flow paths on north facing slopes, which makes the average hydraulic conductivity of the north facing hillslopes greater than the south facing slopes. This asymmetry in hydraulic conductivity increases the difference deep CZ water content already caused by the difference in snowpack persistence between the aspects.

The Johnston Draw study contributes to our greater understanding of the deep CZ by testing hypotheses and by contributing a uniquely spatially broad dataset of weathering depth information. I concluded that the frost cracking theory proposed by *Anderson et al. (2013)* alone cannot explain the aspect correlated weathering differences within Johnston Draw. Observations and modeling conducted by *Langston et al. (2015)* suggest that persistent snow accumulation increases the rate of weathering and our observations that snow accumulation amounts correspond to areas of deeper weathering supports this theory. These conclusions could only be reached because of our unique dataset of both seismic velocity and paired hydrologic instruments. The paired hydrologic instrument data and the seismic data is itself a valuable contribution, as it will be a dataset in which future theories can be tested against.

The inverted 3D resistivity grids show that the soils have persistent resistivity structure. Which is interpreted as a depositional top-layer overlaying a low resistivity weathered soil layer under which is high resistivity saprolite (figure 15). Within the low resistivity weathered soil layer there are vertical structures I believe are preferential flow paths. As their resistivities respond to precipitation and seasonal change, suggesting they are a conduit for soil moisture flow. The resistivity grids were converted to a volumetric water content grid using equation 6, with parameters a and m were found by the gradient search method to fit volumetric water content measured via the TDR probes and the mean resistivity at the same depth from the inverted resistivity grids. As can be seen in figure 14 the volumetric water content grids follow the trend of the TDR derived water content measurements, but the grids themselves (figure 16(d, e)) produce unrealistic water content measurements for the low resistivity weathered soil layer. This suggests that the pedophysical conversion is not robust. Despite the inconsistencies of the volumetric water content grids, valuable inferences into soil moisture distribution and connectivity can be made from the resistivity grids and the changes in the resistivity grids from seasonal and precipitation derived soil moisture changes. The soil structures highlighted in figure 15 is where the majority of seasonal resistivity change occurs (figure 18). The TDR volumetric water content measurements for the LES site (figure 14) show that changes in the water content are not measured at the probes at 60cm and 90cm, this agrees with the changes in the resistivity grids caused by precipitation and seasonal changes (figure 16c and 18). The change in the resistivity grids at the LES site show that there is little change in resistivity in the weathered soil layer and the TDR probes at those depths also show minimal change. This suggests that the contact between the depositional layer and weathered soil layer is a barrier to soil moisture flow. Preferential flow path structures can be seen to respond to both the seasonal and precipitation driven changes in soil moisture. This is particularly interesting at the LES site where the TDR probes show little change in soil moisture at depths deeper than 30cm and the preferential flow paths resistivity is changing at depths down to 1.25m. This observation implies that the preferential flow paths at this site are providing a flow pathway not captured by the TDR probes. The observations from this site show that soil moisture flow and distribution is partially controlled by soil layering, and that TDR profiles can fail to characterize the soil moisture distribution at the plot scale.

While long term ERT surveys are nothing new, this is the first temporally and spatially dense ERT survey to be conducted in the western US and in the sagebrush step. By gathering such dense data I was able to make unique observations about the soil moisture infiltration patterns at these sites. The observation of water content change within a preferential flow path is the first that I know of. While preferential flow paths are likely not as prevalent in other sites as they were at LES, by demonstrating their role in the hydrology at LES I have shown the need for spatially and temporally dense datasets to make process based conclusions in regard to hydrologic systems.

While these projects don't directly overlap, the implication of the Core Site study is that fine scale preferential flow paths play difficult to characterize role moisture infiltration that is easily missed by soil moisture probe profiles. It is unlikely that preferential flow paths like the ones observed at the LES site exist within Johnston Draw. But frost cracking could be creating smaller conduits on the north facing slope and that the flow from these conduits is being missed by the TDR profiles within Johnston Draw. We of course don't know conclusively that preferentially flow paths are present on the north facing slopes of Johnston Draw, but the implication of the LES study is we wouldn't know if they existed from the TDR profiles alone.

Both of these studies have shown that hydro-geophysical imaging can provide spatially broad details of near-surface properties, which can be used to make inferences into hydrologic processes, such as bedrock weathering and soil moisture distribution. The seismic survey of Johnston Draw revealed that bedrock weathering is controlled by interplay of elevation, temperature, and precipitation phase, which results in a weathering pattern that varies both between aspects and elevation. The time-lapse ERT surveys showed that soil moisture distribution is influenced by soil structures and that TDR probes can under sample the soil-moisture distribution.

REFERENCES

Al Hagrey, S. A., and J. Michaelsen (1999), Resistivity and percolation study of preferential flow in vadose zone at Bokhorst, Germany, *Geophysics*, *64*(3), 746–753.

Al Hagrey, S. A., T. Schubert-Klempnauer, D. Wachsmuth, J. Michaelsen, and R. Meissner (1999), Preferential flow: first results of a full-scale flow model, *Geophys. J. Int.*, *138*(3), 643–654.

Amidu, S. A., and J. A. Dunbar (2007), Geoelectric Studies of Seasonal Wetting and Drying of a Texas Vertisol, *Vadose Zone J.*, *6*(3), 511, doi:10.2136/vzj2007.0005.

Amundson, R., D. D. Richter, G. S. Humphreys, E. G. Jobbágy, and J. Gaillardet (2007), Coupling between biota and earth materials in the critical zone, *Elements*, *3*(5), 327–332.

Anderson, R. S., S. P. Anderson, and G. E. Tucker (2013), Rock damage and regolith transport by frost: an example of climate modulation of the geomorphology of the critical zone: ROCK DAMAGE AND REGOLITH TRANSPORT BY FROST, *Earth Surf. Process. Landf.*, *38*(3), 299–316, doi:10.1002/esp.3330.

Anderson, S. P., E.-L. Hinckley, P. Kelly, and A. Langston (2014), Variation in Critical Zone Processes and Architecture across Slope Aspects, *Procedia Earth Planet. Sci.*, *10*, 28–33, doi:10.1016/j.proeps.2014.08.006.

Anderson, S.P., von Blackenburg, Friedhelm., and White, Arthur F. (2007), Physical and Chemical Controls on the Critical Zone, *Elements, 3*, 315–319.

Archie, G. E. (1942), The electrical resistivity log as an aid in determining some reservoir characteristics, *Pet. Trans. AIME*, *146*, 54–62.

Balachandran, K. (1975), Determination of Weathering Thickness by a Seismic P-S Delay Technique, *GEOPHYSICS*, *6*, 1073–1075.

Befus, K. M., A. F. Sheehan, M. Leopold, S. P. Anderson, and R. S. Anderson (2011), Seismic Constraints on Critical Zone Architecture, Boulder Creek Watershed, Front Range, Colorado, *Vadose Zone J.*, *10*(3), 915, doi:10.2136/vzj2010.0108.

Brantley, S. L., M. B. Goldhaber, and K. V. Ragnarsdottir (2007), Crossing disciplines and scales to understand the critical zone, *Elements*, *3*(5), 307–314.

Brillante, L., B. Bois, O. Mathieu, V. Bichet, D. Michot, and J. Lévêque (2014), Monitoring soil volume wetness in heterogeneous soils by electrical resistivity. A field-based pedotransfer function, *J. Hydrol.*, *516*, 56–66, doi:10.1016/j.jhydrol.2014.01.052.

Brunet, P., R. Clément, and C. Bouvier (2010), Monitoring soil water content and deficit using Electrical Resistivity Tomography (ERT) – A case study in the Cevennes area, France, *J. Hydrol.*, *380*(1–2), 146–153, doi:10.1016/j.jhydrol.2009.10.032.

Buss, H. L., S. L. Brantley, F. N. Scatena, E. A. Bazilievskaya, A. Blum, M. Schulz, R. Jiménez, A. F. White, G. Rother, and D. Cole (2013), Probing the deep critical zone beneath the Luquillo Experimental Forest, Puerto Rico: LUQUILLO DEEP CRITICAL ZONE, *Earth Surf. Process. Landf.*, *38*(10), 1170–1186, doi:10.1002/esp.3409.

Calamita, G., L. Brocca, A. Perrone, S. Piscitelli, V. Lapenna, F. Melone, and T. Moramarco (2012), Electrical resistivity and TDR methods for soil moisture estimation in central Italy test-sites, *J. Hydrol.*, *454–455*, 101–112, doi:10.1016/j.jhydrol.2012.06.001.

Cassiani, G., R. Deiana, A. Villa, V. Bruno, A. Bagliani, M. Miorali, and N. Fusi (2006), A water injection experiment in the vadose zone: The use and value of non invasive cross-hole data for model calibration, in *Proc. Int. Conf. on Computational Methods in Water Resour., 16th, Copenhagen, Denmark*, pp. 19–22.

Dahlgren, R.A., Boettinger, J.L., Huntington, G.L., and Amundson, R.G. (1997), Dahlgren_Soil_Development_Along_Elevation_Gradient.pdf, *Geoderma*, *78*, 207–236.

Daily, William, Ramirez, Abelardo, LaBrecque, Douglas, and Nitao, John (1992), Electrical Resistivity Tomography of Vadose Zone Water Movement, *Water Resour. Res.*, *28*(5), 1429–1442.

Deiana, R., G. Cassiani, A. Kemna, A. Villa, V. Bruno, and A. Bagliani (2007), An experiment of non-invasive characterization of the vadose zone via water injection and cross-hole time-lapse geophysical monitoring, *Surf. Geophys.*, *5*(3), 183–194.

Dietrich, W. E., D. G. Bellugi, L. S. Sklar, J. D. Stock, A. M. Heimsath, and J. J. Roering (2003), Geomorphic transport laws for predicting landscape form and dynamics, in *Geophysical Monograph Series*, vol. 135, edited by P. R. Wilcock and R. M. Iverson, pp. 103–132, American Geophysical Union, Washington, D. C.

Dunne, T. (1998), CRITICAL DATA REQUIREMENTS FOR PREDICTION OF EROSION AND SEDIMENTATION IN MOUNTAIN DRAINAGE BASINS, *J. Am. Water Resour. Assoc.*, *34*(4), 795–808, doi:10.1111/j.1752-1688.1998.tb01516.x.

Egli, M., A. Mirabella, G. Sartori, R. Zanelli, and S. Bischof (2006), Effect of north and south exposure on weathering rates and clay mineral formation in Alpine soils, *CATENA*, *67*(3), 155–174, doi:10.1016/j.catena.2006.02.010.

Ekren, E. B., D. H. McIntyre, E. H. Bennet, and H. E. Malde (1981), Geologic map of Owyhee County, Idaho, west of longitude 116° W, Map I-1256,

Fan, J., A. Scheuermann, A. Guyot, T. Baumgartl, and D. A. Lockington (2015), Quantifying spatiotemporal dynamics of root-zone soil water in a mixed forest on subtropical coastal sand dune using surface ERT and spatial TDR, *J. Hydrol.*, *523*, 475–488, doi:10.1016/j.jhydrol.2015.01.064.

Freer, J., J. J. McDonnell, K. J. Beven, N. E. Peters, D. A. Burns, R. P. Hooper, B. Aulenbach, and C. Kendall (2002), The role of bedrock topography on subsurface storm flow: THE ROLE OF BEDROCK TOPOGRAPHY ON SUBSURFACE STORM FLOW, *Water Resour. Res.*, *38*(12), 5-1-5–16, doi:10.1029/2001WR000872.

French, H., and A. Binley (2004), Snowmelt infiltration: monitoring temporal and spatial variability using time-lapse electrical resistivity, *J. Hydrol.*, *297*(1–4), 174–186, doi:10.1016/j.jhydrol.2004.04.005.

Gabet, E. J., and S. M. Mudd (2010), Bedrock erosion by root fracture and tree throw: A coupled biogeomorphic model to explore the humped soil production function and the persistence of hillslope soils, *J. Geophys. Res.*, *115*(F4), doi:10.1029/2009JF001526.

Hales, T. C., and J. J. Roering (2007), Climatic controls on frost cracking and implications for the evolution of bedrock landscapes, *J. Geophys. Res.*, *112*(F2), doi:10.1029/2006JF000616.

Hansen, B. P., and J. W. Lane (1995), *Use of surface and borehole geophysical surveys to determine fracture orientation and other site characteristics in crystalline bedrock terrain, Millville and Uxbridge, Massachusetts*, US Department of the Interior, US Geological Survey.

Hinckley, E.-L. S., B. A. Ebel, R. T. Barnes, R. S. Anderson, M. W. Williams, and S. P. Anderson (2014), Aspect control of water movement on hillslopes near the rain-snow transition of the Colorado Front Range: SNOWMELT AND HYDROLOGICAL FLOW PATHS ON OPPOSING HILLSLOPE ASPECTS, *Hydrol. Process.*, *28*(1), 74–85, doi:10.1002/hyp.9549.

Holbrook, W. S., C. S. Riebe, M. Elwaseif, J. L. Hayes, K. Basler-Reeder, D. L. Harry, A. Malazian, A. Dosseto, P. C. Hartsough, and J. W. Hopmans (2014), Geophysical constraints on deep weathering and water storage potential in the Southern Sierra Critical Zone Observatory: GEOPHYSICAL CONSTRAINTS ON WEATHERING IN THE SOUTHERN SIERRA CZO, *Earth Surf. Process. Landf.*, *39*(3), 366–380, doi:10.1002/esp.3502.

Hunckler, R. V., and R. J. Schaetzl (1997), Spodosol development as affected by geomorphic aspect, Baraga County, Michigan, *Soil Sci. Soc. Am. J.*, *61*(4), 1105–1115.

Jansen, Stefan (2010), Parameter investigation for subsurface tomography with refraction seismic data, Mastes Thesis, Niels Borh Institute, Universty of Copenhagen, November.

Jarvis, N. J. (2007), A review of non-equilibrium water flow and solute transport in soil macropores: principles, controlling factors and consequences for water quality, *Eur. J. Soil Sci.*, *58*(3), 523–546, doi:10.1111/j.1365-2389.2007.00915.x.

Jayawickreme, D. H., R. L. Van Dam, and D. W. Hyndman (2008), Subsurface imaging of vegetation, climate, and root-zone moisture interactions, *Geophys. Res. Lett.*, *35*(18), doi:10.1029/2008GL034690.

Jin, L., R. Ravella, B. Ketchum, P. R. Bierman, P. Heaney, T. White, and S. L. Brantley (2010), Mineral weathering and elemental transport during hillslope evolution at the Susquehanna/Shale Hills Critical Zone Observatory, *Geochim. Cosmochim. Acta*, *74*(13), 3669–3691, doi:10.1016/j.gca.2010.03.036.

Johnson, T. C., R. J. Versteeg, A. Ward, F. D. Day-Lewis, and A. Revil (2010), Improved hydrogeophysical characterization and monitoring through parallel modeling and inversion of time-domain resistivity andinduced-polarization data, *GEOPHYSICS*, *75*(4), WA27-WA41, doi:10.1190/1.3475513.

Jones, J. R., and N. V. Debyle (1985), *Morphology*, Aspen: Ecology and management in the western United States, USDA Forest Service.

Kean, W. F., M. J. Waller, and H. R. Layson (1987), Monitoring Moisture Migration in the Vadose Zone with Resistivity, *Groundwater*, *25*(5), 562–571.

Keller, G. V., and F. C. Frishchknecht (1966), *Electrical methods in geophysical prospecting*, Oxford: Pergamon press.

Langston, A. L., G. E. Tucker, R. S. Anderson, and S. P. Anderson (2011), Exploring links between vadose zone hydrology and chemical weathering in the Boulder Creek critical zone observatory, *Appl. Geochem.*, *26*, S70–S71, doi:10.1016/j.apgeochem.2011.03.033.

Langston, A. L., G. E. Tucker, R. S. Anderson, and S. P. Anderson (2015), Evidence for climatic and hillslope-aspect controls on vadose zone hydrology and implications for saprolite weathering: CLIMATIC CONTROL ON VADOSE ZONE MOISTURE, *Earth Surf. Process. Landf.*, *40*(9), 1254–1269, doi:10.1002/esp.3718.

Lebedeva, M. I., and S. L. Brantley (2013), Exploring geochemical controls on weathering and erosion of convex hillslopes: beyond the empirical regolith production function: HILLSLOPE EVOLUTION AND REGOLITH THICKNESS, *Earth Surf. Process. Landf.*, *38*(15), 1793–1807, doi:10.1002/esp.3424.

Leopold, M., J. Völkel, J. Huber, and D. Dethier (2013), Subsurface architecture of the Boulder Creek Critical Zone Observatory from electrical resistivity tomography: CRITICAL ZONE ARCHITECTURE AT BOULDER CREEK CRITICAL ZONE OBSERVATORY, *Earth Surf. Process. Landf.*, n/a-n/a, doi:10.1002/esp.3420.

Leslie, I. N., and R. Heinse (2013), Characterizing Soil–Pipe Networks with Pseudo-Three-Dimensional Resistivity Tomography on Forested Hillslopes with Restrictive Horizons, *Vadose Zone J.*, *12*(4), 0, doi:10.2136/vzj2012.0200.

Ma, L., F. Chabaux, N. West, E. Kirby, L. Jin, and S. Brantley (2013), Regolith production and transport in the Susquehanna Shale Hills Critical Zone Observatory, Part 1: Insights from U-series isotopes: HILLSLOPE ASPECT AND REGOLITH PRODUCTION, *J. Geophys. Res. Earth Surf.*, *118*(2), 722–740, doi:10.1002/jgrf.20037.

Maher, K. (2010), The dependence of chemical weathering rates on fluid residence time, *Earth Planet. Sci. Lett.*, *294*(1–2), 101–110, doi:10.1016/j.epsl.2010.03.010.

Marks, D., A. Winstral, and M. Seyfried (2002), Simulation of terrain and forest shelter effects on patterns of snow deposition, snowmelt and runoff over a semi-arid mountain catchment, *Hydrol. Process.*, *16*(18), 3605–3626, doi:10.1002/hyp.1237.

McIntyre, Davis H. (1972), Cenozoic Geology of the Reynolds Creek Experimental Watershed, Owyhee County, Idaho, *Ida. Buraeu Mines Geol.*, *Pamphlet 151*.

McNamara, J. P., D. Chandler, M. Seyfried, and S. Achet (2005), Soil moisture states, lateral flow, and streamflow generation in a semi-arid, snowmelt-driven catchment, *Hydrol. Process.*, *19*(20), 4023–4038, doi:10.1002/hyp.5869.

Michot, D., Y. Benderitter, A. Dorigny, B. Nicoullaud, D. King, and A. Tabbagh (2003), Spatial and temporal monitoring of soil water content with an irrigated corn crop cover using surface electrical resistivity tomography: SOIL WATER STUDY USING ELECTRICAL RESISTIVITY, *Water Resour. Res.*, *39*(5), n/a-n/a, doi:10.1029/2002WR001581.

Miller, C. R., P. S. Routh, T. R. Brosten, and J. P. McNamara (2008), Application of time-lapse ERT imaging to watershed characterization, *GEOPHYSICS*, *73*(3), G7–G17, doi:10.1190/1.2907156.

Millot, R., J. Gaillardet, B. Dupré, and C. J. Allègre (2002), The global control of silicate weathering rates and the coupling with physical erosion: new insights from rivers of the Canadian Shield, *Earth Planet. Sci. Lett.*, *196*(1), 83–98.

Molnar, P., R. S. Anderson, and S. P. Anderson (2007), Tectonics, fracturing of rock, and erosion, *J. Geophys. Res.*, *112*(F3), doi:10.1029/2005JF000433.

Monego, M., G. Cassiani, R. Deiana, M. Putti, G. Passadore, and L. Altissimo (2010), A tracer test in a shallow heterogeneous aquifer monitored via time-lapse surface electrical resistivity tomography, *GEOPHYSICS*, *75*(4), WA61-WA73, doi:10.1190/1.3474601.

Moulton, K. L., and R. A. Berner (1998), Quantification of the effect of plants on weathering: Studies in Iceland, *Geology*, *26*(10), 895–898.

Nielson, T., and J. Bradford (2015), Sensitivity of seismic refraction inversion to smooth and blocky velocity gradients, pp. 2313–2317, Society of Exploration Geophysicists.

Niemeyer, R. J., R. Heinse, T. E. Link, M. S. Seyfried, P. Z. Klos, C. J. Williams, and T. Nielson (2017), Spatiotemporal soil and saprolite moisture dynamics across a semi-arid woody plant gradient, *J. Hydrol.*, *544*, 21–35, doi:10.1016/j.jhydrol.2016.11.005.

Nijland, W., M. van der Meijde, E. A. Addink, and S. M. de Jong (2010), Detection of soil moisture and vegetation water abstraction in a Mediterranean natural area using electrical resistivity tomography, *CATENA*, *81*(3), 209–216, doi:10.1016/j.catena.2010.03.005.

Olona, J., J. A. Pulgar, G. Fernández-Viejo, C. López-Fernández, and J. M. González-Cortina (2010), Weathering variations in a granitic massif and related geotechnical properties through seismic and electrical resistivity methods, *Surf. Geophys.*, *8*(1750), doi:10.3997/1873-0604.2010043.

Parsekian, A. D., K. Singha, B. J. Minsley, W. S. Holbrook, and L. Slater (2015), Multiscale geophysical imaging of the critical zone: Geophysical Imaging of the Critical Zone, *Rev. Geophys.*, *53*(1), 1–26, doi:10.1002/2014RG000465.

Payne, S. J., R. McCaffrey, R. W. King, and S. A. Kattenhorn (2012), A new interpretation of deformation rates in the Snake River Plain and adjacent basin and range regions based on GPS measurements: Deformation rates in the Snake River Plain, *Geophys. J. Int.*, *189*(1), 101–122, doi:10.1111/j.1365-246X.2012.05370.x.

Poulos, M. J., J. L. Pierce, A. N. Flores, and S. G. Benner (2012), Hillslope asymmetry maps reveal widespread, multi-scale organization: MAPPING HILLSLOPE ASYMMETRY, *Geophys. Res. Lett.*, *39*(6), n/a-n/a, doi:10.1029/2012GL051283.

Rasmussen, C., R. A. Dahlgren, and R. J. Southard (2010), Basalt weathering and pedogenesis across an environmental gradient in the southern Cascade Range, California, USA, *Geoderma*, *154*(3–4), 473–485, doi:10.1016/j.geoderma.2009.05.019.

Rech, J. A., R. W. Reeves, and D. M. Hendricks (2001), The influence of slope aspect on soil weathering processes in the Springerville volcanic field, Arizona, *Catena*, *43*(1), 49–62.

Rempe, D. M., and W. E. Dietrich (2014), A bottom-up control on fresh-bedrock topography under landscapes, *Proc. Natl. Acad. Sci.*, *111*(18), 6576–6581, doi:10.1073/pnas.1404763111.

Riebe, C. S., J. W. Kirchner, and R. C. Finkel (2004a), Erosional and climatic effects on long-term chemical weathering rates in granitic landscapes spanning diverse climate regimes, *Earth Planet. Sci. Lett.*, *224*(3–4), 547–562, doi:10.1016/j.epsl.2004.05.019.

Riebe, C. S., J. W. Kirchner, and R. C. Finkel (2004b), Erosional and climatic effects on long-term chemical weathering rates in granitic landscapes spanning diverse climate regimes, *Earth Planet. Sci. Lett.*, *224*(3–4), 547–562, doi:10.1016/j.epsl.2004.05.019.

Riebe, C. S., J. W. Kirchner, and R. C. Finkel (2004c), Sharp decrease in long-term chemical weathering rates along an altitudinal transect, *Earth Planet. Sci. Lett.*, *218*(3–4), 421–434, doi:10.1016/S0012-821X(03)00673-3.

Riebe, C. S., W. J. Hahm, and S. L. Brantley (2016), Controls on deep critical zone architecture: a historical review and four testable hypotheses: Four Testable Hypotheses about the Deep Critical Zone, *Earth Surf. Process. Landf.*, doi:10.1002/esp.4052.

Robinson, D. A. et al. (2008a), Advancing process-based watershed hydrological research using near-surface geophysics: a vision for, and review of, electrical and magnetic geophysical methods, *Hydrol. Process.*, *22*(18), 3604–3635, doi:10.1002/hyp.6963.

Robinson, D. A., C. S. Campbell, J. W. Hopmans, B. K. Hornbuckle, S. B. Jones, R. Knight, F. Ogden, J. Selker, and O. Wendroth (2008b), Soil Moisture Measurement for Ecological and Hydrological Watershed-Scale Observatories: A Review, *Vadose Zone J.*, *7*(1), 358, doi:10.2136/vzj2007.0143.

Robinson, J., T. Johnson, and L. Slater (2013), Evaluation of known-boundary and resistivity constraints for improving cross-borehole DC electrical resistivity imaging of discrete fractures, *GEOPHYSICS*, *78*(3), D115–D127, doi:10.1190/geo2012-0333.1.

Robinson, J. L., L. D. Slater, and K. V. R. Schäfer (2012), Evidence for spatial variability in hydraulic redistribution within an oak–pine forest from resistivity imaging, *J. Hydrol.*, *430–431*, 69–79, doi:10.1016/j.jhydrol.2012.02.002.

Roering, J. J., J. Marshall, A. M. Booth, M. Mort, and Q. Jin (2010), Evidence for biotic controls on topography and soil production, *Earth Planet. Sci. Lett.*, *298*(1–2), 183–190, doi:10.1016/j.epsl.2010.07.040.

Sasaki, Y. (1992), Resolution of resistivity tomography inferred from numerical simulation, *Geophys. Prospect. Eur. Assoc. Explor. Geophys.*, *40*(4), 453.

Schuster, Gerard T., and Quintus-Bosz, Aksel (1993), Wavepath eikonal traveltime inversion: Theory, *GEOPHYSICS*, *58*(9), 1314–1323.

Schwartz, B. F., M. E. Schreiber, and T. Yan (2008), Quantifying field-scale soil moisture using electrical resistivity imaging, *J. Hydrol.*, *362*(3–4), 234–246, doi:10.1016/j.jhydrol.2008.08.027.

Seyfried, M. S., R. C. Harris, D. Marks, and B. Jacob (2000), A geographic database for watershed research, Reynolds Creek Experimental Watershed, Idaho, USA, *Tech Bull NWRC 2000*, *3*, 26.

Shah, P. H., and D. N. Singh (2005), Generalized Archie's Law for Estimation of Soil Electrical Conductivity, *J. ASTM Int.*, *2*(5), 13087, doi:10.1520/JAI13087.

Sidle, R. C., S. Noguchi, Y. Tsuboyama, and K. Laursen (2001), A conceptual model of preferential flow systems in forested hillslopes: evidence of self-organization, *Hydrol. Process.*, *15*(10), 1675–1692, doi:10.1002/hyp.233.

Singha, K., and S. M. Gorelick (2005), Saline tracer visualized with three-dimensional electrical resistivity tomography: Field-scale spatial moment analysis: SPATIAL MOMENT ANALYSIS OF ERT, *Water Resour. Res.*, *41*(5), n/a-n/a, doi:10.1029/2004WR003460.

Srayeddin, I., and C. Doussan (2009), Estimation of the spatial variability of root water uptake of maize and sorghum at the field scale by electrical resistivity tomography, *Plant Soil*, *319*(1–2), 185–207, doi:10.1007/s11104-008-9860-5.

St. Clair, J., S. Moon, W. S. Holbrook, J. T. Perron, C. S. Riebe, S. J. Martel, B. Carr, C. Harman, K. Singha, and D. d. Richter (2015), Geophysical imaging reveals topographic stress control of bedrock weathering, *Science*, *350*(6260), 534–538, doi:10.1126/science.aab2210.

Thomas, M. F. (1966), Some Geomorphological Implications of Deep Weathering Patterns in Crystalline Rocks in Nigeria, *Trans. Inst. Br. Geogr.*, (40), 173, doi:10.2307/621576.

Travelletti, J., P. Sailhac, J.-P. Malet, G. Grandjean, and J. Ponton (2012), Hydrological response of weathered clay-shale slopes: water infiltration monitoring with time-lapse electrical resistivity tomography, *Hydrol. Process.*, *26*(14), 2106–2119, doi:10.1002/hyp.7983.

Tromp-van Meerveld, H. J., and J. J. McDonnell (2006a), Threshold relations in subsurface stormflow: 1. A 147-storm analysis of the Panola hillslope: SUBSURFACE FLOW RELATIONS, 1, *Water Resour. Res.*, *42*(2), n/a-n/a, doi:10.1029/2004WR003778.

Tromp-van Meerveld, H. J., and J. J. McDonnell (2006b), Threshold relations in subsurface stormflow: 2. The fill and spill hypothesis: THRESHOLD FLOW RELATIONS, 2, *Water Resour. Res.*, *42*(2), n/a-n/a, doi:10.1029/2004WR003800.

Vignoli, G., G. Cassiani, M. Rossi, R. Deiana, J. Boaga, and P. Fabbri (2012), Geophysical characterization of a small pre-Alpine catchment, *J. Appl. Geophys.*, *80*, 32–42, doi:10.1016/j.jappgeo.2012.01.007.

Von Voigtlander, J. (2016), P-wave velocity of weathering profiles from a basalt climosequence: Implications for weathering on the mechanical properties of the critical zone,

Walder, J. S., and B. Hallet (1986), The Physical Basis of Frost Weathering: Toward a More Fundamental and Unified Perspective, *Arct. Alp. Res.*, *18*(1), 27, doi:10.2307/1551211.

Yamakawa, Y., K. ’ichirou Kosugi, N. Masaoka, J. Sumida, M. Tani, and T. Mizuyama (2012a), Combined geophysical methods for detecting soil thickness distribution on a weathered granitic hillslope, *Geomorphology*, *145–146*, 56–69, doi:10.1016/j.geomorph.2011.12.035.

Yamakawa, Y., K. ’ichirou Kosugi, S. ’ya Katsura, N. Masaoka, and T. Mizuyama (2012b), Spatial and Temporal Monitoring of Water Content in Weathered Granitic Bedrock Using Electrical Resistivity Imaging, *Vadose Zone J.*, *11*(1), 0, doi:10.2136/vzj2011.0029.

Zelt, C. A., Haines, S., Powers, M. H., Sheehan, J., Rohdewald, S., Link, C., Hayashi, K., Zhao, D., Zhao, H.-w, Burton, B.L., Peterson, U.K., Bonal, N.D., and Doll, W. E. (2013). Blind Test of Methods for Obtaining 2-D Near-Surface Seismic Velocity Models from First-Arrival Traveltimes. Journal of Environmental & Engineering Geophysics, 18(3), 183–194. https://doi.org/10.2113/JEEG18.3.183

Zumr, D., M. Snehota, and M. Cislerova (2012), Numerical Simulation of Tension Infiltration Experiment Monitored by 3D ERT.

APPENDIX A

Soil moisture monitoring at the Mid Elevation Sagebrush site

Site description

The Mid Elevation Sagebrush (MES) is located 3.6km southeast of the Low Elevation Sagebrush (LES) at an elevation of 1650m (figure 1). Like the LES site MES is on a near neutral aspect; is dominated by sagebrush and grasses; and consists of weathered basalt. Unlike the LES site, MES is on a ridge bounded by two westward draining ephemeral streams and has extensive animal burrows from ground squirrels.

Methods

The ERT array at the MES site is identical to the one at the LES site, except that the electrodes are made of woven stainless steel mesh with a wire diameter of 0.035”. The surveys were conducted at the MES site on the same day as they were at LES. However there were a handful of survey days in which the MES site was not visited due to poor road conditions. Equations 1 and 2 were also used to determine the weighting for the inversion for the data from the MES site, but with different values for *mn* and *sd*.

The same methodology for the pedo-physical conversion applied to LES was applied to MES. At LES the TDR probes at 5cm, 15cm, and 30cm were correlated to the high resistivity top layer, while at MES only the TDR probes at 5cm and 15cm were attributed to the high resistivity top layer. Thus a set of Archie’s parameters for depths 5cm and 15cm and depths 30cm, 60cm, and 90cm were derived, table 4.

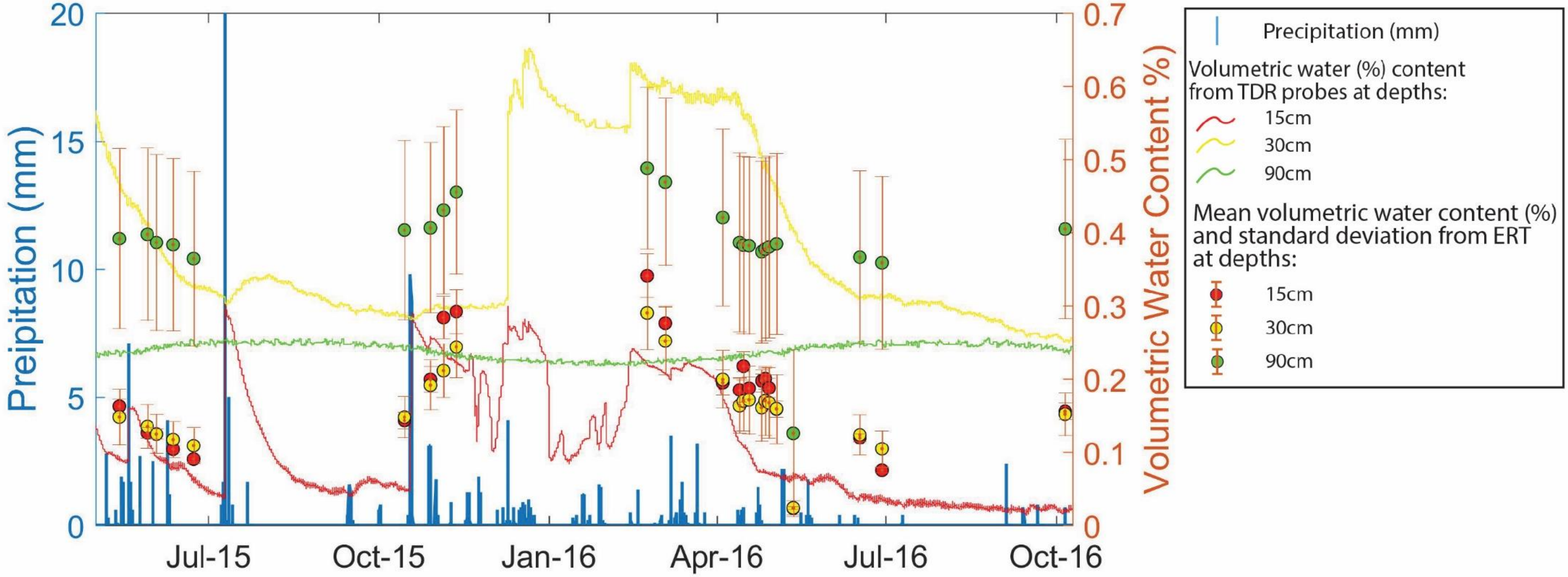

Figure A1: **The colored lines are the volumetric water content as measured by the TDR probes, and the dots with errorbars are the mean and standard deviations of the conductivity of the resistivity grids at the same depths as the TDR probes, for the MES sites. The precipitation is also shown on both _gures as orange vertical lines. Despite recieving similar amounts of precipitation, at the MES the volumetric water content at 90 cm remains constant.**

At MES the 2D ERT and SRT surveys were conducted on September 29th, 2016, with the same survey specification as the 2D surveys at the LES site. The 2D inversion were performed in the same manner at both sites and reached a similar level of convergence.

Results

The static inversion converged to ±0.05Ωm, suggesting a good fit to measured data. And the 2D ERT and SRT converged to about 0.5Ωm and 2.00ms, respectively, also a good fit to the data. The time-lapse 3D inversions for the surveys conducted at the MES site converged to a mean residual of around 5Ωm. This is much higher than the inversions from the LES surveys which converged to 0.1Ωm. This lower degree of convergence implies that the time-lapse inversion was overly temporally smoothed. However a variety of weight calculation parameters, *mn* and *std* for equation 2, were used and none converged to a high degree. The high error rate becomes an issue during the wet periods, where the mean resistivity for the survey measurements is as low as 30Ωm, which means the relative error for the inversion is ~17%. This makes confidently interpreting the inverted resistivity grids tenuous especially for the surveys gathered in the wet winter and spring months.

The broad 2D resistivity profiles reveal a complex resistivity structure at the MES site (figure A2). Across the MES 1 and MES 2 lines there is an intermittent high resistivity top layer that is less than 2m thick. This is likely not the same thin top layer seen in the 3D profiles as it is much thicker and does not occur at the array location. Below this intermittent top layer, and at the surface where the layer does not exist, there is a low resistivity layer that extends between 2 and 3m below the surface. At around 2 and 3m depth circular high resistivity anomalies occur across both profiles, separating these high resistivity anomalies are zones of very low resistivity. The intermittent top layer could be the result of Aeolian deposition or bioturbation and the low resistivity layer below that the highly weathered clayey soil the loess was deposited on. The high resistivity circular anomalies are likely core-stones that have remained relatively unweathered. The 3D and 2D profiles agree at the MES site in much the same way they agreed at the LES site, the 3D profiles have a thin top layer that could not be resolved with the 2D survey and both profiles resolve a transition to a higher resistivity saprolite at about 2m. The seismic velocity contours roughly bound the transitions between high and low resistivity however between 1600m and 1605m a low velocity zone on line MES 2 (figure A2) complicates interpretation. The low velocity zone does roughly bound the high resistivity zones identified as core stones, however it is uncommon in a uniform weathering environment to have a low velocity layer. As this is a basalt environment and the low velocity zone is roughly horizontal, it could be a separate layer of basalt that is more heavily weathered.

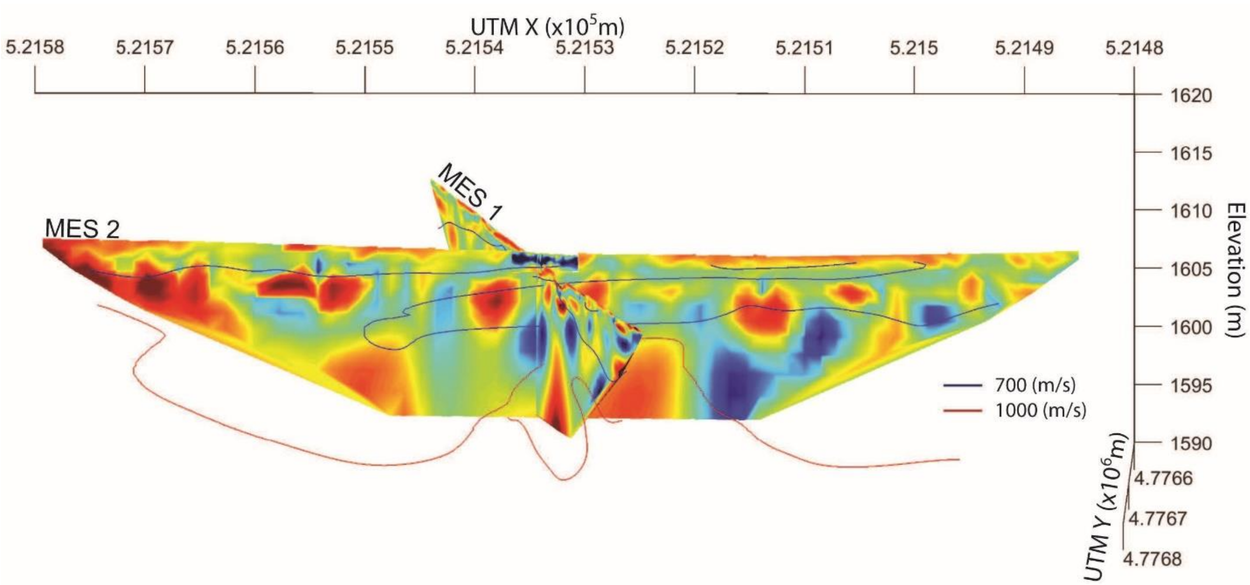

Figure A2: Fence plot looking north of the 2D resistivity surveys with the seismic velocity contours from the SRT surveys overlain of the MES site surveys. The portion of the 2D resistivity pro_les that intersect the area of investigation of the 3D surveys is replaced with the resistivites from the 3D resistivity grids.

The 3D resistivity structure shows a high resistivity top layer, followed by a low resistivity middle layer, and finally a high resistivity bottom layer. This is similar to what was observed at the LES site, figure 15, however the top high resistivity layer is less than 25cm thick, see figure A3. The soils at the MES site feature quite a few animal burrows. This bioturbation would increase the soils bulk porosity; therefor the high resistivity top layer is likely a layer of bioturbated soil. Thus at the MES site the soil structure is interpreted to be: <15cm of bioturbated layer, under which is ~2m thick highly weathered clayey basaltic soil, underlain by less weathered more resistive basalt saprolite. As with LES site there are persistent vertical macropores present, whose resistivities respond to rainfall and seasonal changes in soil moisture (figure A4).

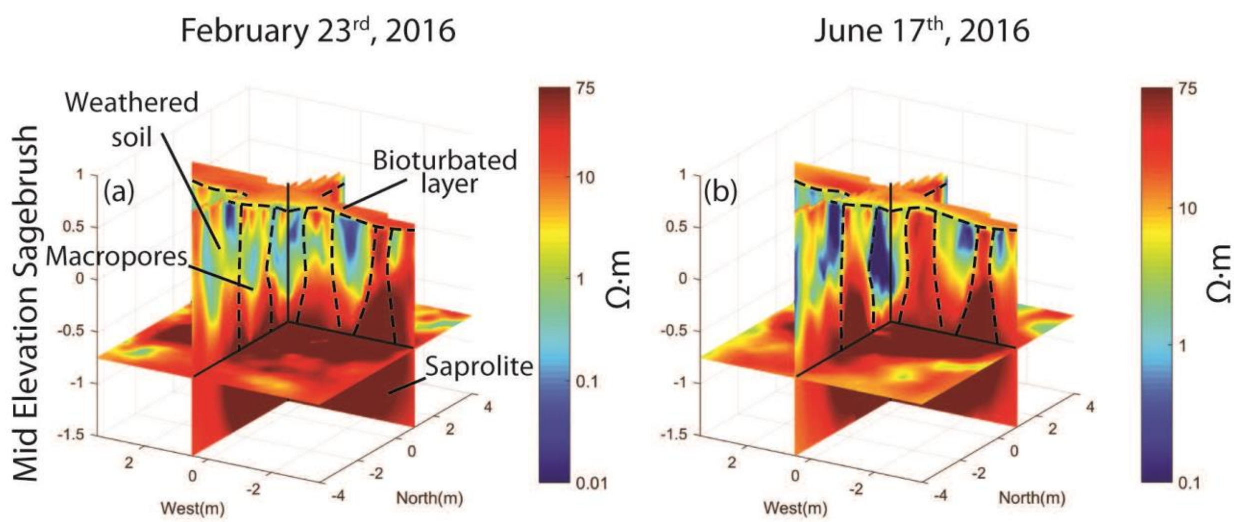

Figure A3: The resistivity grids from the static inversion of the February, 23rd, 2016 (a) and June, 17th, 2016 (b) surveys for the MES site. The colorbar ramps at a log scale but the values indicated on the colorbar are the true resistivity values. The dark dotted lines are the contact between the various soil structures and in (a) soil structures are labeled with our interpretation. While the soil moisture states are very di_erent between the two surveys the resistivity structure remains largely the same.

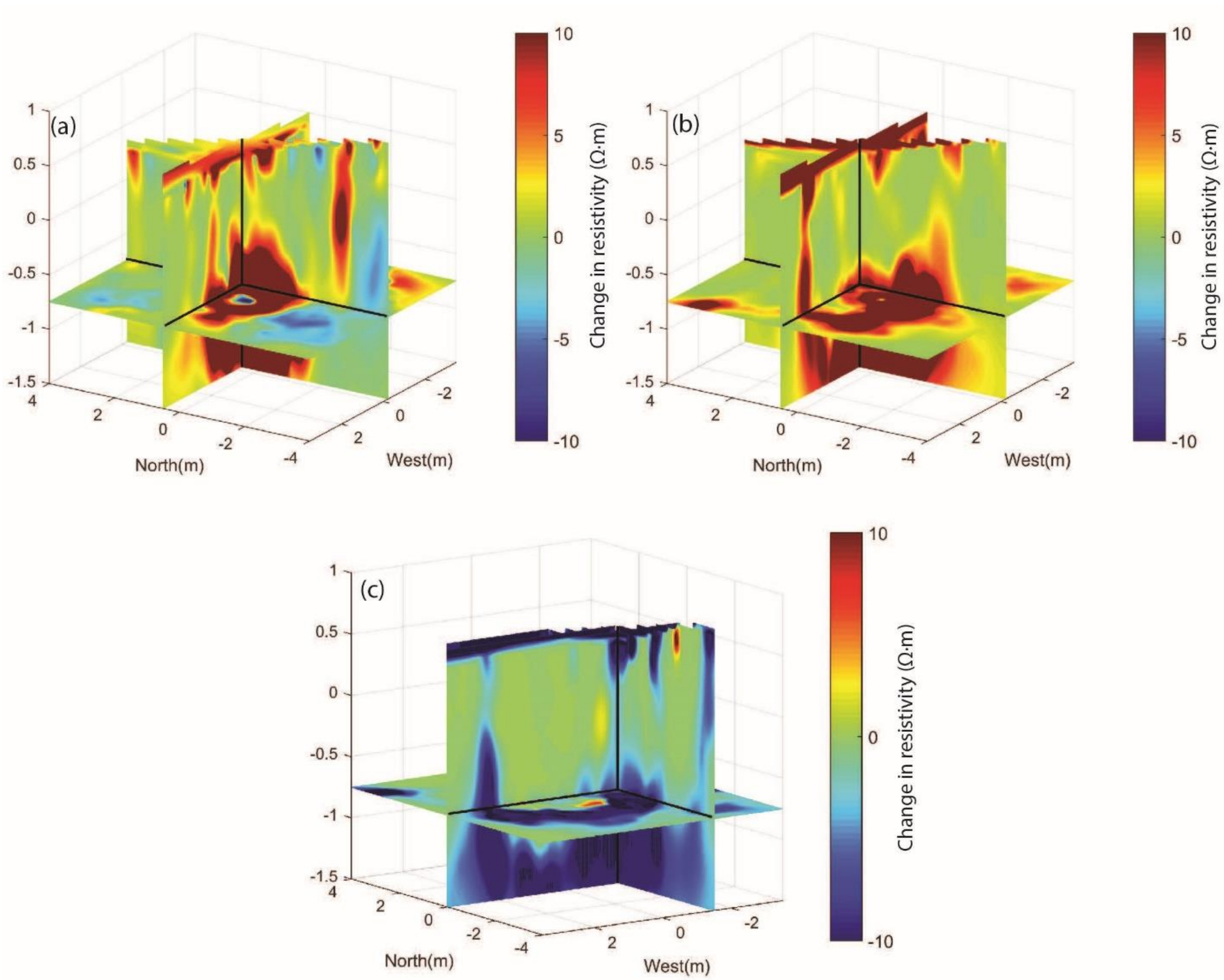

Figure A4: The change in resistivity for the springs of 2015 (a,) and 2016 (b). The change for the spring of 2015 is the difference in the grids from May 29th, 2015 to June 12th, 2015 and the change for the spring of 2016 is the difference between the grids gathered on February, 23rd, 2016 and June 29th, 2016. The change in the resistivity (a, b) for the fall 2015 (c). The grids are the difference in the resistivity grids taken on October 15th, 2015 and February 23rd, 2016.

Discussion

On October 18th, 2015 there was a rainstorm the precipitated 8mm at the MES sites. The resistivities response to this rainfall event is shown in figures A5. Between October 15th and October 29th, 2017 the TDR probes at MES show that the volumetric water content increased by about 15% at 5cm and 30% at 30cm, with little change in water content at 60cm and 90cm. This is similar to what was observed at the LES site, i.g. minimal infiltration bellow ~0.6m, and is again characteristic of the low flux summer dry period. The preferential flow paths structures change in resistivity in response to the precipitation event, suggesting a change in water content within the structures. Like what is observed at the LES site, this indicates that the preferential flow paths are acting as a conduit for flow that is bypassing the TDR probes.

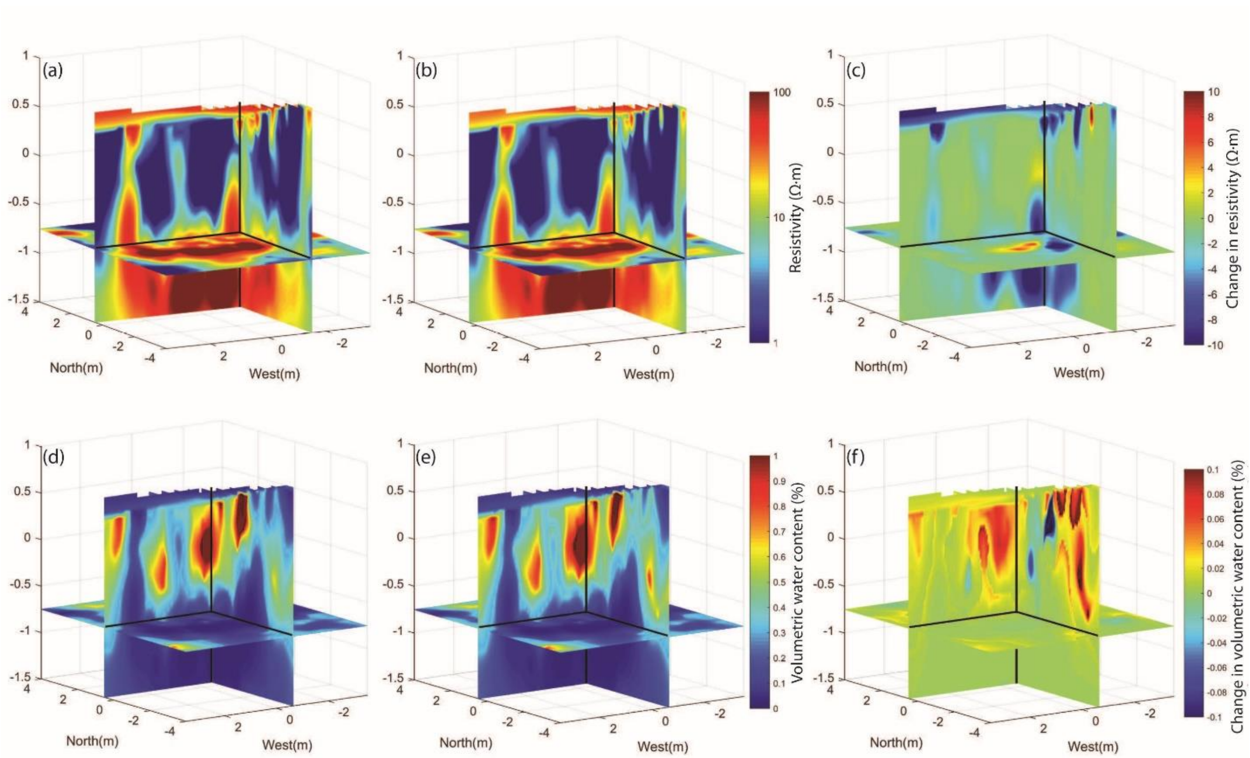

Figure A5: The response to the October 18th, 2015 rainfall event which precipitated 8 mm rain at the MES site. The resistivities and volumetric water contents were measured before the rainfall on October 15th (a, d) and after the rainfall on October 29th (b, e). The change in resistivity and volumetric water contents between the two surveys is shown in paned (c, f).

The seasonal changes in resistivity captured by the ERT at MES are similar to what was observed by the ERT at LES, however the TDR profiles show distinct differences. At LES the volumetric water content below 30cm never changes (figure 14), however at MES the volumetric water content at 90cm, the bottom of the profile, changes in response to the seasons and to precipitation during the wet high flux winter (figure

A1). The spring transitions captured by the ERT show (figures A4) drastic increases in resistivity in the bioturbated soil and preferential flow paths, with minor increases in resistivity in the weathered soil layer. There are some areas of decreases in resistivity over the spring of 2015 (figure A4), however this is likely due to the soils settling around the electrodes after their installation. As mentioned previously this site has extensive animal burrows. So it not unreasonable to assume that the soil characteristics changed in the uppers tens of centimeters over the first couple of weeks after the electrode installation. The decreases in resistivity at MES over the 2015 fall wetting period are essentially the reverse of what was overserved at the site during the spring of 2016. Where the resistivity increased drastically during the spring, i.g. the bioturbated soil and preferential flow paths, the resistivity decreased over the fall of 2015. Likewise there was a minor decrease in resistivity in the weathered soil layer through the fall of 2015.

The TDR profiles at MES show soil moisture changes at all depths measured suggesting a hydrologically connected soil profile. If the soil moisture wetted in a uniform manner as suggested by the TDR profile (figure A1) then it is expected that the change in resistivity over an area would be relatively uniform. This is however at odds with what is observed in the resistivity grids, where the resistivity change below ~15cm is more drastic in the preferential flow paths than within the weathered soils. The ERT alone would suggest that the majority of water is flowing through the preferential flow paths and a smaller amount through the weathered soils. At LES I assumed that the TDR probes are placed within the weathered soil layer, as neither the volumetric water content measured by the TDR profile nor the reasistivity of the weathered soil changed seasonally. However at MES the small change in resistivity within the weathered soil does not reflect the drastic changes in volumetric water content measured by the TDR profile. It is possible that the TDR probes at this site were placed within a preferential flow and not the weathered soil, thus the soil moisture profile shown figure TDR-ERT is of a preferential flow. However there are two TDR profiles at the MES sites (see figure 13) and while only profile 127n (figure A1) is shown the profile 127g has a similar pattern, and it is unlikely that both TDR profiles were placed within preferential flow paths. It is also possible that the weathered soils at MES's response to changes in water content are dampened because of the pedo-physics of the soil. However without excavation and testing this cannot be confirmed. Further the relatively high mean residuals, ~5Ωm, makes confident interpretation of the inversion results difficult, as the temporal changes in resistivity are being over smoothed.

Conclusion

The 2D ERT and SRT revealed a complex CZ structure that may be interbedded basalt flows that are weathering at different rates. The ERT results at the MES site stand in contrast with the results from the TDR profiles. While there are plausible explanations to why this might be, i.e. unique soil characteristics or TDR probes being positioned in preferential flow paths, because of the low level of convergence for the time-lapse survey a confident interpretation isn't possible.